UC Merced

UC Merced Electronic Theses and Dissertations

Title

UNDERSTANDING THE ROLE OF TRANSITION METALS AND METAL OXIDES ON CARBON STRUCTURES FOR ENHANCING ELECTROCATALYTIC ACTIVITY

Permalink

https://escholarship.org/uc/item/6qt5b3nz

Author

Macedo Andrade, Angela Macedo

Publication Date

2021

Peer reviewed|Thesis/dissertation

eScholarship.org Powered by the California Digital Library
University of California

UNDERSTANDING THE ROLE OF TRANSITION METALS AND METAL OXIDES ON CARBON STRUCTURES FOR ENHANCING ELECTROCATALYTIC ACTIVITY

by

Angela Macedo Andrade

A thesis submitted in partial satisfaction of
requirements for the degree of Doctor of Philosophy
August 2021

in

Materials and Biomaterials Science and Engineering

Committee in charge:
Professor Sarah Kurtz
Professor James Palko
Professor Po-Ya (Abel) Chuang
Professor Min Hwan Lee

Chapter 4 ©2021 The Royal Society of Chemistry (RCS)

All other chapters

©2021 Angela Macedo Andrade

All rights are reserved

The thesis of Angela Macedo Andrade is approved:

_____

Sarah Kurtz, Chair Date

_____

James Palko Date

_____

Po-Ya Abel Chuang Date

_____

Min Hwan Lee, Advisor Date

ACKNOWLEDGEMENTS

I would like to acknowledge my advisor, Min Hwan Lee, for his patience, guidance, and support as his student. I would also like to thank all my mentors who dedicated their time and helped me through this process: Lilian Davila, Jennifer Lu, Christopher Viney, Abel Chuang, Rudy Ortiz, Jessica Wang, and James Palko.

I especially want to express my gratitude to my colleges: Simranjit, Ziqi, Haoyu, Hung-Sen, Orbel and Alireza for their assistance in conducting experiments and for their friendship

I also want to acknowledge and recognize all my friends and family who were always there for me, supporting and encouraging me every step through.

TABLE OF CONTENTS

LIST OF FIGURES

LIST OF SYMBOLS AND ABBREVIATIONS

PEMFC	Polymer Electrolyte Membrane Fuel Cell
RFC	Regenerative Fuel Cell
GO	Graphene Oxide
TM	Transition Metal
ORR	Oxygen Reduction Reaction
OER	Oxygen Evolution Reaction
HER	Hydrogen Evolution Reaction
ALD	Atomic Layer Deposition
CV	Cyclic Voltammetry
LSV	Linear Sweep Voltammetry
RHE	Reversible Hydrogen Electrode
SEM	Scanning Electron Microscope
TEM	Transmission Electron Microscope
FTIR	Fourier Transform Infrared
TiO_2	Titanium Dioxide
G	Gibbs Free Energy
E	Potential Energy
j	Current Density
j_o	Exchange Current Density
F	Faraday Constant
η	Activation Loss
ω	Angular Frequency of Rotation

CURRICULUM VITAE

EDUCATION

University of California, Merced
School of Engineering
5200 North Lake Road
Merced, CA 95343

August 2021	Ph.D. Materials and Biomaterials Science and Engineering
December 2018	M.S. Mechanical Engineering
May 2015	B.S. Bioengineering *Minor: Chemistry*

PUBLICATIONS

Macedo Andrade, A., Liu, Z., Grewal, S., Nelson A.J., Lee, MH., *MOF-derived Co/Cu-embedded N-doped carbon for trifunctional ORR/OER/HER catalysis in alkaline media,* Dalton Transactions, 50, 5473, 2021

Grewal, S., **Macedo Andrade, A.**, Liu, Z., Garrido, J.A., Nelson, A.J., Kulkarni, A., Bajdich, M., Lee, MH., *Highly Active Bifunctional Oxygen Electrocatalytic Sites Realized in Ceria-Functionalized Graphene,* Advanced Sustainable Systems, 4, 2020

Grewal, S., **Macedo Andrade, A.**, Nelson, AJ, Thai, K., Lee, MH., *Critical Impact of Graphene Functionalization for Transition Metal Oxide/Graphene Hybrids on Oxygen, Reduction Reaction,* The Journal of Physical Chemistry C, 18, 206, 2018

Karimghaloo, A., **Macedo Andrade, A.**, Simranjit Grewal, Joon Hyung Shim and Min Hwan Lee. *Mechanism of cathodic performance enhancement of few nm oxide overcoat on porous Pt* cathode *of solid oxide fuel cell,* ACS Omega, 2, 806, 2017

Y. Jee, A. Karimaghaloo, **Macedo Andrade, A.**, H. Moon, Y. Li, J.-W. Han, H. Ishihara, P.-C. Su, V. C. Tung, and M. H. Lee*, *Graphene-based Oxygen Reduction Electrodes for Low Temperature Solid Oxide Fuel Cells*, *Fuel Cells* (*Cover Article*), 3, 344, 2017

CONFERENCE PRESENTATIONS

A Macedo Andrade, S Grewal, Z Liu and MH Lee, *Bimetallic Cobalt-Copper MOF Material for Bifunctional Oxygen Electrocatalysis.* Electrochemical Society Conference, Glasgow, Scotland, UK, July 21-26, 2019

A Macedo Andrade, Z Liu, S Grewal, SJ Bai and MH Lee, *UiO-66 As an Effective Support for Metal Oxides for Oxygen Evolution Catalysis.* Electrochemical Society Conference, Cancun, Quintana Roo, MX, September 30-October 4, 2018

A Macedo, S Grewal, A Karimaghaloo and MH Lee. *Functionalization of Graphene Oxide by Atomic Layer Deposition using Titanium Oxide for Improving Electrocatalysis*. American Physical Society Far West Conference, Merced, Ca. November 3-4, 2017.

A Macedo Andrade, A Karimaghaloo, S Grewal and MH Lee. Non-Stoichiometric Titanium Dioxide Incorporation onto Reduced Graphene Oxide by Atomic Layer Deposition for Oxygen Reduction Catalysis. *Electrochemical Society Conference*, San Diego, CA, June 2016.

Macedo A. Angela, and Xinping He. *Electrocatalysis of Oxygen Reduction Reactions using N- containing Carbon Cloth with Fe metal*. BioNanotechnology Summer Institute, Urbana- Champaign, Il July-August 27-8, 2015.

FELLOWHIPS

NASA MACES (Merced Nanomaterials Center for Energy and Sensing) Fellowship. University of California, Merced, Merced, CA January 2016 – May 2017.

United States Department of Agriculture Hispanic Serving Institutions National Program (USDA HSI) Scholar. University of California, Merced, CA May 15-December 2015

ABSTRACT

The studies presented in this thesis focus on developing non-precious metal electrodes for oxygen reduction reactions (ORR), oxygen evolution reactions (OER), and hydrogen evolution reaction (HER), the core catalysis of fuel cells and electrolyzers. Metal oxides on carbon support are mainly considered as the catalytically active materials in this study. Two approaches of fabrication are presented: one based upon atomic layer deposition (ALD) and one by a wet synthesis process known as the solvothermal method. The resulting catalysts are characterized to reveal the process-performance relationship for ORR, OER, and HER.

In the first study (Chapter 4), we demonstrate a bimetallic Co/Cu-embedded N-doped carbon structure for trifunctional catalysis of ORR, OER, and HER in alkaline media. A hybrid catalyst synthesized through a metal-organic framework-based process (M-NC-CoCu) enables active trifunctional catalysis due to its multi-faceted favorable characteristics. It is believed that a range of catalytically active sites are formed through the approach including well-dispersed tiny $CuCo_2O_4$ phases, a high concentration of pyridinic and graphitic N, and Cu-O_x, Cu-N_x, and Co-N_x moieties. In addition, a high-surface-area morphology with a high concentration of sp^2 bonding, which is beneficial for facilitated electron conduction, further contributes to the performance as an electrocatalyst.

The second study (Chapter 5) investigates the catalytic activities of titanium dioxide (TiO_2) incorporated onto graphene oxygen (GO) by atomic layer deposition (ALD). The catalytic activity was systematically measured by cyclic voltammetry (CV). Evidence shows that TiO_2 bonded on the surface of GO is catalytic active. An ALD treatment of TiO_2 shows improvement in the catalytic activity compared to non-treated graphene. The ALD temperature also affects the catalytic performance. A higher temperature results in a higher catalytic activity, which is ascribed to the simultaneous reduction of GO and the addition of catalytically active TiO_2/GO interfaces by ALD. In addition, there is also an optimal number of ALD cycles for enhanced catalytic activity.

In the third study (Chapter 6), a zinc-based zeolitic imidazole framework (ZIF-8) is carbonized to form organized N-doped carbon nanostructures. The carbonized ZIF-8 (C-ZIF-8) was then used as a substrate (support) for ALD. Titanium (Ti) and/or cerium (Ce) precursors were introduced to the ALD chamber to form bimetallic (Ti and Ce) or monometallic (Ti or Ce) hybrids with C-ZIF-8. The effects of bimetal incorporation on the electrocatalytic properties of the resulting hybrid systems toward OER and HER is investigated. The optimization of ALD parameters, such as the number of cycles, temperature, and pressure for catalytic performance are also discussed.

1. INTRODUCTION

According to the U.S. Energy Information Administration (EIA), currently, fossil fuels such as petroleum, natural gas, and coal account for more than 80% of the energy used in the United States. Unfortunately, continuing a heavy usage of fossil fuel-based electricity for an ever-increasing global population is expected to exacerbate already-existing problems such as pollution, global warming, and pollution-related disease.

In addition, the U.S. EIA showed that transportation is one of the biggest sectors for energy consumption. Transportation composes 37% of the energy consumed by the U.S. in 2019. For this reason, one of the major focuses is finding an alternative clean energy source that can replace fossil fuel based internal combustion engines in the transportation sector. Presently, this creates a need for growth and expansion of electrified vehicles starting from automobiles and ranging to semi-trucks, marine vessels, aircrafts and space crafts.

Hydrogen-based fuel cells and batteries are energy conversion devices that can produce electricity without forming harmful byproducts. In addition, if the reactants for these devices, such as hydrogen and oxygen, are produced from renewable energy sources such as solar, wind or biomass, the process itself has the potential of producing virtually zero waste. Furthermore, fuel cells and batteries have a higher efficiency than commonly used internal combustion engines. According to the Department of Energy, while combustion engines have an efficiency of about 35%, hydrogen based fuel cells can reach an efficiency of up to 60% or even higher. The process in a combustion engine requires the conversion of chemical energy into heat energy that is then used for mechanical energy to create electrical energy. On the other hand, both fuel cells and batteries have the advantage of producing electrical energy directly from chemical energy virtually emission free.

However, in batteries, their reactants cannot be replenished continuously, and often the energy density of a battery is compromised by its scalability. Scaling batteries to large sizes is an issue because it is used both for energy storage and as an energy

conversion device. The more energy storage you need the bigger the size of the battery should be. The electrification by battery of big vehicles such as semi trucks, aircrafts and even spacecrafts becomes an issue. On the other hand, the scaling of a fuel cell is readily achievable because the reactant (or fuel) reservoir is separate from the actual energy conversion component.

For this reason, fuel cells have an advantage in achieving higher energy density (the amount of energy per given size or weight) than batteries for larger applications. Batteries, on the other hand, have a higher power density (the rate of energy generation per given size or weight) than fuel cells due to faster redox reactions. The eventual goal of alternative energy conversion and storage devices is to compete against the conventional internal combustion engine (ICE), which has both high energy and power density.[1]

In addition to providing electrical energy, devices such as regenerative fuel cells (RFCs) and rechargeable metal-air batteries (RMABs), can be self-sustainable energy devices through reactant regenerations. To continuously replenish their reactants, RFCs and RMABs can perform both electrification and recharging processes. This set-up provides a system that is pollution free and can serve as a solution for not only the production of hydrogen in hydrogen-based RFCs, but of oxygen as well for both devices.

In general, the major steps of energy conversion in these types of devices are (1) reactant transport, (2) electrochemical reaction, (3) ionic and electronic conduction, and (4) product removal. Though, for many energy conversion devices one of the biggest constraints for their commercialization lies in the drawbacks of the kinetics of their respective electrochemical reactions.

Like in any other electrochemical energy devices, there are three limitations in the main processes causing voltage losses that prevent them from extracting all the thermodynamically determined voltage in an efficient way: redox reaction, ohmic transport and mass transport. The overpotential to incur a desired redox reaction is called activation loss. The activation loss, especially from ORR, OER, and HER are often the most detrimental in these devices due to the sluggish kinetics of these reactions. Thus,

vast research and development for energy conversion devices have focused on the catalytic activity of electrode material where ORR, OER, and HER occur.

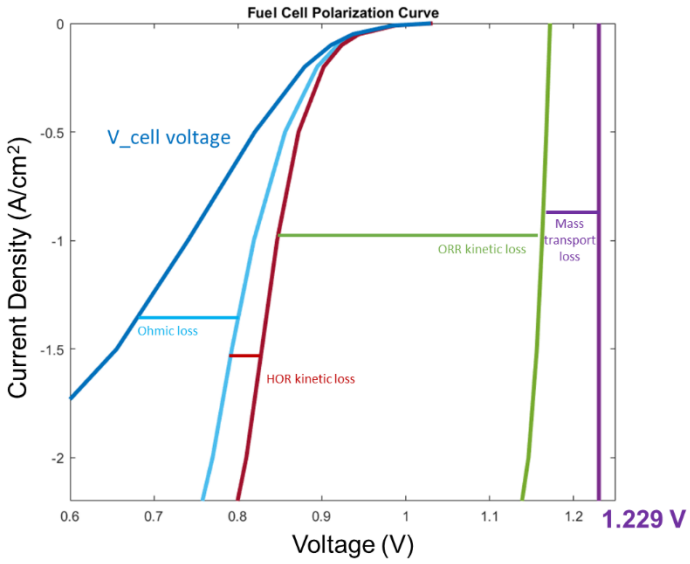

Figure 1-1. polarization curve showing the different losses in a fuel cell

Noble metals like platinum, iridium and ruthenium have been widely used as an electrocatalytic material to mitigate the activation barrier against ORR, OER and HER. However, due to their prohibitive cost, scarcity and susceptibility to poisoning, there has been persistent research to find alternative materials. Most of the alternatives being developed are composed of non-precious metals,[2] heterogeneous material[3] or are completely metal free[4] that are mainly composed of carbon. Many of the newly developed alternative catalysts have been found not only more cost effective and abundant but also more efficient and durable than noble metals-based electrocatalyst.[5,6] Especially, for the development of high-performance RFCs or metal-air batteries, an efficient catalyst not only for oxygen reduction but also for oxygen and hydrogen evolution is necessary.

Currently, there is a wide range of bifunctional catalysts made of well-known noble metals such as Pt, Ir and Ru[7,8], transition metal compounds (TMCs) such as MnO_2[9] and Co_3O_4[10], metal sulfides like MoS_2[11], and metal-free bifunctional catalysts synthesized

from doped carbon-based polymer nanostructure[12]. Commonly used bifunctional electrocatalysts have been noble metal mixtures which include platinum, ruthenium and/or iridium.[13] These noble metal based materials are not desirable for use due to their high cost, limited availability and susceptibility to performance degradation. Bifunctional and even trifunctional electrocatalysts made from transition metals, are not only less expensive than noble metals but also made from a more abundant resource, but have exhibited comparable performance to noble metals in ORR, OER and HER.[12,14,15]

Regardless of whether the electrocatalytic reaction is ORR, OER or HER, these electrochemical reactions can be broken down into a series of simple steps that include:

a. Mass transport: reactant moving to near the electrode
b. Adsorption: reactant adsorbed on the electrode surface
c. Chemisorption: breaking of reactant bonds
d. Electron transfer: electrochemical charge transfer
e. Desorption: product being released from electrode

For various electrocatalytic materials including noble metals, it is often not clear which of these processes is the rate-limiting step responsible for high activation loss in a given condition. However, these processes do outline the attributes of good electrocatalysts such as high surface area, electronic conductivity, and catalytic activity. Chemical and mechanical stability is additionally required.

The overall performance of an electrocatalyst is highly dependent on the morphological, structural, and electronic configurations and composition of the catalyst material, which are affected by the condition of their synthesis process in terms of temperature, pressure, reaction time and reaction environment in addition to starting materials/precursors. Turning materials into nanostructures can also allow for higher performance per mass. Hybridization of dissimilar materials is another frequently employed approach; for example, incorporating transition metals into carbon structures

enhances the electrocatalytic activity further while providing them a support for potential nanoparticle that would otherwise aggregate.[16]

TMCs have the potential of forming different stoichiometry, which enables them to tune the absorption kinetics of oxygen and hydrogen and thus promote ORR, OER, and HER. For some TMCs such as TiO_2 and Co_3O_4, a certain stoichiometry has shown to have better electrocatalytic performance for ORR[17,18], and others are good for water electrolysis.[2,13] The stoichiometry of TMCs can be altered by changing the environmental condition in terms of gas type, temperature, and pressure. Another attribute of materials that affects their electrocatalytic performance is the crystal structure formed. Different crystal structures have distinct symmetries, atom arrangements, and bond structures. [19,20]These can affect properties such as conductivity, chemical stability, and mechanical stability, which can affect the efficiency of these electrochemical reactions. For instance, titanium oxide (TiO_x) is a polymorphous structure that has different types of tetragonal crystal structures.[18,21] Studies have shown that anatase structure has better catalytic activity than rutile structure, and even amorphous structure.[18]

As aforementioned, multifunctional catalysts are the key components of RFCs and metal-air batteries. TMCs supported on carbon structures have long been of high interest due to their low cost, abundance, facile synthesis, and have demonstrated to render multi-catalytic activity for oxygen reduction[22], oxygen evolution[10], and even hydrogen evolution [23], which make them ideal candidates for their use in RFCs and metal-air batteries.

1.1 Research Study

This thesis will present two approaches for synthesizing transition metals supported on carbon structures, using atomic layer deposition (ALD) and the solvothermal method, for their use as electrocatalysts. In this study I will be presenting two methods that aim in synthesizing transition bimetal electrocatalyst that have comparable or exceed the catalytic performance of noble metals:

1) Solvothermal thermal synthesis followed by pyrolysis of a metal-organic framework (MOF) that create a transition bimetal electrocatalyst.
2) Atomically dispersing transition metal and metal oxides on the surface of ordered carbon structures by ALD.

The objectives of these studies are:

1. To develop efficient electrocatalyst for ORR, OER, and HER where transition metals/metal oxides are atomically dispersed on carbon supports;
2. To identify the material characteristics responsible for improved electrocatalytic performance towards ORR, OER, and HER;
3. To enhance the understanding of process-property-performance relationship of hybrid electrocatalyst toward ORR, OER, and HER.

2. BACKGROUND

2.2 Renewable Energy Devices

According to the U.S. Energy Information Administration (EIA), currently, fossil fuels such as petroleum, natural gas, and coal account for more than 80% of the energy used in the United States. Unfortunately, continuing a heavy usage of fossil fuel-based electricity for an ever-increasing global population is expected to exacerbate already-existing problems such

2.3 Overview of Energy Storage and Energy Conversion

As previously discussed, the focus of this research is to improve the overall performance of energy conversion devices by improving the overall kinetics of their respective electrochemical reactions. Even though energy conversion devices have different reactant combinations and electrolytes, I will focus on hydrogen/oxygen systems using proton exchange membrane (PEM) and alkaline electrolytes. Therefore, the reactions discussed here include the electrolysis reactions OER and HER, and as aforementioned ORR is six times slower than HOR, so we will also discuss this reaction.

2.4 Overview of Energy Conversion Devices

2.4.1 Fuel Cells: PEMFCs and AFCs

Some of the common types of fuel cells include polymer electrolyte membrane fuel cell (PEMFC), phosphoric acid fuel cell (PAFC), alkaline fuel cell (AFC), molten carbonate fuel cell (MCFC) and solid oxide fuel cell (SOFC). Each type of fuel cell differs in the types of reactants used and the conditions at which they operate. For the studies presented in this thesis we will focus mostly on hydrogen based PEMFCs and AFCs. Both types of fuel cells have three main components: two electrodes and an electrolyte (Figure 2-1(a) and (b)).

Hydrogen-based PEMFCs have a polymer-based electrolyte that can provide high efficiency at low operating temperatures, around 80°C, with zero emissions and virtually silent operation. The polymer electrolyte membrane is usually made of hydrocarbons that contain fluorine groups and sulfonic groups to aid with the transfer of the ions and water while being highly resistant against electrons. The most commonly used polymer electrolyte membranes are Nafion (sulfonated tetrafluoroethylene-based fluoropolymer-copolymer by DuPont) and persulfonated polytetrafluoroethylene (PTFE). Similarly, alkaline fuel cells (AFCs) operate at lower temperatures ranging from 60 - 220°C. However, they differ from PEMFCs because they use an aqueous alkaline electrolyte instead of acidic polymer electrolyte member. The commonly used electrolyte for AFCs is derived from potassium hydroxide (KOH). Also, as will be discussed below, the by-products of the reactions for AFCs differ from those of PEMFCs.

For both types of hydrogen-based fuel cells there are two electrochemical reactions occurring: hydrogen oxidation reaction (HOR) and oxygen reduction reactions (ORR). The oxidation of hydrogen occurs in the anode side while the reduction of oxygen happens at the cathode side. These reactions produce electrical energy, heat and by-products such as water and hydroxide. While the electrons produced from the oxidation of hydrogen at the anode side flow through an external circuit, which is used to power a device, the ions produced from this reaction flow through the electrolyte. The hydrogen ions along with the electrons head towards the cathode side to reduce oxygen into water. The electrochemical reactions occur in a location that is known as the triple phase boundary (TPB), where electrode material, electrolyte and incoming reactant meet altogether. Because the kinetics of ORR is orders of magnitude slower than HOR, much of the focus for electrode design is focused on cathode side.[24]

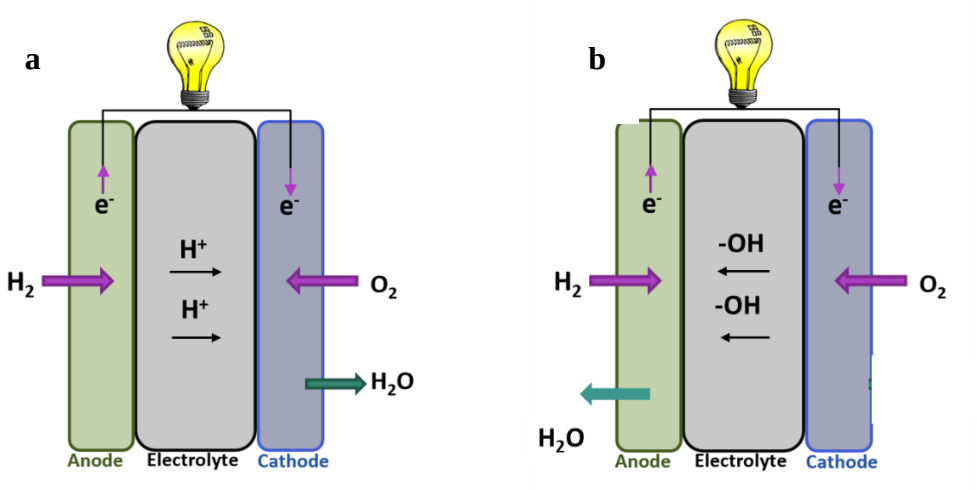

Figure 2-1. simplified diagram of a (a) PEMFC and (b) AFC showing the basic three components: anode, cathode and electrolyte, and reactants and products

2.4.2 Electrolyzers

An electrolyzer functions opposite to a fuel cell; instead of generating energy, it requires energy to convert products back to reactants for energy storage purposes. So instead of dealing with HOR and ORR, hydrogen-based electrolyzers' electrochemical reactions are essentially hydrogen evolution reactions (HER) and oxygen evolution reactions (OER). However similar to fuel cells, electrolyzers have the basic components, which include two electrodes and an electrolyte, and can also have a PEM or alkaline-based electrolyte. Depending on the type of electrolyte used, they will produce different products that again will be discussed later on throughout this chapter. To make the processing in electrolyzers more environmentally friendly, their electric energy source is usually some sort of renewable energy sources such a solar cells.

2.4.3 Regenerative Fuel Cells

Regenerative fuel cells (RFCs) have all the basic components of fuel cells, and additionally also operate as an electrolyzer (Figure 2-2) for energy storage.

There are two main types of regenerative fuel cells. One type is known as a discrete regenerative fuel cells (DRFC) where the electrolyzer and fuel cell components are in two separate stacks. Unitized regenerative fuel cells (URFC), on the other hand, carry out the electrolyzer and fuel cell functions in the same stack. For this reason, URFCs do not need an auxiliary heating because everything should happen in the same stack. It depends on the application to determine which type of regenerative fuel cell is a better option. URFCs can be a better choice when oxygen is stored and used, and DRFCs are a better choice when air is used for operating in fuel cell mode.[25]

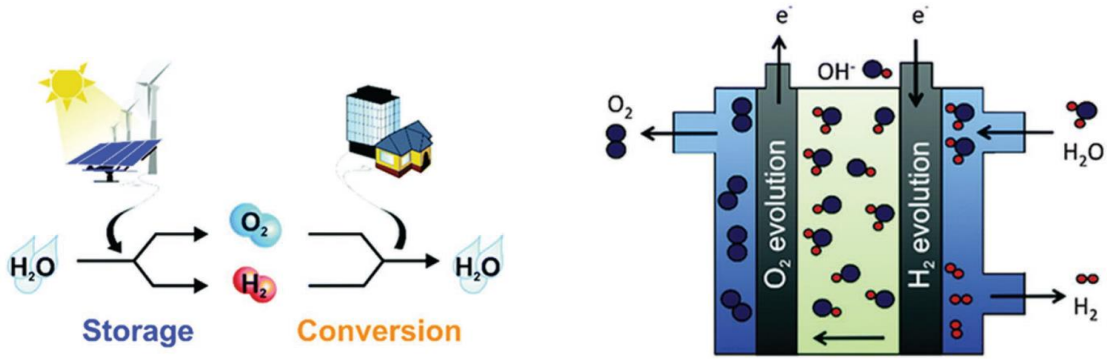

Figure 2-2. a) hydrogen and oxygen cycles for energy storage and conversion. b) scheme of anion-exchange membrane electrolyzer (Adapted from D.Yan et al. [[26]])

The electrode design is also dependent on the type of regenerative fuel cell. For instance, the design of an electrolyzer cathode in a URFC, or where the evolution of oxygen occurs, is designed to allow for flooding. Flooding is when water covers the surface of the electrode material, which for an electrolyzer is needed to split water into oxygen. Whereas the fuel cell cathode, where oxidation reduction occurs, must repel water in order to prevent any blockage of active sites responsible for the electrocatalysis. Operation with pure oxygen in flooded or partially flooded electrodes may be feasible,

particularly at elevated pressure.[27] Though for DRFCs, operation with air, has shown to have limitations in mass transport.

Generally, electrode material in energy conversion devices such as URFC systems not only have to catalyze ORR and HOR but should be able to split water to generate hydrogen and oxygen. This means that the electrodes used in an URFC should either be a bifunctional or even trifunctional electrocatalysts. The goal for a bifunctional or trifunctional electrode material is for it to catalyze water splitting with minimal energy input, but it should still have the characteristics of a PEMFC electrode to catalyze HOR and ORR as well in an efficient way.

2.5 Thermodynamics of Electrochemical Reactions

A chemical reaction can render a certain amount of energy available to do work. For most energy conversion devices discussed here that work is usually known as electrical work (W_{elec}). The Gibbs free energy can show how much work potential is available in a chemical reaction. The Gibbs free energy is derived from the Euler equation using a Legendre transformation. After differentiating that equation, we get the following Gibbs free energy equation.

$$dG = dU - TdS - SdT + pdV + vdp \quad \text{Equation 2.1}$$

When inserting the expression for dU (Equation 2.12) in the equation (Equation 2.11), where the term for work is expanded to include both mechanical and electric work, we get the following (Equation 2.13)

$$dU = TdS - dW = TdS - (pdV + dW_{elec}) \quad \text{Equation 2.2}$$

$$dG = -SdT + Vdp - dW_{elec} \quad \text{Equation 2.3}$$

If the process is at constant temperature and pressure, then differential (Equation 2.13) reduces to:

$$dG = -dW_{elec} \quad \text{Equation 2.4}$$

Essentially, the maximum amount of electrical work available, at a constant temperature and pressure, is represented by the negative of the Gibbs free energy difference.

$$W_{elec} = -\Delta G_{rxn}$$ Equation 2.5

Now W_{elec} can be represented as the work done by a moving charge Q (coulombs) through an electrical potential difference E (volts)

$$W_{elec} = EQ$$ Equation 2.6

In this situation, Q can be considered as an electron carrier resulting in:

$$Q = nF$$ Equation 2.7

In $Q = nF$ Equation 2.7, *n* is the number of moles of electrons transferred and F is Faraday's constant. Putting all these equations together results in:

$$\Delta G_{rxn} = -nFE$$ Equation 2.8

Furthermore, the change in free energy for a reaction (ΔG_{rxn}) can also be expressed in terms of the equilibrium concentrations of the reactants and products. For the given reaction below (Equation 2.19) the change in free energy (Equation 2.20) is the following:

$$A + B \leftrightarrow C + D$$ Equation 2.9

$$\Delta G_{rxn} = \Delta G^{o}_{rxn} - RTln(\frac{a_c + a_d}{a_a + a_b})$$ Equation 2.10

G^0 refers to the Gibbs free energy at the standard condition, R is the gas constant, T is temperature and a is the activity of corresponding species involved in the electrochemical reaction.

The Nernst equation can then be formulated by combing equations 2.18 and 2.20. For electrochemical reactions that occur at a non-standard condition, the Nernst Equation can

be used to quantify the reversible voltage. In fact, PEMFCs and AFCs are usually operated at a non-standard condition (~ 80°C). The equation describes how the reversible voltage potential (E) varies with temperature and reactant/product activities.

$$E = E^0 - \frac{RT}{nF} ln(\frac{a_c + a_d}{a_a + a_b}) \quad \text{Equation 2.11}$$

This depends on the chemical nature it takes on, and it could be for an ideal gas, nonideal gas, dilute ideal solution, nonideal solutions, pure components, or metals. The reversible cell potential indicates the maximum electrical potential that could be extracted from an electrochemical reaction at a given temperature and reactant activity.

2.6 Kinetics of Electrochemical Reactions

The kinetics of electrochemical reactions determine how fast and efficient these reactions proceed. The rate of a reaction is partly determined by the energy barrier height (ΔG^*) for a reactant to overcome before turning into a product. The rate of conversion of reactants to products largely depends on the probability of that reactant species being at an activated state, which is the state that is capable of transitioning to either products or reactants.

The probability of finding a species in the activated state is denoted as P_{act} in the following equation. As shown below, P_{act} is exponentially dependent on the activation energy (ΔG^*), which is the size of the activation barrier. The probability of finding an active state species can be used as a direct way to measure the rate of these reactions.

$$P_{act} = e^{-\Delta G^*/RT} \quad \text{Equation 2.12}$$

During an electrochemical reaction, electrons are either being generated or consumed, which is captured as current (i), the rate of electrical charge flow. The current generated is proportional to the area of catalytically active surface where these reactions occur. With a larger active surface area, the overall rate of the reaction should increase. Current normalized by the active surface area (A) is known as current density (j). With this

parameter, the reactivity of different catalyst in a given catalysis can be in part compared per unit area.

$$j = \frac{i}{A} \text{ Equation 2.13}$$

The current density is often used to describe the overall net reaction rate, which can be denoted as the rate of forward reaction (j_1) minus the rate of the reverse reaction (j_2). Here, the forward reaction is defined as the reaction that transforms reactant to product. When these two reactions reach an equilibrium, that is when $j_1 = j_2 = j_0$, the net reaction rate is zero. This indicates that both the forward and reverse reactions are taking place at the same rate, where j_0 is known as the exchange current density.

As soon as electrons are allowed to flow in an electrochemical cell, the forward reaction should proceed faster than the reverse reaction rate in a spontaneous reaction. However, the unequal rates quickly result in a buildup of charge over time, which results in a potential difference (known as the Galvani potential) that counterbalances the free energy difference between the reactant and product states. This eventually establishes an electrochemical equilibrium with a net reaction current equal to zero.

To produce a net current from a fuel cell, the potential difference between the two electrodes should be forced to deviate from the equilibrium potential (i.e., the open circuit potential). This is achieved by sacrificing part of the thermodynamically determined cell voltage. The voltage being sacrificed is also known as the overpotential or voltage loss. The Butler-Volmer (B-V) equation describes how much of the cell voltage needs to be sacrificed for a given reaction rate at a given temperature. In addition, the B-V equation shows the current density (j) extracted from a cell has an exponential relationship with the overpotential (η).

$$j = j_0(e^{\alpha nF\eta/(RT)} - e^{-(1-\alpha)nF\eta/(RT)}) \text{ Equation 2.14}$$

where α is the transfer coefficient, which depends on the symmetry of the activation barrier. The B-V equation could be simplified given certain conditions. A linear approximation can be used when the activation loss (η) is small. The linear

approximation comes from a Taylor series expansion. Ignoring exponential with powers higher than 1, it becomes:

$$j = j_0 \frac{nF\eta}{RT}$$ Equation 2.15

Another simplification done to the B-V equation is the Tafel approximation, which is used at large η (usually when $j > j_0$). In this case, the forward reaction dominates, and the reverse component disappears resulting in the following equation:

$$j = j_0 e^{\alpha nF\eta/(RT)}$$ Equation 2.16

Overall, improving the kinetics of the electrochemical reactions in a cell involves increasing j_0. Recall that j_0 is the exchange current density of the forward and reverse reaction at equilibrium, which is affected by various parameters including temperature, activation energy, reactant concentration and surface area. This set of equations help with identifying what characteristics of a material affect the kinetics and overall performance of a fuel cell, which aids in the design of an effective electrocatalyst.

2.7 ORR, OER and HER

The products formed by oxygen reactions depend on whether it occurs in an acidic environment or basic environment. In general, ORR is a multi-electron reaction that has different intermediates and products formations. As seen in the equations below, both acid and basic environment have a four electron ($4e^-$) and two electron ($2e^-$) process. In an alkaline medium which is specific to metal-air batteries and alkaline-based fuel cells, two different pathways of ORR (i.e. $4e^-$ or $2e^-$ process) can be described as:

$$O_2 + 2H_2O + 4e^- \rightarrow 4OH^-;\ E^0 = 0.401V \text{ vs SHE}$$ Equation 2.17

$$O_2 + H_2O + 2e^- \rightarrow HO_2^- + OH^-;\ E^0 = -0.076 \text{ vs SHE}$$ Equation 2.18

$$HO^-_2 + H_2O + 2e^- \rightarrow 3OH^-;\ E^0 = 0.878 \text{ V vs SHE}$$ Equation 2.19

The polymer electrolyte membrane is usually made from sulfonated tetrafluoroethylene polymer (widely known as Nafion, a product from Dupont), sulfonic groups are made for an acidic environment. For this reason, PEMFC operation in an acidic environment is preferred. For acid, the four-electron process produces water whereas in basic (or alkaline) environment the product is hydroxides.[28] The ORR in acid can be written as:

$$O_2 + 4H^+ + 4e^- \rightarrow 2H_2O;\ E^0 = 1.229\ V \text{ vs SHE} \quad \text{Equation 2.20}$$

$$O_2 + 2H^+ + 2e^- \rightarrow H_2O_2;\ E^0 = -0.695\ V \text{ vs SHE} \quad \text{Equation 2.21}$$

$$H_2O_2 + 2H^+ + 2e^- \rightarrow 2H_2O\ E^0 = 1.776\ V \text{ vs SHE} \quad \text{Equation 2.22}$$

Similar to ORR the electrolysis or splitting of water process is a multi-electron process, , and the products of these reactions also depend on the environment they take place in as seen below. However, OER and HER have different set of reactants, which result in different intermediates and products.[29] Typically, the 2 e^- pathway processes of ORR, lead to a lower conversion efficiency of chemical energy to electrical energy

In alkaline media:

$$\underline{\text{OER:}}\ 4OH^- \rightarrow O_2 + 2H_2O + 4e^-;\ E^0 = 0.401\ V \text{ vs SHE} \quad \text{Equation 2.23}$$

$$\underline{\text{HER:}}\ 4H_2O + 4e^- \rightarrow 2H_2 + 4OH^-;\ E^0 = -0.829\ V \text{ vs SHE} \quad \text{Equation 2.24}$$

In acidic media:

$$\underline{\text{OER:}}\ 2H_2O \rightarrow O_2 + 4H^+ + 4e^-;\ E^0 = 1.23\ V \text{ vs SHE} \quad \text{Equation 2.25}$$

$$\underline{\text{HER:}}\ 4H^+ + 4e^- \rightarrow 2H_2;\ E^0 = 0\ V \text{ vs SHE} \quad \text{Equation 2.26}$$

Most of these electrochemical reactions occurring in both fuel cells and electrolyzers can be broken down into a series of steps, which include mass transport, adsorption, dissociation, electron transport and mass transport. To develop high-performance energy conversion device, an efficient catalyst not only for oxygen reduction but also oxygen evolution and hydrogen evolution is necessary. Consequently, a key attribute for an

electrocatalyst for this type of application needs to be bifunctional or even trifunctional towards ORR, OER and HER. renewable energy devices would be bifunctionality in oxygen electrocatalysis for both ORR and OER.

2.8 Literature Review

2.8.1 Noble Metal Electrocatalysts

Noble metals have been widely used as electrocatalytic material to mitigate the activation barrier against ORR and OER. The efficiency of the precious metal electrode materials is due to their d-band vacancies and shorter metal to metal interatomic distances that allow for strong metal-reactant interactions during the separation state (also known as dissociative adsorption) of ORR, OER and HER.[28]The separation state is often described as the chemisorption of the reactants to the surface of the electrode material. Chemisorption is referred to the adsorption of reactants to the surface of the electrode that involves a chemical reaction. Considering ORR as an example, the interaction between Pt and oxygen during the separation state weakens the oxygen-oxygen bonding and therefore promotes the dissociation of oxygen molecules.[30] The same applies to other reactions such as HER.

Electrochemical reactions such as OER and HER produces molecular oxygen and hydrogen during the process in electrolysis mode, as opposed to fuel cell mode. Unlike the case for ORR, platinum is not a suitable material for catalyzing the respective reactions. Instead, ruthenium (Ru) and iridium (Ir) are well known OER and HER electrocatalyst. As is the case for Pt in ORR, Ru and Ir catalyze adsorption and dissociation of the reactants and intermediates in OER and HER.

An approach of mitigating this issue has been using less platinum by making nanostructures that will still render an efficient electrocatalysis. Some of these nanostructures including jagged Pt nanowires rendered record-breaking specific mass activity and electrochemical surface area.[31] Another way is creating alloys with other inexpensive metals, which still maintains a high electrocatalytic efficiency.[32] However, noble metals, especially Pt, show reduced efficiency for catalyzing ORR over long-term

cycling. In particular, in the presence of carbon dioxide (CO_2) and carbon monoxide (CO), Pt loses most of its catalytic activity towards oxygen.[12]

2.8.2 Transition Metal-Based Electrocatalysts

Even though the electrocatalytic mechanisms for transition metals are still ambiguous, there are some characteristics attributed to improving their overall electrocatalytic performance. Some of the key advantages of transition metals (TM) and their oxides (TMO) is that they can take up different oxidation states, which has shown to alter their catalytic performance.[33,18,34] In addition TM type catalyst are more suitable for replacing noble metals because of their cost-effectiveness and multi-valence, and tunability of chemical composition, structure, and morphology.[35,36] For some TMs such as TiO_2 and Co_3O_4, certain stoichiometry has shown to have better electrocatalytic performance for ORR[17,18], and others are good for water electrolysis.[2,13] The stoichiometry of TMs can be altered by changing the environmental condition in terms of gas type, temperature and pressure.

Another attribute of materials that affect their electrocatalytic performance is the crystal structure formed. Different crystal structures have distinct symmetries, atom arrangements, and bond structures that can affect properties such as conductivity, chemical stability, and mechanical stability, which in turn influences the efficiency of these electrochemical reactions. For instance, titanium oxide (TiO_x) is a polymorphous structure that has different types of tetragonal crystal structures[18,21]. Studies have shown that anatase structure has better catalytic activity than rutile structure, and even amorphous structure for ORR catalysis.[18]

However, the metal atom utilization in homogeneous TM catalysts can reach 100%, which is orders of magnitude higher than that of heterogeneous catalysts.[37] This is a mainly because transition metal heterogeneous catalysts might feature non-uniform aggregates of hundreds and/or thousands of metal atoms. Therefore, only a small fraction of transition metal atoms is exposed to reactants, which is not favorable for catalysis.

Increasing the metal atom utilization of a catalyst is particularly important for heterogeneous TM catalysts. [38]

2.8.3 Carbon-based Electrocatalysts

Graphene and its derivatives have been intensively investigated for their material properties that are advantageous for a wide range of applications. In many electrocatalytic materials, carbon structures such as graphene and carbon nanotubes have played the role of being supportive structures providing a physical surface for dispersing small metal particles or nanostructures[39,40] and enhancing the overall electronic conductivity.[41,42] However, in recent years, metal free electrocatalyst have also shown to have exceptional electrocatalytic abilities.[43,12]

Defects in a graphene-based material itself can improve electrocatalytic properties. Defects induced by heteroatomic doping can aid in the redistribution of electronic energy profile, which has been shown to change the chemisorption mode of reactants such O_2 in ORR by weakening the O-O bonding.[44,26] A doping often induces defects while the overall crystal structure is unchanged. Heteroatoms, such nitrogen, can alter the electronic properties of the nearby carbon atoms due to differences in atomic size, electronegativity and other factors.[45] Nitrogen, sulfur and phosphorus are all commonly used dopants in carbon-based materials, which can serve as a base structure material to enhance the electrocatalytic properties of transitional metal and transitional metal structures.[46,43,47]

In some cases, heteroatoms like nitrogen can be removed to form vacancies. Yao et al. prepared a 2D graphene material with carbon defects (DG) by a facile heat treatment process.[48] This process created many types of single-atom vacancies induced by N-atom removal. Data confirmed the absence of nitrogen in the material, which resulted in various defects on the edge of graphene at the atomic scale, including pentagons, heptagons and octagons. These defects modulated the local electronic environment and perturbed the surface properties of the graphene, such as the specific surface area and hydrophobicity. Authors showed that DG has higher catalytic activity

than original graphene sample and studied the role of these defects for different electrochemical reactions, including ORR, OER and HER.

2.8.4 Transition Metals Incorporated in Hetero-doped Carbon Structures

TMCs supported on carbon structures have long been of high interest due to their low cost, abundance, facile synthesis, and have demonstrated to catalyze oxygen reduction reactions[22], oxygen evolution reactions[10], and hydrogen evolution reactions[23], which make them ideal candidates for their use in PEMFCs, RFCs and RMABs. This is especially the case for heterogeneous transition metal-based catalysts, which are often complexed with hetero-doped carbon. The synergy between metal and hetero-doped carbon can form complexes such as, CoP-N-C and Fe-N-C that have been known to catalyze oxygen reactions.[3,49–51] The chemical bonds that are formed between metal atoms and supports can also enhance the stability of single metal atoms and anchor metals sites to prevent agglomeration.[52] Moreover, the catalytic capabilities of these materials is also associated with the defects that they can incur.[53,54]

One defect that has been widely studied on heterogeneous transition metal (TM) based electrocatalyst has been oxygen vacancies. The concentration and distribution of oxygen vacancies can adjust the bandgap or charge distribution of the materials. The presence of vacancies is known to improve the kinetics of adsorbing reactants because the electronic energy profile can be tailored by changing the concentration of oxygen defects.[55] Aijaz et al. showed that with the formation of oxygen vacancies in the reduced form of Co_3O_4, the two electrons that previously occupied the oxygen 2p orbitals, became delocalized around the adjacent three Co^{3+}.[17] In comparison to pristine Co_3O_4, the defect-rich Co_3O_4 resulted in an improved OER performance. Wang et al. reported that cation vacancies can also influence the electrocatalytic performance of heterogeneous transition metal (TM) material.[56]

2.8.5 Transition Bimetal Electrocatalyst

Even though there is a great benefit with the TM incorporated onto hetero-doped carbon, monometallic TM atoms are usually optimal to the electrocatalysis of a specific reaction rather than multiple reactions. Thus, promoting bifunctionality in monometallic transition metals is challenging. Transition bimetals incorporated on hetero-doped carbon supports have the benefits of binary metal composites and multi-valence species available to catalyze multiple reactions.[57,58]

Other characteristic of bimetallic material, like spinel structures, can promote uncoordinated metal sites between with carbon based ligands, which not only expose the metal site but promotes an optimal occupancy of octahedral sites that help promote the adsorption of reactants during OER.[59] Furthermore, metal-metal interactions can help anchor metal centers, which helps increase catalytically active metal utilization for catalysis.

2.8.6 Metal Organic Framework-derived Carbon

In addition to being doped with other materials, TMs can be complexed with organic linkers to form what are known as metal organic frameworks (MOFs). MOFs are orderly structured material with high surface area and contain uniform open pores that can expose active metal sites. In the past few years, MOF-derived nanostructures have garnered attention for their electrocatalytic abilities. These structures can also benefit from defects for high electrocatalytic performance.[22,60,61]As mentioned for bimetallic materials, MOFs have the advantage of having mixed valency between the two metals because they can tune the electrocatalytic activity by creating defects. Similarly, bimetallic structures derived from MOFs have the same advantage. It has been shown that a mixture of different metals can result in unsaturated coordinated sites that are beneficial for catalysis. An example would be Co-Ni ultrathin nanosheets that are composed of MOFs. Duan et al. complexed nickel and cobalt metals with benzene dicarboxylic acid (BDC) organic linker to form a MOF,[15] which has crystal defects with unsaturated metal sites on the surface and partially terminated BDC coordination

bonding. Such coordinated unsaturated metal sites are active metal sites, which resulted in exceptional OER performance with a very low overpotential.

2.8.7 Experiments to Understand the Active Sites and Reaction Mechanism

From the literature it is evident that TM-based materials show a great promise to replace noble metal-based electrocatalyst for OER and ORR. However, transition metal based catalysts often contain non-uniform aggregates of metals.[37] This results in only a small fraction of transition metal atoms that are catalytically active and exposed to reactants, which is not favorable for efficient electrocatalysis per mass.[37] Incorporating TMs in hetero-doped carbon supports creates synergistic interactions that help disperse transition metal active sites, prevent their agglomeration, and promote defects that are beneficial for the catalysis of both ORR and OER.[62] In addition, multi-metallic system overcomes the limitation of monometallic transitional metal atom-based catalyst in terms of catalytic ability.

Having more than one metal can exhibit binary metal composites and multi-valence species available to catalyze multiple reactions.[57,58] Therefore, creating transition bimetal sites on carbon structures can increase utilization and bifunctional catalytic activity of electrode material, overcoming the relatively low activity of single-TM catalysts.[35,63] A multi-metallic species often induces a synergetic effect results in a facile charge transfer between dissimilar metals and a decrease in the kinetic energy barrier from modulation of electronic structures.[63] For these reasons, bimetallic transition metals embedded N-doped carbon systems have savored various beneficial effects for multifunctional electrocatalysis,[64,65] not limited unifunctional ORR catalysis.[66,67]

3. OVERIEW OF MATERIAL SYNTHESIS AND CHARACTERIZATION

3.1 Material Synthesis

Both physical properties (including shape, surface area, and dispersion of active materials) and chemical properties (type and concentration of defects, interfacial nature, etc.) of a catalyst are critical factors of overall catalytic performance of the material.[68,69] Crystalline nanostructures are often used as electrocatalytic material because their organized structure can provide enhanced electric conductivity and optimized dispersion of catalytically active sites, and allow for easier characterization of material structure (compared to amorphous structures) facilitating further optimization of the material for performance.[70,71] This study will be focused on both solution-based and vapor transport-based nanostructure synthesis methods. For these types of the synthesis methods the molecular and crystal structure in a material is often dictated by the process of nucleation and growth, synthesis parameters such as temperatures, pressure, and the starting material that is chosen. Controlling these processes can lead to an electrocatalytic material with desired physical and chemical properties for electrochemical energy conversion and storage.

3.1.1 Nucleation and Growth

Nanostructure and nanoparticle synthesis ultimately starts off with nucleation. Classical nucleation theory consists of two modes of nucleation (homogenous and heterogeneous), and the rate of nucleation is primarily determined by the kinetics and thermodynamics of a reaction. Homogeneous nucleation is mostly hard to achieve because it requires a simultaneous nucleation throughout the surface (or interface). Therefore, heterogeneous nucleation occurs in most cases. It starts by forming a wall of transformed material and then nucleates towards the inside of those walls regardless of the nucleation type (e.g. liquid-to-solid transformation, a transformation into a different solid phase, etc.).

Generally, the thermodynamics of forming certain material during nucleation depends on a range of parameters as seen in the equation below.[72]

$$\Delta g = -\left\{\frac{[(4/3)\pi r^3]}{\Omega}\right\} + 4\pi r^2\alpha \ (homogeneous\ nucleation)$$ Equation 3.1

where $r = 2\Omega\alpha \ / \ kT\sigma$

$$\Delta g_n = (16/3)\pi\alpha^3(\Omega/k_BT\sigma)^2 \ (heterogeneous\ nucleation)$$ Equation 3.2

where Δg_n represents the Gibbs free energy of nucleation, α is the interfacial free energy, Ω volume per molecules, k_B is Boltzmann constant, r is the critical radius and T is temperature. These simplified equations reveal the critical parameters needed to synthesize a material with specific nanostructure and morphology. One of the focuses of synthesizing electrode material is to create nanostructure material with defects, morphology and crystallinity that will promote the adsorption, chemisorption and separation of reactants involved in ORR, OER and HER.

3.1.2 Solvothermal Method

The solvothermal method involves dissolving a set of precursor or reactants in a solvent, and then having the resulting solution undergo a heat treatment in a pressurized autoclave. This environment enables crystallization, particle/crystal growth, and change in pore size volume. A solvothermal process is used to make single crystals, nanocrystals and thin films.[73] It is often used because of the simplicity and its capability to prepare thermodynamically stable and metastable states of a material (or a composite) that would be difficult to form with other methods.

The overall material synthesis using the solvothermal method is controlled by different parameters including: solvent, precursor concentration, kinetics of crystal formation, temperature and pressure. Materials such as metal organic frameworks, zeolites, metal/oxide nanoparticles, and other hybrid materials are synthesized using this method.[74,60,75] In general, solvothermal method is a facile, scalable and cost effective approach of synthesizing hybrid materials for many applications including catalysts.

3.1.3 Atomic Layer Deposition

Atomic layer deposition (ALD) is a type of vapor deposition that has unique advantages over the other vapor deposition methods. While others vapor deposition methods run on a continuous flow of precursor, substrates in an ALD process are exposed to a sequence of precursor pulses. After a precursor gas is fed into the reaction chamber, adsorbed on the substrate, and reacted with the substrate surface, all the unreacted precursor and products generated by the reaction will be purged away by an inert gas flow. The precursors used in ALD are designed to only react with the specific sites on a substrate's surface, and not react with each other. Therefore, the reaction is self-limiting, and a deposition beyond a single atomic layer per cycle is prohibited in an ideal ALD mode. After the first reaction followed by purging process, a second set of precursor gas will be introduced to the chamber and react with the substrate surface. This digitized process, as opposed to a continuous introduction of reactant, enables a highly accurate thickness control down to atomic scale, even on a substrate with highly complicated geometry. Commonly used precursors in ALD are organometallic compounds that help promote self-limiting surface reactions. The surface chemistry of the substrate affects the deposition behavior and kinetics during ALD.

ALD has been used in a range of applications including batteries, fuel cells, photovoltaics, catalysis, semiconductors, and other electronics devices. ALD can aid in functionalization of material surfaces by forming ultrathin film or nanoparticles with size control down to the atomic scale. Since electrocatalysis is a highly surface-sensitive process, the ALD-based approach should provide ample opportunities for catalyst development.

As briefed, ALD growth is a multi-step process as follows: [76]

1. The substrate inside the chamber is exposed to a gaseous metal precursor for a certain amount of time. The reaction of a metal precursor with the substrate is referred as the first half reaction, during which the ligands of the metal precursor are partially removed by reacting with the active sites on the substrate surface.[77] After the first half reaction is completed, the pulsing of the precursor is stopped. If

the pulse time is enough for deposition, the molecules of the precursor will be allowed to react with all the sites on the substrate surface, and one atomic layer of precursor molecules will be covering the surface.

2. The chamber is purged using an inert gas such as nitrogen and argon to remove gaseous products and any unreacted reactants.

3. Then a second metal precursor or oxygen/nitrogen/sulfur source introduced into the chamber for a subsequent reaction, which is either to deposit a second metal or to oxidate, nitrate or sulfate the metals deposited in the first cycle. Simultaneously another reactive functional group is formed on their surface during the reaction for the subsequent (first) precursor to react with it. Usually, oxygen functional groups such as hydroxyls react well with ligand and metal center in a precursor, which allows the metal site to bind to the substrate surface.[78]

4. Step 2 is repeated using the same inert gas.

Steps 1-4 is considered as one full cycle. In an ideal case, the number of ALD cycle should be linearly proportional to the resulting thickness of the film. However, the deposition rate (i.e. thickness per full cycle) varies depending the precursor, substrate material and temperature.

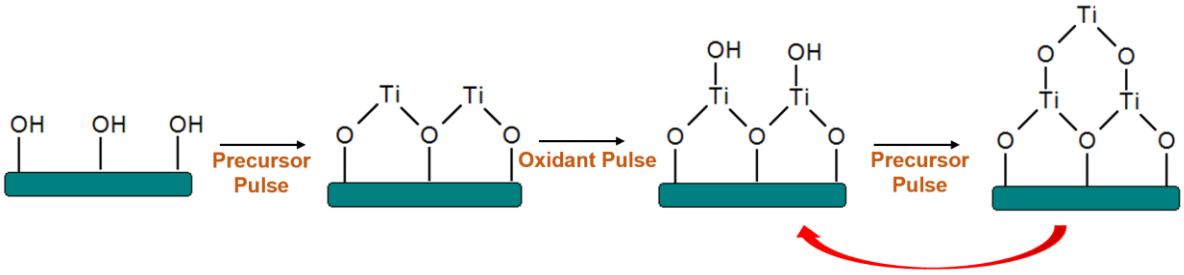

Figure 3-1 schematic diagram depicting the ALD process of depositing titanium oxide on a hydroxylated substrate.

3.1.4 Metal Organic Framework (MOF) Synthesis

The main goal in MOF synthesis is to execute a synthesis procedure that will result in a well-defined structure. In addition, the kinetics of crystallization must be ideal for the growth and nucleation of a desired phase.[79] Selecting an ideal organic ligand and metal-ion center is an important factor in this process. The organic linkers that are part of MOFs are usually Lewis's base–binding atoms (functional groups) such as halides, nitriles, cyanides, anionic organic molecules (benzenedicarboxylic acid), and neutral organic molecules.[80] The characteristics of resulting MOFs such as pore size and shape is critically dependent on the choice of organic ligand due to differences in the length and the types of functional groups.

Selecting optimal metal ions for MOF synthesis depends on the electrocatalytic activity and the overall function that is desired. Most of transition metals (TMs) can be used to form a MOF. TMs are the group of metals whose block d. Therefore, they are very active and flexible in coordination numbers and oxidation states, which makes them ideal for their application as an electrocatalytic material.[81,82] Because of this, MOFs have a diversity of geometrics such as square–planer, tetrahedron, octahedron, trigonal and pentagonal. For MOF synthesis, the coordination reaction typically takes place between the metal salt and the ligand in the presence of one or more organic solvents such as dimethyl-formamide (DMF), ethanol, and methanol. Based on the reaction condition, the end-product, MOF is produced in different geometric shapes. Non-solvothermal methods of synthesizing MOFs, such as those performed at ambient temperature and pressure, are often known as precipitation reactions. These reactions usually consist of short-time scale crystallization. Both of these synthesis methods are used for this study.

3.2 Material Characterization

Material characterization is divided into two parts. One of the material characterizations is focused on characterizing the material composition and structure while the other focuses on the electrochemical characterization to understand the process-property-performance correlation.

3.2.1 Electron Microscopy

3.2.1.1 Scanning Electron Microscopy (SEM)

Scanning electron microscopy (SEM) uses a focused electron beam to scan over the surface of a material, which gives off various signals after interacting with different depths within a specimen. The depth of interaction is known as the interaction volume. Usually, the size of the interaction volume depends on the accelerating voltage of the primary electron beam and the atomic density of the specimen. The electron beam's accelerating voltage can range from as low as 0.1 kV to 30 kV, and the types of signals given off at different depths include: auger electrons, secondary electrons (SE), characteristic x-rays, backscattered electrons (BSE) and Bremssarahung x-rays. The SEMs used in the studies presented here are a field emission gun-SEM (Zeiss Gemini 500 FEG-SEM) and an environmental SEM (FEI XL30). Both SEMs have various detectors including in-lens detector, secondary detector, and backscatter detector. The latter, FEI XL30 SEM, is the only one equipped with a energy dispersive X-ray (EDX) spectrometer for detecting the characteristic X-rays given off by the material.

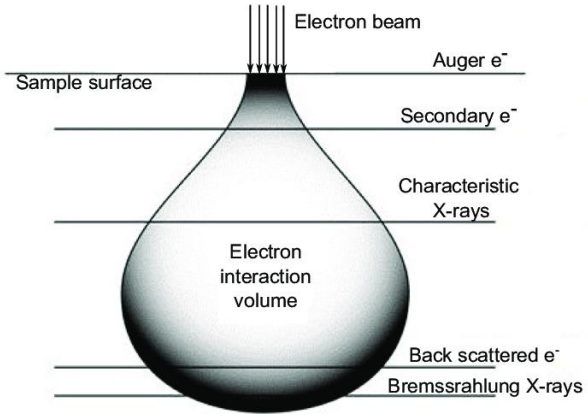

Figure 3-2 shows the 'interaction volume' of the electron beam and sample

Since most of the materials discussed here are largely composed of carbon it was difficult to operate with a high accelerating voltage. With this, and with carbon having a comparatively lower atomic density, the interaction volume was smaller, and therefore

the types of signals obtained were mostly pertaining to the topography and the surface morphology of the specimens. Both the in-lens and secondary electron detectors were used for these low accelerating voltages, which were usually less than 1 kV to capture overall morphology of the materials presented in the SEM micrographs. Operating at low voltage has the advantage of obtaining the surface signals of the material without the noise given off by more signals due to a larger interaction volume. In addition, operating at this low accelerating voltage also prevents the burning of a mostly carbon specimen. Although, doping and the incorporation of transition metals and transition metal oxides, made the carbon structure conductive, they were still susceptible to burning. However, operating at low voltage can also give less signal that overall can affect the image quality and resolution, especially at higher magnifications.

3.2.1.2 Transmission Electron Microscopy (TEM)

In contrast to SEM, TEM image development does not come from the raster of the electron beam over the specimen, but rather as the name indicates, the image is developed from the interaction of the beam with the specimen and the resultant transmission that is then projected onto a fluorescent screen. However, like SEM the electron beam and specimen interaction have an interaction volume, and usually the signal that transmits through the sample is composed of inelastic scattered, elastic scattered and unscattered electrons. Aside from the transmitted signal there is also backscattered electrons, secondary electrons, auger electrons, cathodoluminescence and characteristic x-rays. Although there are other differences between SEM and TEM, one of the most obvious is that the working voltage is higher (up to 200 kV). In addition, the resolution of TEM can reach to a fraction of a nanometer, which is smaller in comparison to SEM.

For TEM there are different types of imaging modes. In high-resolution TEM imaging, an objective aperture is not used, so that unscattered electrons recombine to form a phase contrast image. In standard TEM dark-field imaging, the objective aperture excludes unscattered electrons, so there are areas that appear brighter as a result of their thickness and higher atomic number. In standard TEM bright-field imaging, an objective

aperture placed between the objective lens and its image. In turn, this set-up aids in excluding scattered electrons from contributing to the image.

Energy-filtered transmission electron microscopy (EFTEM) imaging techniques can utilize properties of loss spectrum energy to increase contrast, reduce chromatic aberration, and increase depth perception. The contrast seen in images and diffraction patterns comes from the removal inelastically scattered electrons that produce fog. EFTEM can create elemental/chemical maps at nanometer resolution by forming images with inelastically scattered electrons.

3.2.1.3 Energy Dispersive x-ray spectroscopy (EDS, EDX or EDXS)

EDS is an analytical tool that is equipped in both SEM and TEM. EDS is mainly used to get the elemental composition and chemical characterization of a sample. The way that EDS works is that the electron beam is focused on the sample, which excites an electron from the inner shell. This causes electron to eject from the shell creating an electron hole. Then an electron from a higher energy shell will fill the hole that was creating. The resulting X-ray emission is due to the energy difference between the higher-energy shell and the lower energy shell. The energy difference between the two shells is related to atomic structure, which allows for elemental composition to be measured.

3.2.2 Fourier Transform Infrared (FTIR)

Fourier-transform infrared (FTIR) spectroscopy measures the infrared spectrum of transmittance or absorbance of a sample that is exposed to a wide range of wavelengths of infrared radiation. Some of the IR radiation is absorbed by the sample while some passes through. The energy absorbed or transmitted by the sample is related to the different vibrations of chemical bonds which include stretching and bending. By measuring the wavenumbers of the energy absorbed by a particular sample, chemical bonds within the sample are identified.[83] Unlike dispersive spectroscopy where a monochromatic beam is used, FTIR collects signals with a wide range of wavelengths simultaneously and process the raw data by leveraging Fourier transform.

3.2.3 X-ray Diffraction (XRD)

XRD measures the diffraction of x-rays that interact with a material. Some would consider the X-ray diffraction a reflection rather than a diffraction. The general mechanism of XRD consist of two incident X-ray that interact with the sample and then are diffracted. The reflected X-rays can have either constructive or deconstructive interference which is then picked up by a detector. The X-ray interference in XRD is usually represented by the known Bragg's Law equation () which shows the relationship between the wavelength (λ), the scattering angle of the x-ray (θ) and lattice spacing (d). The d-spacing can then be used to determine the different atomic planes present using Miller indices. However, as crystal structures get more complex it gets more difficult to use the d-spacings solely to determine the different atomic planes present. Therefore, to determine the different atomic planes and phases present in XRD spectra we compare it to with a reference from a database. The most used databases are maintained by the International Center of Diffraction Data (ICCD).

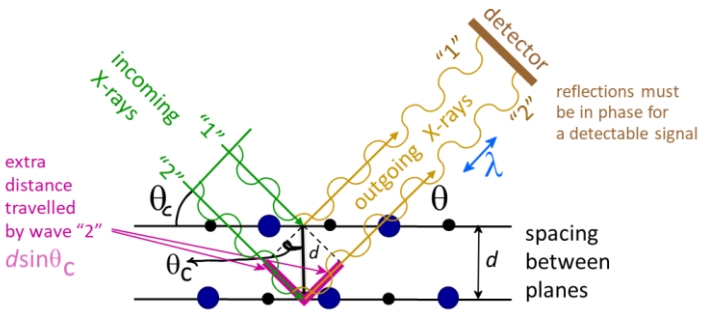

Figure 3-3 shows the X-ray interference that occurs in XRD

3.2.4 X-ray Photoelectron Spectroscopy (XPS)

X-ray photoelectron spectroscopy (XPS) is a surface-sensitive spectroscopy technique that allows for elemental analysis and characterization, which includes chemical states, electronic states, and electronic densities. Based on the photoelectron effect, XPS not only can identify the atomic composition of our electrode but can potentially help unveil the stoichiometry found in the metal oxide of the electrocatalytic

material. Furthermore, XPS can also help identify the complexation of the transition metals with other atoms such as oxygen, carbon, and nitrogen.

The energy of the x-ray (Al $K_{\alpha,}$ E_{photon} = 1486.7 eV) used in XPS is usually has a known wavelength and kinetic energy is known. Therefore, the electron binding energy of the emitted electrons can be calculated by using the photoelectric effect equation:

$$E_{binding} = E_{photon} - (E_{kinetic} + \phi) \quad \text{Equation 3.3}$$

Where ϕ is the work function term for the specific surface of the material. Generally, the XPS spectra generated (which is usually counts vs. binding energy) is related to the number of electrons detected at certain binding energies, and each peak in the spectra is corresponding to the electron configuration of the atom's electrons.

The bindings energies of each peak can be identified using a database such as those found in National Institute of Standards and Technology (NIST), which will characterize specific elemental and electronic states for specific elements. The peaks of each XPS spectra are found by doing fittings. There should not be any binding energy shifts before doing a peak fitting, which could be verified by the C 1s peak that is usually around 284.6 eV. Peak fittings in these studies were done using XPSPeak and having some knowledge of peak position for each corresponding elements. The main parameters that are adjusted are binding energy, full width at half maximum (FWHM), chemical shifts and peak shapes.

The atomic concentration (atom %) for each type of different elemental components for each spectrum (C 1s, N 1s, O1s, Co 2p, and Cu 2p) can be determined from relative peak areas and the corresponding sensitivity factor (for Al K-alpha x-ray) according to:

$$atom\% = 100(A_i \,/\, s_i) \,/\, \Sigma(A_i \,/\, s_i) \quad \text{Equation 3.4}$$

where is the peak area of the element *i* and is the sensitivity factor for each element.

3.3 Electrochemical Measurements

For this study, an electrochemical analyzer (Biologic SP-200; potentiostat/galvanostat and impedance spectroscopy) is mainly used to perform cyclic voltammetry (CV), linear sweep voltammetry (LSV) and electrochemical impedance spectroscopy (EIS). A rotating disk electrode (RDE) apparatus (ALS RDE-3A) and a rotating rind disk electrode (RRDE) apparatus (ALS RRDE 3-A) were used to obtain LSV at different rotational speeds. For all electrochemical measurements, a three-electrode set-up was used to gauge ORR, OER and HER capabilities of synthesized materials. In the three-electrode set-up, a 0.3 mm glassy carbon electrode (GCE) was deposited with sample, which served as the working electrode. A platinum wire or graphite rod was used as a counter electrode, and silver-silver chloride (Ag/AgCl) in saturated potassium chloride or mercury-mercury oxide (Hg/HgO) in 1 M sodium hydroxide were used as reference electrodes.

3.3.1 Cyclic Voltammetry

Cyclic voltammetry (CV) is a potential-sweeping technique that measures the resulting current from the cell of test. The controlled potential is applied at a specific rate within a desired potential window in a cyclic fashion. A potential sweep towards higher anodic potentials gives rise to an oxidation current while reduction occurs as the potential is being cycled back towards the cathodic potential. CV usually provides an initial assessment about the relative amplitude of electrochemically active surface area, presence of specific redox reactions and their relative activity.

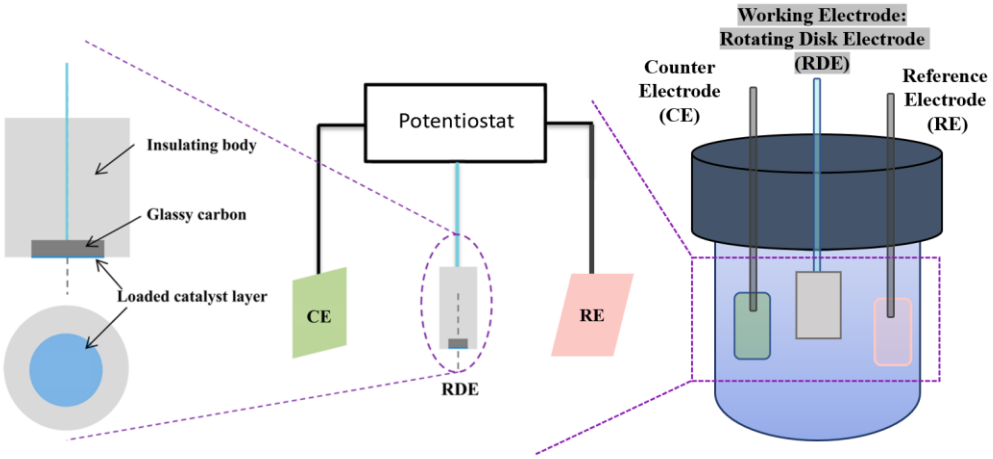

Figure 3-4 is a diagram of the three-electrode set-up of electrochemical testing showing the working, reference and counter electrode

3.3.2 Linear Sweep Voltammetry with RDE and RRDE measurements

Linear sweep voltammetry (LSV) is commonly used with a rotating disk electrode (RDE) and rotating ring disk electrode (RRDE) to gauge the catalytic capabilities of materials in a quantitative way. In general, LSV curves (after compensating the overpotential originated from ohmic loss) provides an overview of the electrocatalytic performance of the electrode material (Figure 3-5), and allows for the extraction of the Tafel slope, an indication of catalytic activity.[84]

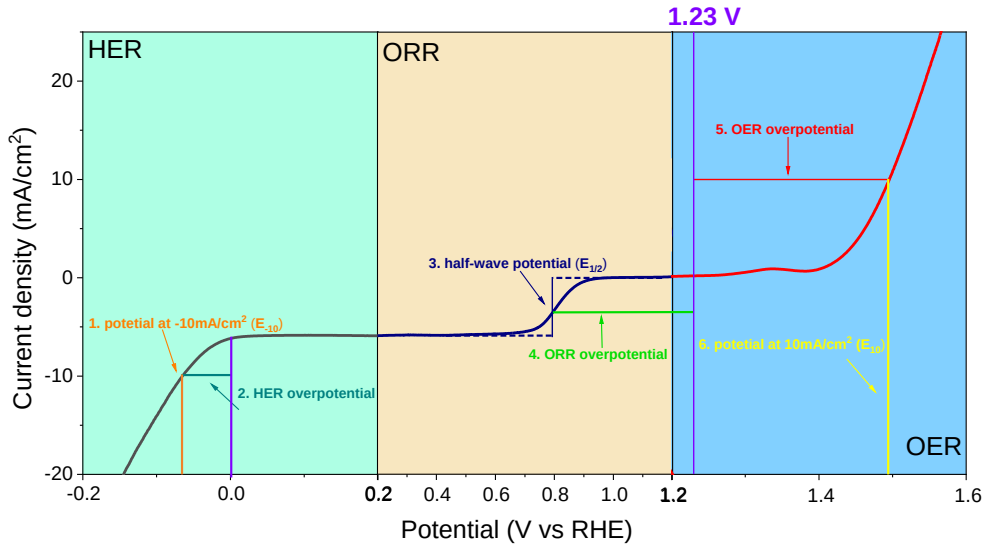

Figure 3-5 a general overview of the type of information that could be extracted from a LSV curve

The RDE allows for the convective flow of reactant to the surface of the working electrode thus creating a steady-state diffusion where the mass transport dependent current, i_l, can be described with the following Levich equation:

$$\mathrm{i_l} = \mathrm{nFAD}^{2/3}\omega^{1/2}\nu^{-1/6}\mathrm{C}^{*} \quad \text{Equation 3.5}$$

where n is the number electron moles, F is Faraday's constant, D is the diffusion coefficient of the reactant, C^* bulk concentration of the reactants, ν is the kinematic viscosity of the solution, ω is the angular frequency of rotation, and A surface area.

This equation can then be combined with i_k, which is the kinetically dependent current which results in the Kourtecky-Levich equation that describes the current from electrochemical reaction dependent on kinetics and mass-transport:

$$\frac{1}{\mathrm{i}} = \frac{1}{\mathrm{i_k}} + \frac{1}{\mathrm{i_l}} \quad \text{Equation 3.6}$$

Often the constants terms ($nFADvC^*D$) of i_l are combined in one term, B, known as the Levich slope. This value can be obtained by plotting the reciprocal current of the sample versus the reciprocal of the rotational frequency. From the Levich slope, the number of electron moles can be calculated by dividing the slope by all the constants except for n, which is what we are solving for.

In addition, RRDE can also give off additional information due to the set-up with a platinum ring, which allows for discerning different types of reactions that are occurring during the experiment. A certain volume of catalyst ink (the catalyst loading was usually 0.4 mg/cm^2) deposited on the surface of the rotating disk electrode (RRDE), which is composed of a glassy carbon disk (D= 4mm, A= 0.126 cm^2) enveloped by a Pt ring (ID/OD: 5/7 mm).

Both the glassy carbon disk and the Pt ring's current were recorded simultaneously. The LSV measurements were collected on the RRDE at a rotation of 1600 rpm with a scan rate of 5 mV/s. The Pt ring's current was recorded by applying a constant potential of 0.3 V. The electron transfer (n) deduced from the reduction of O_2 molecules at the disk and the reduction of HO_2^- at the ring can be calculated by the following equation[41]:

$$n = 4 \times \frac{I_D}{I_D + I_R/N} \quad \text{Equation 3.7}$$

Where I_D and I_R are the disk and ring currents (Fig.S7). N is the collection efficiency, which is obtained by taking the ratio of the I_D and I_R in 0.1 M KOH with 10 mM $K_3Fe(CN)_6$ electrolyte.

The HO_2^- percentage was calculated using the following equation:

$$HO_2^-\% = 2 \times \frac{I_R/N}{I_D + I_R/N} \quad \text{Equation 3.8}$$

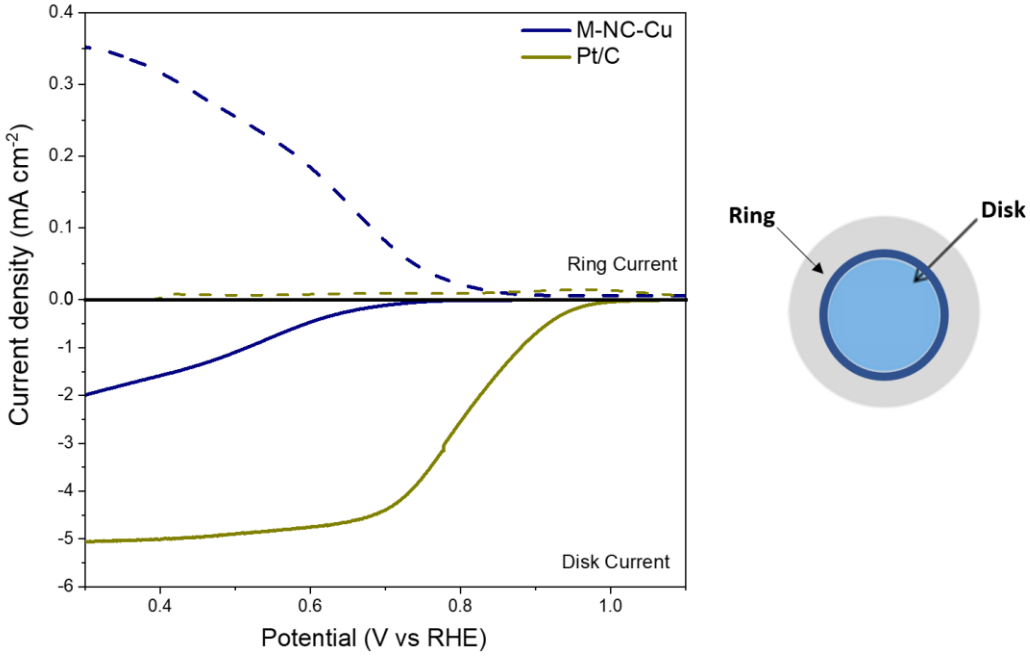

Figure 3-6 shows (left) the LSV of both ring and disk electrodes and (right) a diagram of the RRDE components

3.3.3 Tafel Slope

The Tafel slope is an approximation of the Butler-Volmer equation that can be done at overpotentials usually larger than 50 mV. At a large enough overpotential the second exponential is negligible because it is presumed that applying a high overpotential (or at least higher than 50 mV) will be favoring the forward reaction, or in other words the production of reactant to products and thus becoming an irreversible reaction process. The resultant B-V turns into $j= j_0 e^{\alpha nF\eta/(RT)}$ Equation 2.16 (which is discussed in Chapter 2), and by plotting the region associated with this equation, and fitting a line we get the Tafel equation (Equation 3.3). From the linear fitting we can get the Tafel slope, which shows the relationship between overpotential and current density.

$$\eta_{act} = a + b \log (j) \quad \text{Equation 3.9}$$

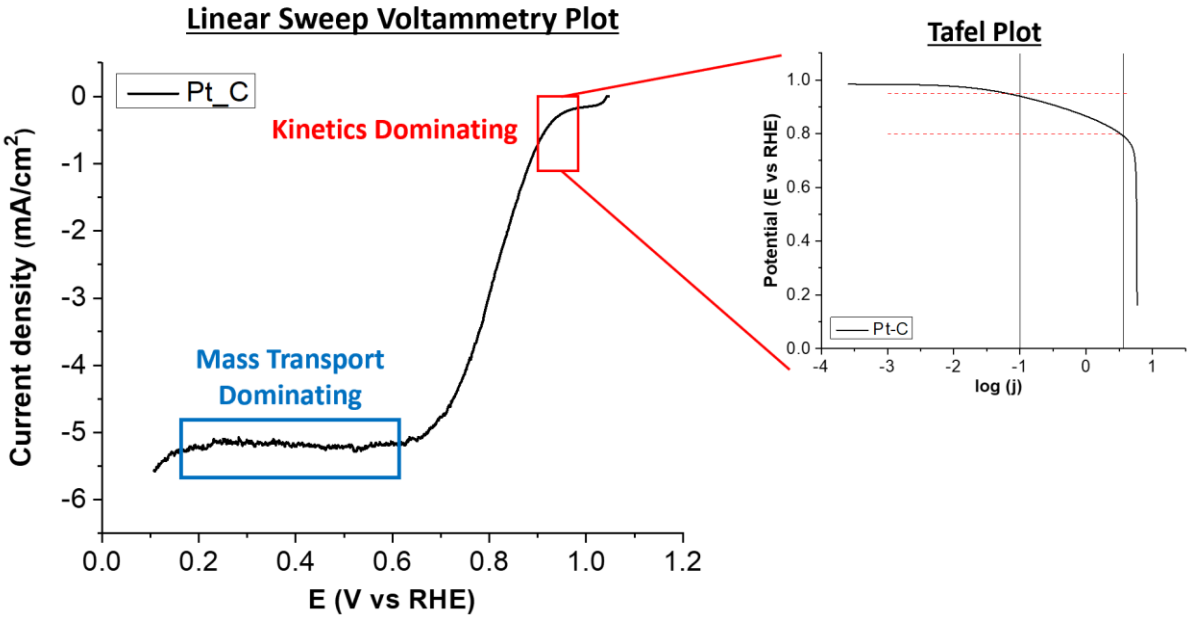

Figure 3-7 shows the region from an I-V curve that is chosen to do the linear fitting for finding the Tafel slope

3.3.4 Quantification of electrochemical active surface area (ECSA)

The ECSA was characterized using cyclic voltammetry (CV) in 0.1 M KOH electrolyte saturated with N2. The CVs were cycled from -0.2 to -0.3 V vs Ag/AgCl/KCl (3.5 M) for scan rates12 to 40 mV s-1 in intervals of 4 mV s-1. This potential range was chosen because of its non-faradaic characteristics. J_{anodic} and $J_{cathodic}$ values were obtained at -0.25 V and then plotted vs scan rate. The slope was obtained from a linear fitting on the plot, which was used to find the double-layer capacitance (C_{dl}). The ECSA can be calculated using the following equation:

where A is the geometric area of the electrode (0.071 cm2), and C_{ref} is the referential areal capacitance of flat electrode (80 mF/cm^2)[3].

$$ECSA = \frac{C_{dl}\,A}{C_{ref}} \quad \text{Equation 3.10}$$

4. CO-CU BIMETALLIC METAL ORGANIC FRAMEWORK FOR ELECTROCATALYSIS

4.1 Introduction

The advancement of electrochemical energy conversion technologies such as fuel cells, water splitting systems and metal-air batteries is heavily reliant upon a range of functionalities for three essential electrochemical reactions – hydrogen evolution reactions (HER), oxygen evolution reaction (OER) and oxygen reduction reaction (ORR).[85–87] Noble metal-based catalysts have been widely used for HER (Pt), ORR (Pt) and OER (Ir and Ru) owing to their excellent electrocatalytic activity, but their high cost, scarcity, and low stability drives active development of alternative catalysts.[86,88]

Transition metals (TM) and their oxides (TMO), among many, have been widely studied as a typical class of non-noble metal-based hydrogen and oxygen electrocatalysts due to the cost-effectiveness and multi-valence, along with their tunability of chemical composition, structure and morphology.[35,36] Cobalt (Co) is one of the most commonly used TMs for bifunctional oxygen electrocatalysis [14,17,89] partially because of their tendency to better absorb reactants for each reaction (i.e. O_2 for ORR; OH^- for OER, and H_2O for HER).[35] To augment electrical conductivity and catalytic activity, as is the case for many other TM/TMO-based catalysts, Co and CoO_x nanoparticles are often dispersedly embedded into carbon-based structures for bifunctional electrocatalysis.[89–91] On the other hand, copper (Cu) is theoretically predicted to exhibit one of the best ORR activities among TMs, and [92] copper oxides (Cu_xO) have shown good HER activity due to its low energy barrier for hydrogen adsorption.[93,94] Even though metal nanoparticles exhibit good electrocatalytic activity, due to having a larger active surface area, they often have high surface energy and fast nucleation that makes them prone to agglomeration.[95–97] To address the issue of Cu being readily agglomerated, researchers have used N-doped carbon as the template to stably anchor tiny Cu species.[67,98,99] The

approach also rendered excellent ORR performance, which is mainly ascribed to rich Cu-N_x bonds within the hybrid matrix.[36]

To overcome relatively low activity of single-TM catalysts, bimetal-based systems have attracted significant recent attention.[35,63] A multi-metallic species often induces a synergistically enhanced catalytic activity due to a favorable rearrangement of electronic structures to reduce kinetic energy barriers.[63] In addition, the introduction of a secondary metal can deter the overall agglomeration kinetics of each metal during the pyrolysis of metal-organic frameworks (MOFs),[100] a widely used approach in synthesizing TM-supporting N-doped carbon.[64] All the aforementioned studies considered, it is a reasonable approach to design bimetallic Co and Cu-embedded N-doped carbon systems for trifunctional electrocatalysis. There have been several recent studies on the use of Co/Cu-based bimetallic hybrids for monofunctional or bifunctional catalysis of HER, ORR and/or OER, but there has not been a report on the trifunctional capability.[13, 20, 23–28]

Herein, this study demonstrates a new facile MOF-based process to realize an efficient trifunctional catalyst where tiny Cu species are uniformly dispersed in Co/CoO_x-embedded N-doped carbon. The amino terephthalic acid organic linker used in this study not only has the carboxylic acid sites where the metals could complex but also has an amine group that can complex with metal centers and provides a nitrogen source for doping carbon.[104–106] It is believed that Co-anchored N-doped carbon acts not only as an efficient OER catalyst but also as an inhibitor of Cu agglomeration for both ORR and HER. The hybrid system also has $CuCo_2O_4$ clusters (for ORR and OER) in addition to Cu-N_x, Cu-O_x (for HER and ORR), and Co-N_x complexes (for OER) in a N-doped carbon structure for further enhanced catalytic activity. The resulting heterogeneous material renders a hierarchical structure for both efficient mass transport and large surface area that demonstrates active trifunctional catalysis for ORR, OER and HER in alkaline solution.

4.2 Experimental

4.2.1 Metal-organic hybrid synthesis

0.75 mmol of $CoCl_2 \cdot 6H_2O$ (98%, Alfa Aesar) and 0.75 mmol $CuCl_2 \cdot 2H_2O$ (99+% ACS grade, Alfa Aesar) were dissolved in 20 ml of dimethylformamide (DMF, 99.8+% ACS grade, Alfa Aesar) and sonicated for 20 min. Then 1.5 mmol of 2-aminoterephthalic acid (99%, ACS grade, Alfa Aesar) was added to the solution and sonicated for an additional 20 min. The solution was transferred to a 40 ml autoclave for the solvothermal reaction at 140 ºC for 24 h under airtight conditions. The solid was collected and rinsed several times via centrifugation using DMF, water and ethanol. After being air-dried, the sample was dried further at 150 ºC under N_2 conditions for several hours. By heat-treating the resulting solid at 800 ºC for 2 h in N_2, a N-doped carbon with Co and Cu (we name it M-NC-CoCu; M-NC meaning MOF-derived N-doped carbon) was obtained. Two other variants of study, M-NC-Co and M-NC-Cu were prepared via the same approach by starting with $CoCl_2 \cdot 6H_2O$ or $CuCl_2 \cdot 6H_2O$, respectively, instead of both. It is noted that two more batches of samples heat-treated at 700 ºC and 600 ºC were also characterized, but those pyrolyzed at 800 ºC are mainly discussed in this report due to their higher catalytic performance.

4.2.2 Material Characterization

Transmission electron microscopy (TEM) and scanning transmission electron microscopy (STEM) images were recorded on a 200 kV FEI monochromated F20 UT Tecnai system. The STEM image was acquired with a convergence angle of 10 mrad and a detection angle of 30 mrad. Energy filtered transmission electron microscopy (EFTEM) was used to visualize elemental distribution. Sample preparation for TEM samples included drop-casting ethanol-suspended catalyst upon a 3 mm Lacey B Carbon 400 mesh grid from Ted Pella, followed by ambient drying. X-ray photoelectron spectroscopy (XPS) was performed on a PHI Quantum 2000 system using a focused, monochromatic Al Kα X-ray (1486.6 eV) source for excitation and a spherical section analyzer (200 μm diameter X-ray beam incident to the surface normal; detector set at 45°). The collected

data were referenced to an energy scale with binding energies for Cu $2p_{3/2}$ at 932.7 ± 0.1 eV and Au $4f_{7/2}$ at 84.0 ± 0.1 eV. For XPS, catalysts were dispersed in ethanol and drop-cast onto a cleaned Si wafer. X-ray diffraction (XRD) pattern was recorded by a PANalytical X'Pert PRO with Co Kα radiation (λ = 1.7890 Å) at a step size of 0.02º and scanning rate of 0.04º s^{-1}. The obtained data were converted to Cu Kα radiation (λ = 1.5406 Å)-based spectra for facile comparison with other reports. The dried powder sample was placed on the surface and flattened on the surface of a MTI P-type Boron doped Silicon Zero Diffraction Plate. FT-IR samples were dried under vacuum for 24 h by placing samples in a desiccator overnight and placed on a diamond crystal (Nicolet 380 system, Thermo Scientific).

4.2.3 Electrochemical Characterization

The catalytic activity was evaluated with linear sweep voltammetry (LSV) using a potentiostat (SP-200, Bio-Logic Science Instruments) in either ring-disk electrode (RDE) or rotating ring-disk electrode (RRDE) setup (RRDE-3A, ALS Co. Ltd). Measurements were performed in a three-electrode setup with a graphite rod as the counter and Ag/AgCl (3.5 M KCl) or Hg/HgO (1 M NaOH) electrode as the reference electrodes. The working electrode was prepared by drop-casting each electrode ink onto a glassy carbon (GC) disk electrode or nickel (Ni) foam. The ink was prepared by immersing 5 mg of hybrid catalyst materials into 1 ml of 2:1 volume of ethanol to MiliQ water along with 10.75 µl of 5 wt% Nafion (Nafion D-521, Alfa Aesar). For Pt/C electrode, a 5 mg ml^{-1} Pt/C suspension was prepared by using a commercial 20 wt% Pt supported on carbon black (Vulcan XC72). These samples were dried under N_2 at 2 standard cubic feet per hour (scfh). The loading mass for all samples measured on glassy carbon was 0.4 mg/cm^2. Then, O_2 and N_2 saturated environments were implemented by flowing high-purity O_2 and N_2 gas at 2 scfh into 80 ml of electrolyte for 30 min. All electrochemical data were expressed with respect to the reversible hydrogen electrode (RHE).

4.3 Results and Discussion

Three metal/N-doped hybrid catalysts (M-NC-Co, M-NC-Cu and M-NC-CoCu) are studied. In all three samples, metal clusters are well dispersed within a porous carbon matrix as shown in the SEM (Figure 4-1. a-c) and TEM images (Figure 4-1. d-f). The sizes of metal clusters in M-NC-Co and M-NC-Cu span up to hundreds of nanometers whereas those of M-NC-CoCu are significantly smaller with a more uniform distribution in size. This is in accordance with recent studies reporting the suppression of metal particle agglomerations by the introduction of a secondary metal in a MOF-based synthesis.[100,107] The SEM micrographs show that the carbon matrix of M-NC-CoCu is in a pinecone-like shape while the geometry of the other two samples are less defined. The HRTEM images of M-NC-CoCu show nanoparticles of metallic Co (Figure 4-1. g; *d*-spacing = 1.98 Å corresponding to Co (1 1 1) planes) encapsulated by graphitic carbon layers (Figure 1h; *d*-spacing of ~ 3.5 Å corresponding to C (0 0 2) plane).[108] The elemental maps of Co and Cu in M-NC-CoCu (Figure 4-1. m and n) reveal that Co species form nanoclusters while seemingly much smaller Cu are uniformly dispersed. Meanwhile, the O species (Figure 4-1. k) tend to reside where C species are located but a significantly lower O concentration is observed on Co nanoclusters, hinting most Co species are mostly in the metallic state. The N mapping (Figure 4-1. l) also suggests uniform and dense N-doping in the carbon matrix.

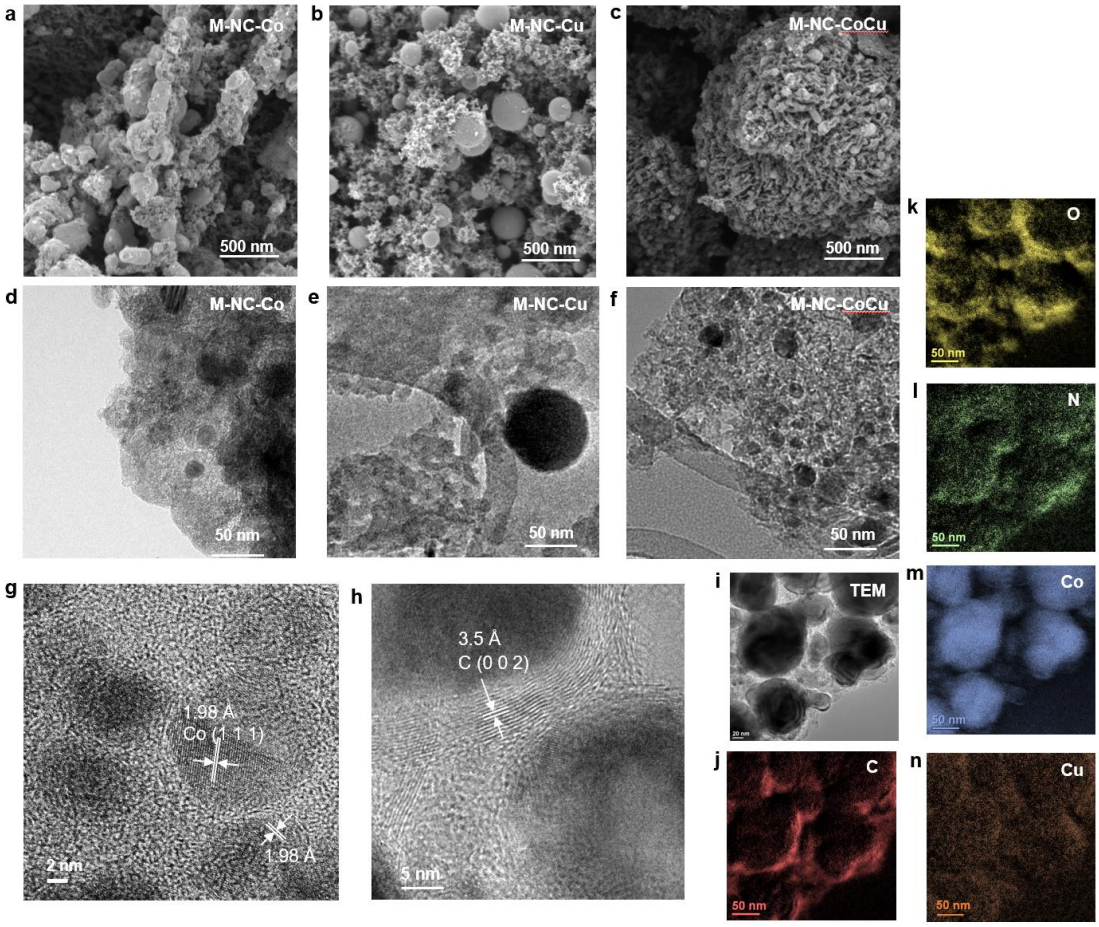

Figure 4-1 **.** SEM (a-c) and TEM (d-f) micrographs of M-NC-Co, M-NC-Cu and M-NC-CoCu. (g,h) HRTEM images of M-NC-CoCu showing lattice fringes of Co (1 1 1) and C (0 0 2). (i-n) A TEM image of M-NC-CoCu and its corresponding EFTEM elemental maps.

Fourier transform infrared spectroscopy (FT-IR) spectra (Figure 4-2. a) shows that M-NC-CoCu has a distinct presence of sp^2 C=N and C=C bonds,[109] unlike the other two hybrid catalysts. The larger amount of sp^2 bonds in M-NC-CoCu should provide a higher electronic conductivity through the carbon structure,[110,111] making it advantageous for electrode performance. The peaks located at 2000 – 2300 cm^{-1} are ascribed to ambient CO_2. The XRD spectra (Figure 4-2. b) shows a dominant presence of cubic Co in M-NC-Co and cubic Cu in M-NC-Cu. The average sizes of Co in M-NC-Co and Cu in M-NC-

Cu quantified by applying the Scherrer equation[112] to their (1 1 1) peaks are 44.3 and 73.8 nm, respectively. Interestingly, the spectrum for M-NC-CoCu has peaks mostly corresponding to cubic Co without a trace of monometallic Cu. The average size of Co in M-NC-CoCu (27.7 nm) is much smaller than that of M-NC-Co, which is in accordance with the SEM images in Figure 1. Most of the other tiny peaks found in M-NC-CoCu (Figure 4-2. c) are attributed to spinel $CuCo_2O_4$ (Fm-3m:2 space group).[65,67,113] The average size of $CuCo_2O_4$ crystals quantified by applying the Scherrer equation to the (3 1 1) peak is 4.3 nm, which is significantly

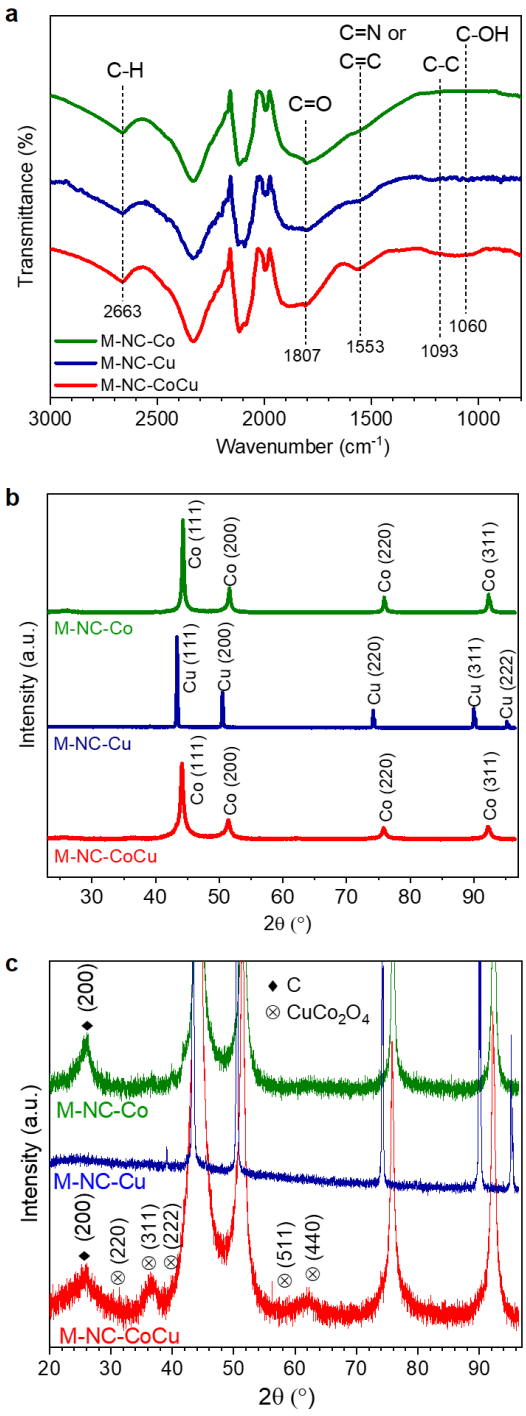

Figure 4-2. (a) FT-IR spectra and (b,c) XRD spectra of the three samples. (c) shows zoomed-in spectra of (b) for clarity.

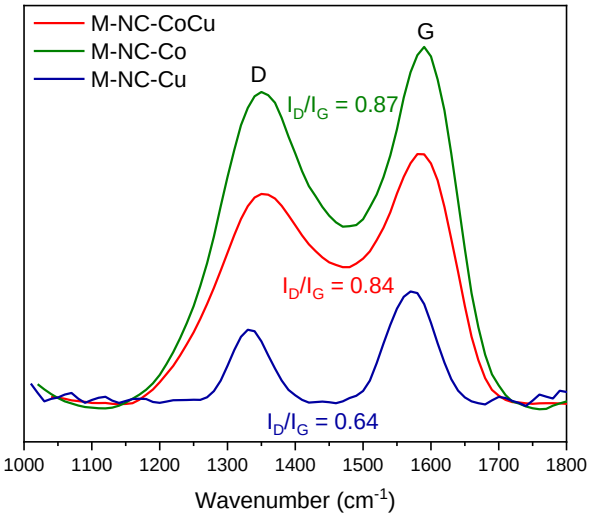

Figure 4-3. Raman spectra of M-NC-Co, M-NC-Cu and M-NC-CoCu

smaller than Co (33.7 nm) found in the same sample. It is also noted that the small graphitic peak at 2θ = 25.6° corresponding to (0 0 2) carbon plane is visible in M-NC-Co and M-NC-CoCu (Figure 4-2. c), which is also aligned with the aforementioned HRTEM observation (Figure 4-1. h). The average thicknesses of the graphitic layers estimated again by the Scherrer equation are 3.52 nm for M-NC-Co and 1.80 nm for M-NC-CoCu. An encapsulation of Cu by graphitic carbon is known to be difficult to achieve via an *in situ* carbonization of MOFs due to the fast nucleation of Cu,[114] explaining the absence of the graphitic diffraction peak (Figure 4-2c) and the large Cu particle sizes in M-NC-Cu (Figure 4-1. b).

Raman spectra of M-NC-Co, M-NC-Cu and M-NC-CoCu in Figure 4-3 shows that all samples had graphitic sp^2 carbon. M-NC-Co has the highest I_D/I_G ratio. This correlates with results quantified relative atomic percentage of the XPS C1s, which also showed that M-NC-Co with the highest relative graphitic carbon in Figure 4-5.

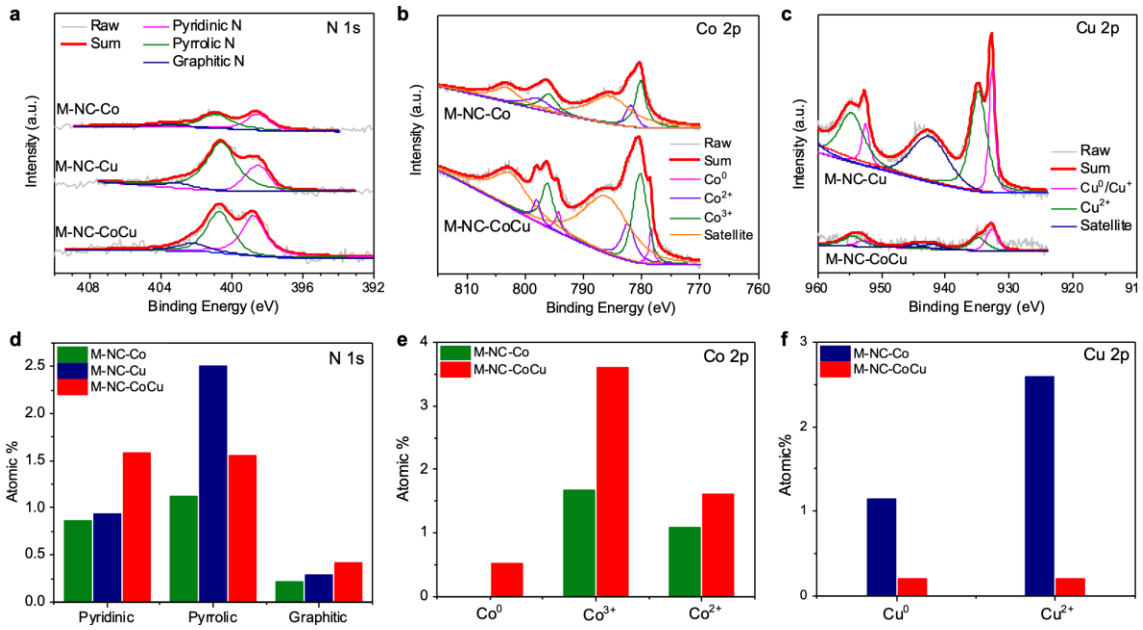

Figure 4-4. (a-c) XPS spectra of N 1s (a), Co 2p (b) and Cu 2p (c) and (d-f) the atomic percentages of species quantified based upon the XPS spectra.

X-ray photoelectron spectra (XPS) analysis was conducted for a better understanding of the chemical bonding in these samples. In the survey spectra for the three hybrid samples, Co, Cu, O, N, and C were detected (Figure 4-5. a). The N 1s spectra shows peaks for graphitic (402.2 eV), pyrrolic (400.7 eV) and pyridinic (398.7 eV) nitrogen for all three samples (Figure 4-4. a),[67,115,116] confirming a considerable amount of N-doping in the supporting carbon structures. The M-NC-Cu and M-NC-CoCu samples are quantified to have higher N contents (Figure 4-4. d; 3.7 and 3.6 at%) than M-NC-Co (2.8 at%). This is ascribed to the presence of Cu, which readily complexes with N and retains N even after thermal treatments,[67] forming more catalytically active Cu-N_x moieties.[117,118] It is also noted that M-NC-CoCu has the highest amount of pyridinic and graphitic N (Figure 4-4d), both of which are known to contribute to ORR and HER activity.[48,67,101,119–122]

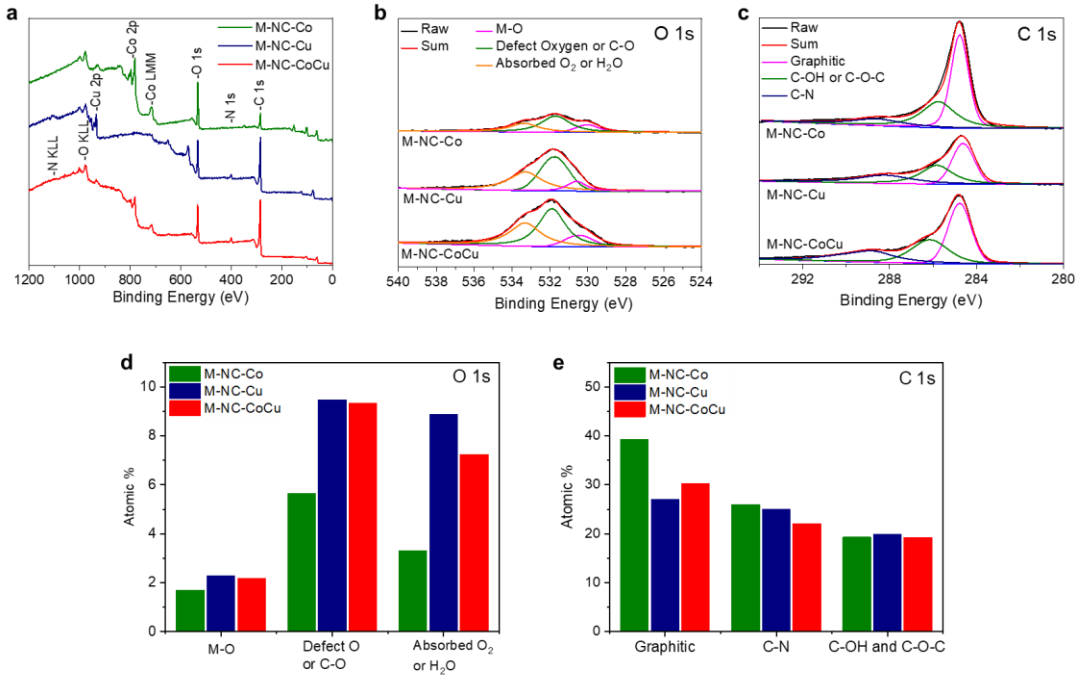

Figure 4-5. (a-c) XPS spectra. (a) Wide-range survey scan, (b) O 1s, (c) C 1s. (d-e) Atomic percentages of species deduced from the XPS spectra shown in (b) and (c).

We also note that the M-NC-CoCu has a distinct metallic Co peak (778.4 eV) unlike M-NC-Co (Figure 4-4. b). While M-NC-Co showed a strong presence of metallic Co phase in XRD (Figure 4-2b), no metallic Co peak is detected by XPS, indicating Co was oxidized on its surface. In contrast, the metallic Co peak detected from M-NC-CoCu is possibly due to the graphitic layer that encased the Co nanoparticles as seen in Figure 1h, which protects the Co from oxidation, leading to the enhancement in catalytic performance and stability.[17,67,123]

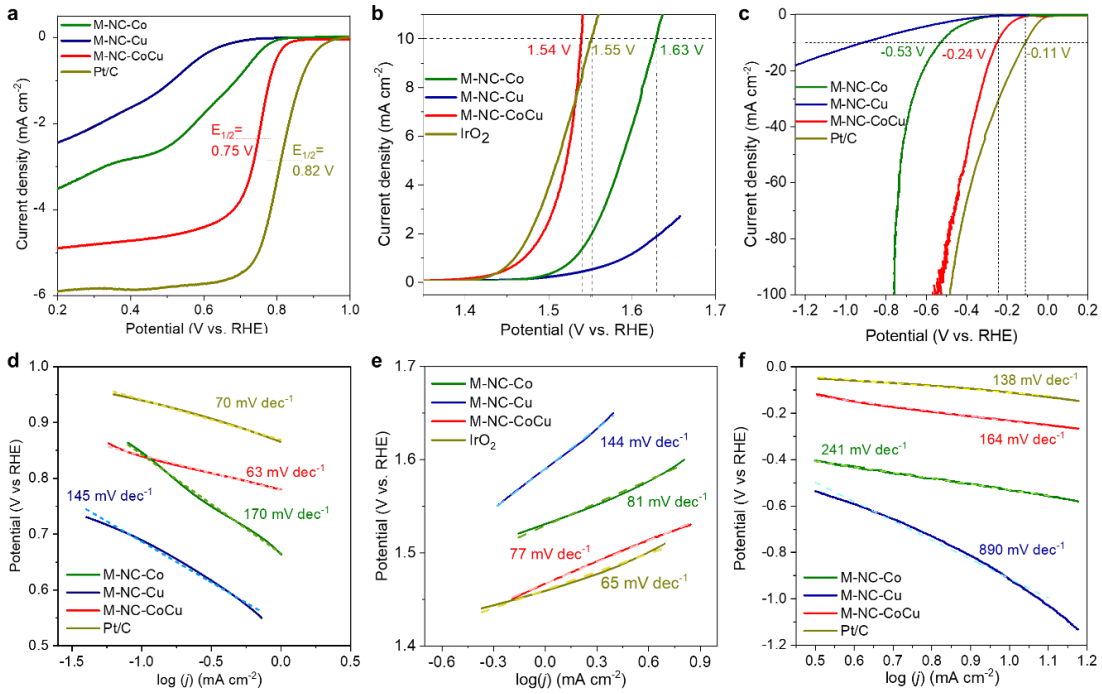

Figure 4-6. (a-c) LSV voltammograms for ORR (a), OER (b) and HER (c). (d-f) Tafel plots along with Tafel slope values for ORR (d), OER (e) and HER (f). All quantified at 1600 rpm. ORR voltammograms are obtained in 0.1 M KOH while OER and HER voltammograms are obtained in 1 M KOH.

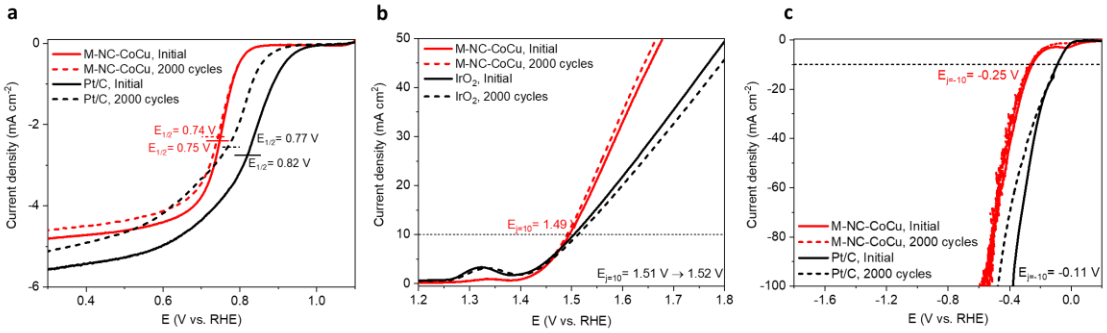

Figure 4-7. Cyclic durability LSV of M-N-CoCu and noble metal benchmarks for ORR (a), OER (b) and HER (c). The potential range of cycling is 0.2 – 1.2 V for ORR, 1 – 2 V for OER and -0.1 – 0.3 V for HER. Quantified at 1600 rpm in 0.1 M KOH for ORR, in 1 M KOH for HER, and in a stationary condition on a Ni foam in 1 M KOH for OER. Note

that the OER voltammograms presented in Figure 4 were obtained on a RDE setup at 1600 rpm, not on a Ni foam.

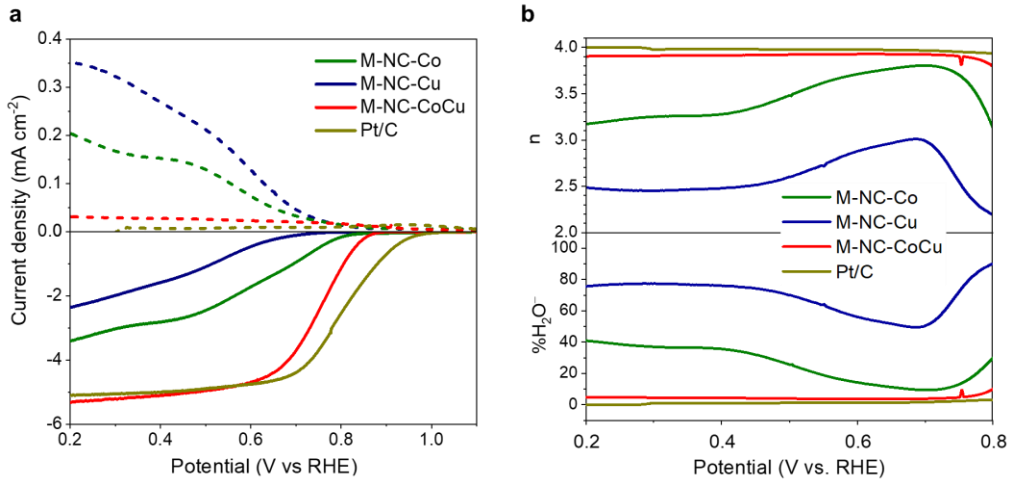

Figure 4-8. Electrochemical voltammograms for (a-d) ORR and. (a) LSV voltammograms, (b) Tafel plots along with Tafel slope values, (c) RRDE voltammograms for ORR and (d) the resulting peroxide percentage (lower) and electron transfer number (upper). All quantified at 1600 rpm in 0.1 M KOH.

Two oxidized Co species, Co^{3+} (780.2 eV) and Co^{2+} (781.9 eV) are present with a Co^{3+}/Co^{2+} ratio of 1.52 and 2.22 for M-NC-Co and M-NC-CoCu, respectively (Figure 4-4. e). The higher Co^{3+}/Co^{2+} ratio of M-NC-CoCu supports the presence of spinel $CuCo_2O_4$ in the sample; in the spinel structure, Cu occupies tetrahedral sites making Co species sit in octahedral sites with high valence state.[65] Furthermore, spinel $CuCo_2O_4$ is considered to be highly active toward ORR and OER,[65,103,124,125] which is well aligned with the excellent catalytic performance of M-NC-CoCu discussed below. In the N 1s spectra, the pyridinic N peak (398.6 eV) can also be ascribed to the catalytically active Co-N and/or Cu-N bonds due to their similar binding energies.[116,126] The Cu 2p spectra of M-NC-Cu and M-NC-CoCu have two main peaks, one associated with metallic Cu or Cu^+ species (932.7 eV) and the other corresponding to Cu^{2+} (934.8 eV). Both Cu^+ and Cu^{2+} are assigned to unsaturated Cu–N centers,[67,114,127,128] while Cu^{2+} is additionally

assigned to Cu–O in the spinel structure and Cu-O_x.[65] The aforementioned Cu elemental map (Figure 4-1. m) showed that Cu species are uniformly dispersed on both Co nanoclusters and carbon matrix. Those dispersed on Co clusters is ascribed to small crystalline domains of $CuCo_2O_4$, and those located on the carbon matrix are presumed to form Cu-N-C and Cu-O-C, as opposed to crystalline clusters of monometallic cubic Cu. The N 1s spectra also suggests the presence of Cu-N_x, which has been assigned for ~398.5 eV.[58,99,128]

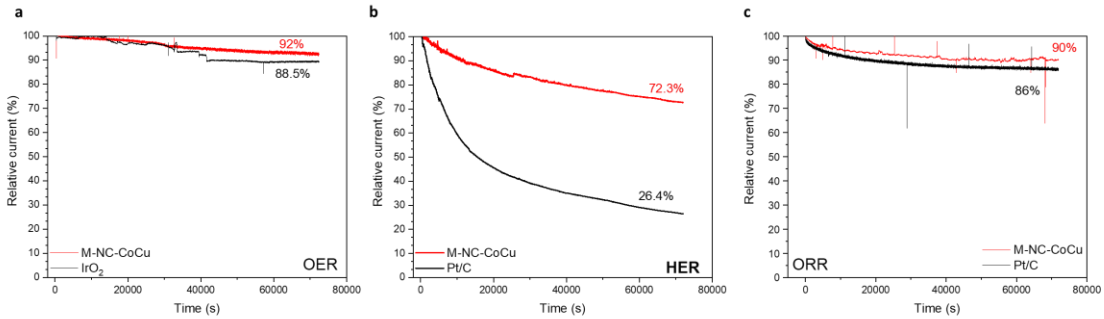

Figure 4-9. (a-c) chronoamperometric stability evaluation for OER, HER and ORR of M-NC-CoCu and benchmarks. (a) OER in1 M KOH at 1.55 vs. RHE, (b) HER in 1 M KOH -0.3 V in 1 M KOH vs RHE and (c) ORR in 0.1 M KOH at 0.5 vs. RHE.

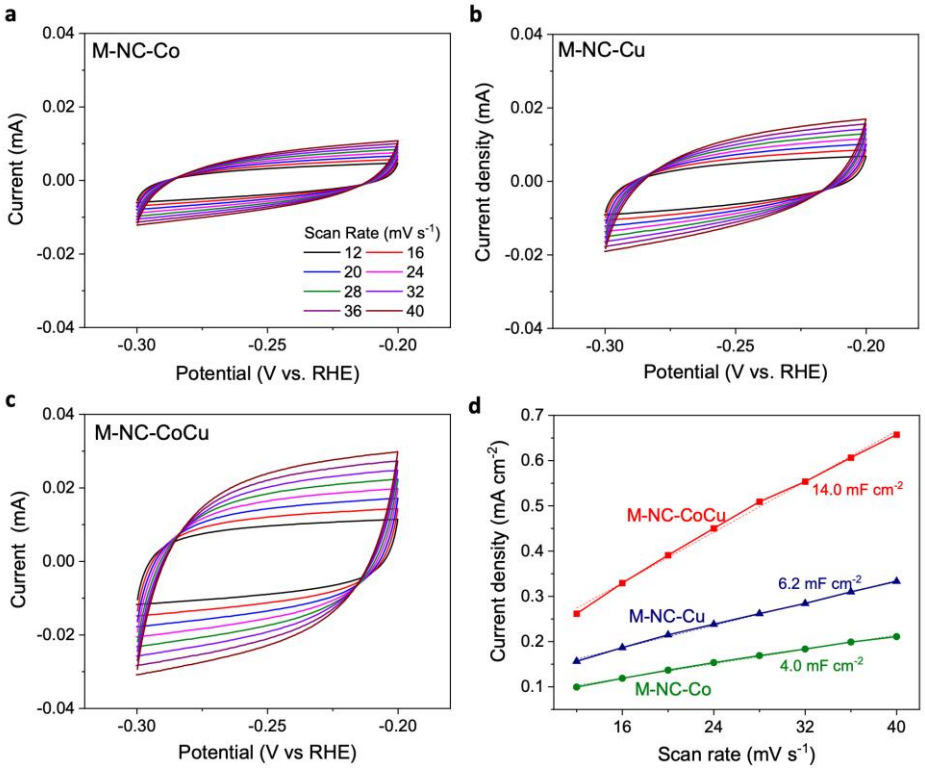

Figure 4-10. CV measurements for M-NC-Co (a), M-NC-Cu (b), M-NC-CoCu (c) under N_2 saturation in 0.1 M KOH and (d) their corresponding ECSA quantification.

The oxygen electrocatalytic performance of the three hybrid samples is compared with noble metal-based benchmark catalysts: Pt/C for ORR and HER, and IrO_2 for OER. The ORR voltammograms in 0.1 M KOH (Figure 4-6. a) shows that M-NC-CoCu performs the best among the three hybrids with onset potential (E_{on}) and half-wave potential ($E_{1/2}$) of 0.85 V and 0.75 V (versus RHE hereafter), comparable to those of Pt/C (E_{on} = 0.93 V; $E_{1/2}$ = 0.82 V). M-NC-CoCu also affords a small Tafel slope (63 mV dec^{-1}; Figure 4-6. b), even lower than Pt/C (70 mV dec^{-1}) indicating its fast ORR kinetics. In addition, M-NC-CoCu exhibits a dominant four electron process with the electron transfer number (n) of 3.9 – 4.0 in the wide potential window of 0.2 – 0.8 V (Figure 4-8), unlike the other two hybrids rendering a mixed $2e^-$ and $4e^-$ transfer (n = 2.48 and 3.28 for M-NC-Cu and M-NC-Co at 0.4 V). As for OER, M-NC-CoCu still exhibits the best performance among the hybrid catalysts, reaching 10 mA cm^{-2} in 1 M KOH at the lowest

potential of 1.54 V ($E_{j=10}$ = 1.54 V; Figure 4-6a), slightly smaller than the value for IrO_2 (1.55 V). Its Tafel slope is also the smallest (77 mV dec^{-1}; Figure 4-6. b) among the three hybrids, close to that of IrO_2 (65 mV dec^{-1}). Furthermore, M-NC-CoCu shows the lowest HER overpotential among the hybrid samples with $E_{j=10}$ = -0.24 V to reach 10 mA cm^{-2} (Figure 4-6. c), the closest to that of Pt/C ($E_{j=10}$ = -0.11 V). Both M-NC-CoCu and Pt/C have the smallest Tafel slope (Figure 4-6. d) with 164 mV dec^{-1} and 138 mV dec^{-1}, respectively.

The reasons for the trifunctional capability of M-NC-CoCu can be summarized as follows. First, M-NC-CoCu has $CuCo_2O_4$ phases, which has been reported to be active toward both OER and ORR.[103,124,125] Additionally, the highly dispersed Cu-N_x and Cu-O_x moieties and the largest amount of graphitic and pyridinic N-doping should further contribute to the ORR, OER and HER activities. The unsaturated nature of Cu-N_x centers (with Cu^+ and Cu^{2+}) become active sites for ORR due to the unfilled 3d-orbital electrons that can contribute to the electronic interactions with oxygen intermediates, which results in an ideal chemisorption of oxygen.[117] The high concentrations of sp^2 bonding are also expected to enhance electronic conductivity of the matrix, and the well-defined 3D structure along with uniformly-dispersed catalytically-active species should also be synergistically beneficial to the performance. A separately quantified electrochemically active surface area (ECSA; represented by double layer capacitance, C_{dl}) of M-NC-CoCu is indeed found to be the highest by a significant margin among the hybrid catalysts. The C_{dl} values of M-NC-Co, M-NC-Cu and M-NC-CoCu are 4.0, 6.2 and 14.0 mF cm^{-2}, respectively (Figure 4-10). The high ECSA of M-NC-CoCu is consistent with its hierarchical morphology, smaller nanoparticles and highly dispersed Cu species.

Additionally, the durability of the best performing sample (M-NC-CoCu) is characterized by cyclic measurements in the potential window of 0.2 V – 1.2 V for ORR (in 0.1 M KOH), 1.0 V – 2.0 V for OER (in 1 M KOH) and -0.3 V - 0.3 V for HER (in 1 M KOH), and compared to those of noble metal benchmarks. For ORR, M-NC-CoCu shows a slight change in $E_{1/2}$ (from 0.75 V to 0.74 V) after 2,000 cycles whereas Pt/C showed a significant degradation by decreasing $E_{1/2}$ from 0.82 V to 0.77 V (Figure 4-7.

a). For both OER and HER, M-NC-CoCu shows impressive cycling durability; there is little change in the current-potential profile up to 50 mA cm^{-2} after 2,000 cycles (Figure 4-7. b). On the other hand, IrO_2 for OER shows a noticeable degradation by increasing $E_{j=10}$ from 1.51 V to 1.52 V. The degradation is more pronounced at higher current densities; the potential to reach j = 40 mA cm^{-2} increased from 1.73 V to 1.76 V. It is noted that the discrepancy between OER voltammograms shown in Figure 4-6. a and Figure 4-7. b is originated from the different setup they are obtained; the cycle durability test for OER was performed by placing the samples on a Ni foam whereas all the electrochemical measurements including ORR durability test was performed on a rotating glassy carbon. Oxygen gas bubbling from a continuous OER prevented stable voltammetry in the rotating glassy carbon setup.

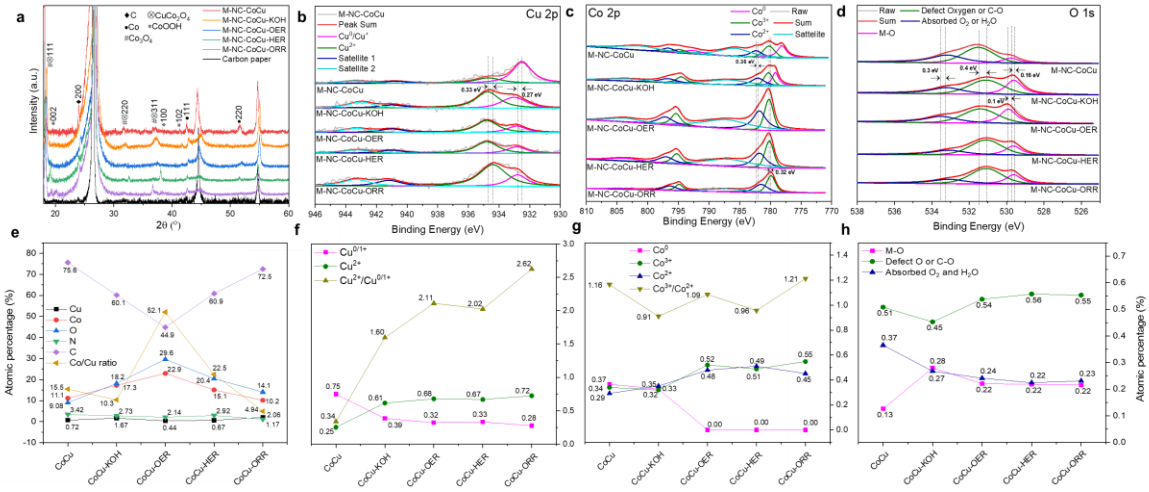

Figure 4-11. (a) XRD and (b-d) XPS spectra of samples after electrochemical durability cycling. (b) Cu 2p, (c) Co 2p, (d) N1s. (e-f) Relative atomic percentage (%) of species deduced from (a) wide scan spectra of the samples and the XPS spectra shown in (b-d).

For M-NC-CoCu-KOH there is a decrease in intensity and positive shift to higher binding energy (BE) in both metallic Co^0 (~778 eV in Figure 4-11. c) and $Cu^{0/1+}$ (~933 eV in Figure 4-11. b), which is likely due to the leaching of the metallic species and their oxidation after being submerged in KOH for 12 hours.[19,129] Even though the amount of metallic Co is lower in M-NC-CoCu-KOH, it is still present when comparing to the post

durability samples. This could be associated with the nanoparticles being encased in graphitic carbon (Figure 4-1. h). [17,67,123] The oxidation of these species is further corroborated by the O1s (Figure 4-11. d) and N1s (Figure 4-12. a), which reveal an increase metal oxide species (M-O), absorbed oxygen/water species and increase in pyridinic N (Figure 4-12. c). Nonetheless, still intact in XRD are the peaks corresponding to spinel $CuCo_2O$ (COD no. 1537073) and potentially crystalline CoO_x catalytic active site pertaining to Co_3O_4 (COD no. 1528447) at around 18.9° and 36.3° and CoOOH (COD no. 9009449) 20.15° and 41.8°, which shows that all the peak locations of M-NC-CoCu-KOH are similar with M-NC-CoCu.

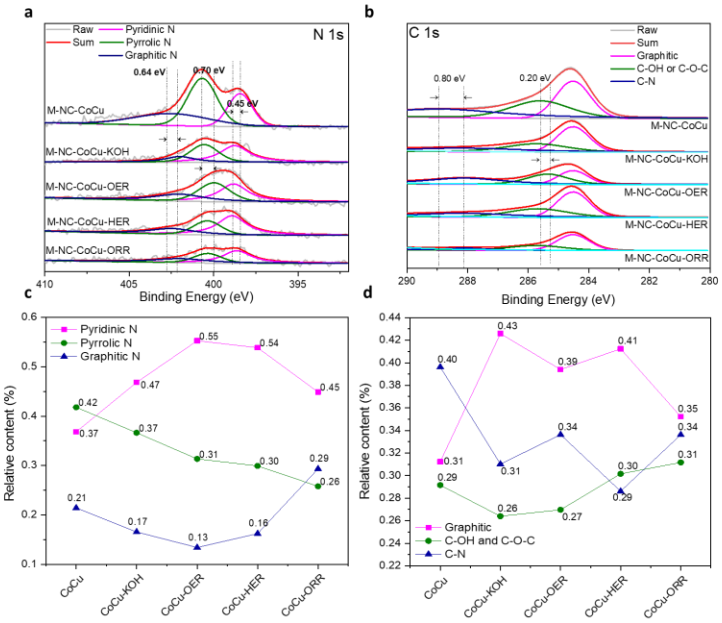

Figure 4-12. (a and c) XPS spectra of samples after electrochemical durability cycling. (a) O 1s, (c) C 1s. (b and d) Relative atomic percentage (%) of species deduced from the XPS spectra shown in (a) and (c).

Similarly, post OER sample M-NC-CoCu had similar XRD spectra with not much change. However, in terms of XPS, M-NC-CoCu-OER had complete absence of Co^0 peak this is due to oxidation and leaching of metallic Co in alkaline environment and

oxidative potential. From the Co $2p_{3/2}$ spectra M-NC-CoCu-OER (Figure 4-11. c) the peaks at 780.22 eV and 781.83 eV corresponding to Co^{3+} and Co^{2+} are in the line with the M-NC-CoCu sample. This indicates that Co^{3+} could be found in octahedral sites and Co^{2+} of tetrahedral sites for potential OER catalytic sites like $CuCo_2O_4$ and crystalline CoO_x structures, which also include Co_3O_4.[130–132] However, looking at the relative atomic percentages (Figure 4-11. h), the Co^{3+}/Co^{2+} ratio decreased post OER (1.33 to 0.7750), which is not common for the formation of CoOOH during OER resulting in the oxidation of Co^{2+} to Co^{3+}.[130,133] Still, an increase in Co^{2+} could signify an increase in oxygen vacancies in CoOx and CuCoOx, and when comparing to M-NC-CoCu-KOH there is an increase in Co3+/Co2+ ratio (0.911 to 1.09), which might indicate the oxidation of Co during OER could of happened after the sample had been etched by the KOH electrolyte.[54,134] The increase in oxygen vacancies is supplemented by O1s spectra (Figure 4-11. d) increase in the peak associated with defect oxygen (0.508 to 0.538) and M-O peak (0.126 to 0.221). In addition, the higher Co^{2+} content (Figure 4-11. c) could also pertain to Co-N_x, which happens to have a negative shift that is complimented by a positive shift and increase (0.368 to 0.553) in pyridinic peak in N 1s for post OER (Figure 4-12. a) signifying potential electron donating from N to Co.[135] Looking at Cu $2p_{3/2}$ (Figure 4-11. b) the for M-NC-CoCu-OER shows BE corresponding to $CuCo_2O_4$ with Cu^+ at 932.7 eV and Cu^{2+} at 934.7 eV, that could correspond to Cu oxidations states in $CuCo_2O_4$. The slightly higher biding energy of peak corresponding to Cu^+ might also signify the oxidation of metallic Cu.[136]

For M-NC-CoCu-HER, its XRD spectra is similar to M-NC-CoCu-KOH and M-NC-CoCu-OER only differing by a more well-defined peak at around 37.7° pertaining CoOOH. Like KOH and OER samples, M-NC-CoCu-HER also had the Co $2p_{3/2}$ peaks (Figure 4-12c) corresponding to Co^0 completely diminished. Therefore, the well defined CoOOH XRD peak could pertain to the oxidization of Co found in $CuCo_2O_4$, which is similar to M-NC-CoCu-OER, or also to oxidization of Co in CoN_x due the adsorption of water during HER in alkaline environment resulting in OH-Co-N moiety.[137] In general, the peak of Cu $2p_{3/2}$ centered at around 932.7 eV for Cu^+ could be connect with Cu^+ in Cu_3N, and its positive shift post HER can signify the possible oxidation in alkaline

environment. This falls in line with N 1s (Figure 4-12. a) graphitic N and O 1s (Figure 4-12. b) C-N peak, which have a negative shift supporting the electron coupling of Cu complexed in N-doped carbon support for HER electrocatalysis. [136]

After ORR cycling, there is a well-defined narrow XRD peak around corresponding spinel Co and CuCoCO. Looking at Co $2p_{3/2}$ (Figure 4-11. c) we see that there is a negative shifts for Co^{3+} to 779.88 eV and Co^{2+} to 781.36 eV. These lower BE shifts could be associated with a change in the cation distribution at the spinel surface when Co^{2+} (occupying the tetrahedral site) is replaced by Cu^{2+} ions in the spinel structure.[138] Therefore, this XRD peak would most likely be attributed to $CuCo_2O_4$. The peak location of Cu^{2+} (Figure 4-11. b), which was around 934.4 eV, has slightly lower BE than M-NC-CoCu, which might indicate a interaction between Co-Cu and an increase of electron-density for Cu^{2+}.[102] Though, Cu^{2+} is also linked with CuN_x, and is a known catalytic site for ORR, so the lower BE could also be due to its activity as a redox center for ORR. Meanwhile, the Cu $2p_{3/2}$ peak associated with Cu^0 and Cu^+ has a positive BE shift, which could signify the oxidation metallic Cu^0 to Cu^+. However, this could also signify the participation of Cu^+ as an unsaturated in CuN_x serving as an active center for ORR, which resulted in a positive BE shift due to Cu atoms transferring some valence electrons to nitrogen.[117] This is supported with negative shift in N 1s graphitic N (Figure 4-12. a) and C 1s C-N (Figure 4-12. b). Furthermore, it is suspected that during ORR the presence of adsorbed oxygen on the basal plane of quaternary site causes is positive shift in the BE of the pyridinic peak (Figure 4-12. a), resulting in pyridinic oxide ($N\text{-}O^+$).[139]

4.4 Conclusions

In this chapter, we demonstrated a facile synthesis of an efficient trifunctional electrocatalyst where Co/Cu species are incorporated in a high-surface-area N-doped carbon structure. The facile synthesis approach of MOF formation followed by a pyrolysis process formed highly-dispersed catalytically-active sites in a hierarchical N-doped carbon. The presence of both Cu and Co species is conjectured to have deterred the agglomeration of each other and form well-dispersed active sites such as $Cu\text{-}N_x$, $Cu\text{-}O_x$

and $CuCo_2O_4$. The excellent electrocatalytic performance of M-NC-CoCu can be ascribed to multiple factors: (1) the high-surface-area structure of carbon matrix, (2) uniformly distributed tiny-sized catalytically active sites such as $CuCo_2O_4$ phases as well as Cu-O_x, Cu-N_x and Co-N_x moieties, (3) high concentration of graphitic and pyridinic nitrogen, and (4) high concentration of sp^2 bonding beneficial for electronic conduction. The multitude of active sites derived from bimetallic Cu and Co species and N-doped carbon support of M-NC-CoCu prove to be effective in catalyzing ORR, OER and HER. This study suggests that a bimetallic mixture and doping can result in multiple favorable effects that can be highly leveraged for efficient trifunctional electrocatalyst.

Limitations: Although, the heterogeneity of this material demonstrated beneficial for achieving tri-functionality, it is still difficult to pin-point exact the catalytic active sites because there were so many possibilities. This in turn will make it difficult to try to further improve the catalytic activity of this material because there are so many possible sites. In addition, because this material has trifunctional electrocatalytic activity, it is not the best catalyst for all three reactions. It seems that it is a comparable OER catalyst in comparison to other catalyst found in literature but is still lacking in both ORR and HER. HER, had very poor stability as seen in Figure 4-9.

5. TiO_2 FUNCTIONALIZATION ON GRAPHENE OXIDE BY ATOMIC LAYER DEPOSITION

5.1 Introduction

Titanium dioxide (TiO_2) is an abundant, inexpensive and non-toxic material that has been widely used for a variety of applications ranging from sunscreens, solar cells, optics to photocatalyzers.[140] TiO_2 versatility is due to the capability to tune its chemical and physical properties[20] and its electrocatalytic performance.[141] The catalytic activity of TiO_2 can also be significantly enhanced by incorporating them onto an electron-conducting scaffold made of nanostructured carbon such as reduced graphene oxide (rGO).

Graphene oxide (GO) can be chemically reduced to graphene-like materials with excellent mechanical and chemical properties, and work as a useful precursor for the synthesis of functionalized graphene, which potentially renders a unique mechanical, electrochemical and electronic properties.[142] Since GO itself has very low electron conductivity, it needs to be reduced for use as an electrode material. As an approach of reducing GO, TiO_2 can be used; from UV-irradiated TiO_2 suspensions, GO accepts electrons and thus becomes reduced.[143] The TiO_2 tethered on the GO is also found to prevent restacking of graphene sheets, which is advantageous to use the resulting hybrid as a catalyst. The rGO incorporated with TiO_2 is a commonly used material as photocatalyzers,[144] but it was rarely considered for ORR catalysis.

Recent studies have shown that the TiO_2 can have catalytic activity towards ORR. It was observed that ordered phases of TiO_2 crystals can facilitate electron transport, which enhances its catalytic activity towards the reduction of oxygen.[145] TiO_2 is a polymorphous structure that has three common phases: anatase, rutile and brookite.[21] This study not only showed anatase as the optimal phase for ORR catalysis, but also showed that the oxygen vacancies in sub-stoichiometric TiO_{2-x} provides favorable site for oxygen binding, and thus facilitating its reduction. Forming oxygen vacancies, or

reducing TiO_2, can be done in several ways such as doping,[146] photo induced reduction,[147] thermal reduction and hydrogen reduction. We aimed to achieve this by the use of ALD.

ALD has recently gained popularity because of its precise deposition at the atomic level.[148] Unlike other physical and chemical deposition methods, ALD depends on self-limiting chemical reactions; only one layer can be adsorbed on the substrate for reaction per cycle. The titanium precursor used for ALD is expected to bind to oxygen functional groups such as hydroxyl (-OH) and carboxylic (-COOH) groups. GO is rich in these oxygen functional groups, making it an ideal substrate for ALD of TiO_2. By controlling the temperature of ALD chamber and precursor pulsing time, it is possible to control the resulting TiO_2 phase and deposition rate. The number of ALD cycle is varied to render different nominal thicknesses.

This study investigates the catalytic activities of titanium dioxide (TiO_2) incorporated GO, which was achieved by ALD. The catalytic activity was systematically evaluated by CV curves. It was found that TiO_2-anchored GO (by ALD) exhibits a catalytic activity significantly higher than rGO itself. The temperature for ALD process also was found to affect the catalytic activity of resulting TiO_2/rGO. This is ascribed to a combined contribution from facilitated reduction of GO and higher deposition rate of TiO_2 at higher temperatures. In addition, there is an optimal amount of TiO_x for catalytic activity, which is achieved by 25 cycles of ALD. The deposition of TiO_x onto GO by ALD is not new, but to our knowledge this is the first study to take this approach for ORR catalysis.

5.2 Experimental

5.2.1 TiO_x on GO by ALD synthesis

GO was synthesized using graphite by a modified and improved version of Hummer's method using graphite powder (<20 um, Sigma-Aldrich), $KMnO_4$ (ACS reagent, ≥99.0%), and an acid mixture of 9:1 of H_2SO_4 (ACS, 95 – 98 %, Alfa Aesar)/H_3PO_4 (ACS reagent, ≥ 85wt% in H_2O, Alfa Aesar).[149] The reaction was then

heated to 50°C. The GO solution was then brought to a pH > 5 by several water rinses followed by centrifuge, and vacuum filtrated to a solid. The GO was then dispersed in 1:9 water to dimethylformamide (DMF) to make a 2 M solution.

The GO solution was then drop-casted on the surface of stainless steel (SS; 99.99% purity, Goodfellow). The SS was prepared and cleaned using a three-step solvent rinse with isopropanol, ethanol, and water. The SS was submerged in each solvent is sonicated for 20 min and finalized with ozone cleaning. The drop casting process consisted of covering the surface SS with 10 ml of the GO colloidal solution followed by an air-drying at room temperature. This drop casting-and-drying process was repeated eight times to prepare a GO/SS scaffold for TiO_2 ALD onto it.

Before inserting the GO/SS sample into the ALD chamber (Savanah 100, Cambridge NanoTech), the chamber was heated up to the desired temperature. The deposition was performed at three different temperatures (150, 200 and 250°C) with different number of ALD cycles (10 – 125). The pulsing time for titanium precursor, Tetrakis (dimethylamido) titanium (99.99%-Ti Puratrem, STREM), was maintained at 0.5 s and the water (as oxygen source) was maintained at 0.1 s. The deposition was performed under vacuum conditions (0.2 torr) with 20 sccm N_2 flow. It is estimated that 25 cycles lead to a TiO_x deposition with a nominal thickness of ~1 nm.

5.2.2 Material Characterization

Scanning electron microscopy (SEM) was used to obtain the morphology of the sample using a Zeiss Gemini SEM 500 using a working current of 0.4 kV. The energy dispersive X-ray spectra (EDS) was captured using a FEI Qunata 200 ESEM equipped with EDAX Genesis software. FT-IR samples were dried under vacuum for 24 h by placing samples in a desiccator overnight and placed on a diamond crystal (Nicolet 380 system, Thermo Scientific).

5.2.3 Electrochemical Measurements

Cyclic voltammetry (CV) measurements were performed using a potentiostat (SP-200, Bio-Logic Science Instruments) with the catalyst (TiO_2 ALD'ed GO) in 0.1 M KOH electrolyte. Ag/AgCl (3.5 M KCl) was used as the reference electrode, and Pt wire was used as the counter electrode. The scan rate was 20 mV/sec, with a potential window of -0.3 to 0.7 V, under oxygen and nitrogen purged environments using a Biologic Potentiostat. All samples were tested after drop-casting a catalyst ink on a glassy carbon electrode. The ink was a mixture of the TiO_2/rGO catalyst and 5 wt% Nafion in a solvent made of 1:1 water and DMF. For Pt/C electrode was prepared using 20 wt5 Pt supported on carbon black (Vulcan XC72).

5.3 Results and Discussion

The SEM image in Figure 5-1 obtained at a low voltage using an in-lens detector reveals the morphology of GO sheets obtained from the modified Hummer's method. The GO structure is folded sheets that are wrinkled throughout the SS substrate.

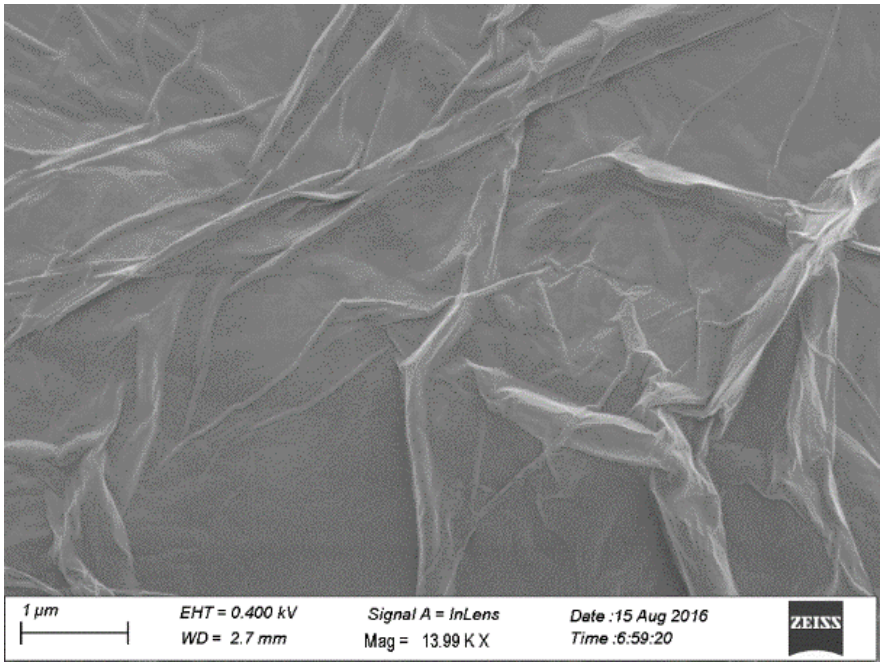

Figure 5-1. An SEM image of GO on the SS revealing a sheet-like morphology of GO.

The FTIR spectrum shown in Figure 5-2indicates the abundance of oxygen-containing functional groups on GO. These oxygen functional groups are conjectured to be responsible for binding the Ti precursor during ALD. The FTIR result shows distinct carbonyl peak, which can be responsible for carboxylic functional group at around 1625 cm^{-1}, and a distinct hydroxyl (-OH) peak at around 3400 cm^{-1}.

The synthesis of GO by a modified form of Hummer's method was proven to be successful based on the SEM (Figure 5-1) and FTIR results (Figure 5-2). The goal of using Hummer's method is to synthesize carbon structures rich in oxygen functional group that TiO_x can bind to during the ALD,[149] which was successfully achieved. GO, due to its high density of defects, is not a conductive material, but it was chosen for its simple processing, stable mechanical properties and the flexibility. More importantly, it has the flexibility of being readily functionalized and reduced. Even though GO itself has low conductivity, which is not ideal for catalytic material, the functionalization and reduction of GO can enhance its conductivity.[50,12]

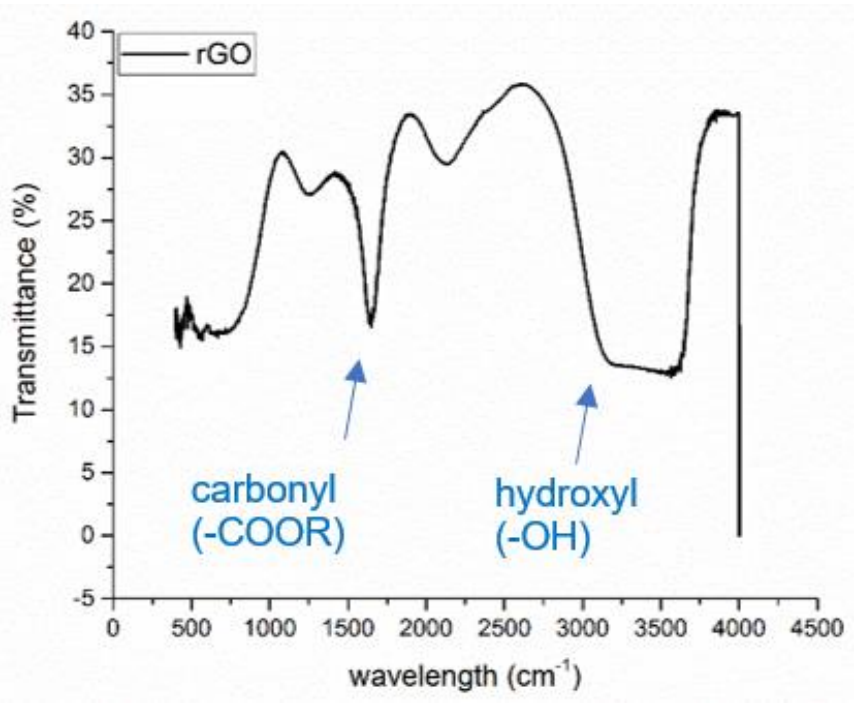

Figure 5-2. An FTIR spectrum showing oxygen functional groups on GO.

After TiO_2 was deposited by ALD onto the GO/SS, energy dispersive spectroscopy (EDS) was performed to examine the presence of titanium. The EDS spectra in Figure 5-3 shows two small peaks corresponding to titanium, confirming that Ti is indeed deposited by ALD on the surface of the GO. A distinct Fe peak in the spectra is ascribed to the SS substrate.

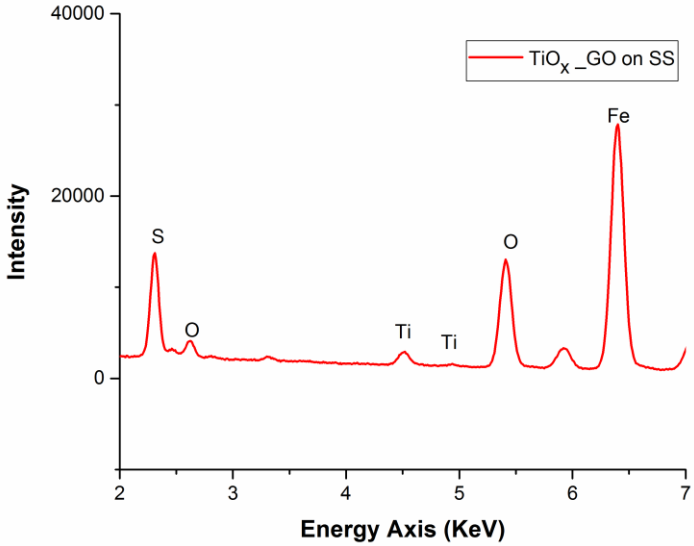

Figure 5-3. EDS map of the elemental composition found in the TiO_2/GO hybrid.

Transmission electron microscopy (TEM) was used to image the morphology of the GO and TiO_2 nanoparticles formed by the ALD. The sheet-like graphene structure was still conserved even after ALD was performed at elevated temperatures. However, embedded in the GO sheet-like structure there are nanoparticles that are several nanometers wide (Figure 5-5). With the use of energy filtered transmission electron microscopy (EFTEM), the nanoscale particles was found to correspond to TiO_2 (Figure 5-5d).

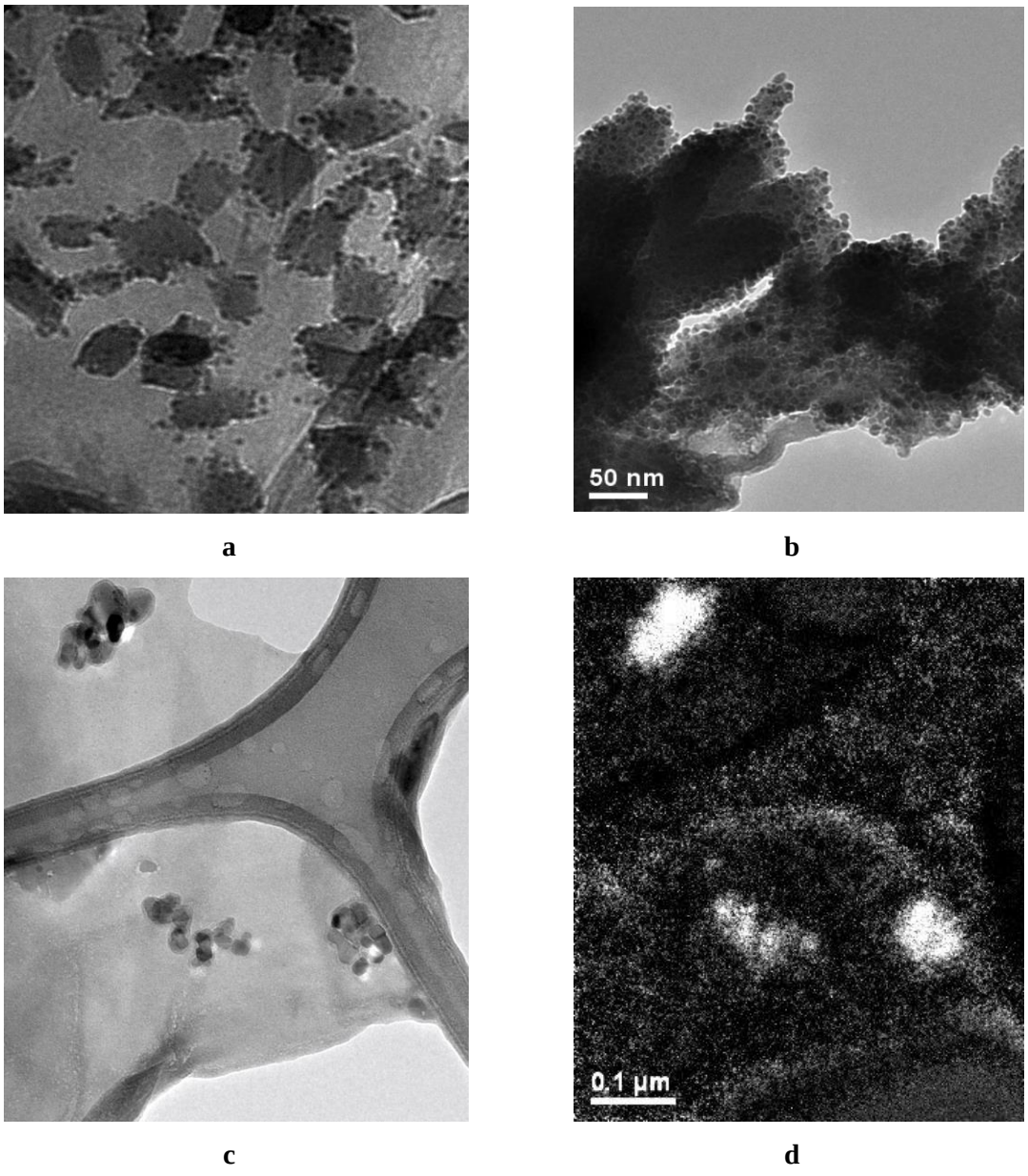

Figure 5-4. (a-c) TEM images of the TiO_2 incorporated GO by ALD. (d) An energy filtered TEM image that reveals the nanoparticles correspond to TiO_2.

When exposed to high temperatures during ALD, GO is likely to turn into reduced graphene oxide (rGO), which is more conductive.[150] In addition, TiO_2 binds to oxygen functional groups on GO, which is considered to be another contribution toward GO

reduction. On the other hand, by binding TiO_2 nanoparticles, GO nanosheets can be free of the issue of being agglomerated.[151] As an agglomeration can cause a decrease in the overall surface area and thus a sacrifice in the overall catalytic activity per gram, the suppression of agglomeration is highly advantageous for catalytic performance.

CV results in Figure 5-5 exhibits a comparison of electrochemical activity between TiO_2/rGO and GO. There is a significant different in the ORR performance between the two samples in terms of current density (0.1 mA/cm^2 for GO; ~ 0.5 mA/cm^2 for TiO_2/rGO) and on-set potential (-0.18 V vs Ag/AgCl for GO; -0.02 V for TiO_2/rGO), indicating that the ORR activity of GO was dramatically improved by TiO_2 ALD.

In addition, Figure 5-6 shows the effect that different number of ALD cycles has on the ORR activity. The CV was taken of GO samples deposited with 12 cycles, 25 cycles and 125 cycles. All samples were deposited at 250°C. In terms of the on-set potential and current, the sample deposited with 25 cycles has the best performance among the three samples. The TiO_2/rGO deposited with 25 cycles has a current density of ~ 1 mA/cm^2, and an on-set potential of ~ -0.056 V vs Ag/AgCl. The tetrakis (dimethylamido) titanium precursor at 250°C is expected to have a deposition rate of 0.04 nm/cycle. Therefore, an estimated thickness of ~ 1 nm coating was enough to form the nanometer-sized TiO_2 nanoparticles seen in the TEM images, which exhibited the best catalytic performance. The 125 cycles, corresponding to the TiO_2 thickness of 5 nm, would result in the formation of film, as opposed to dispersed nanoparticles. Film in comparison to nanoparticles have smaller surface area, which can reduce the number of exposed active sites. When compared to the benchmark Pt/C catalyst, the on-set potential was measured at ~ 0.015 V vs Ag/AgCl, slightly higher than that of the TiO_2/rGO catalyst.

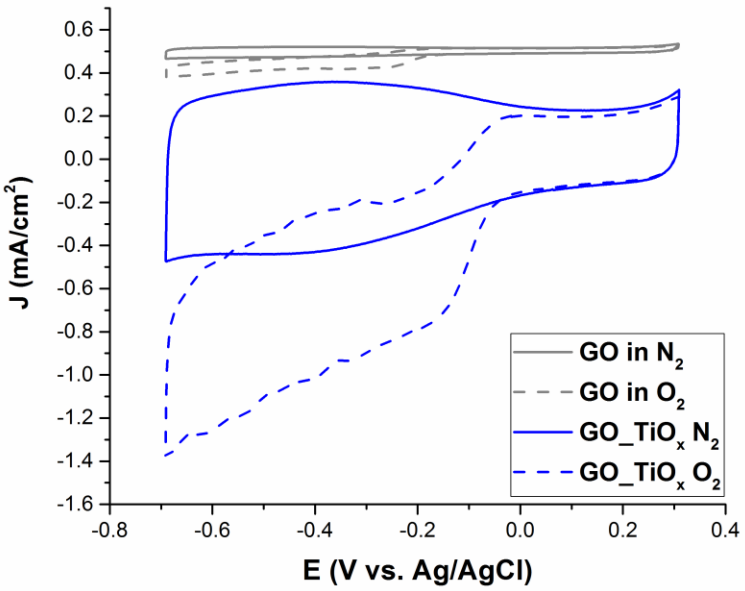

Figure 5-5. CV curves of GO and ALD TiO_2/GO in O_2 and N_2 saturated 0.1M KOH electrolyte.

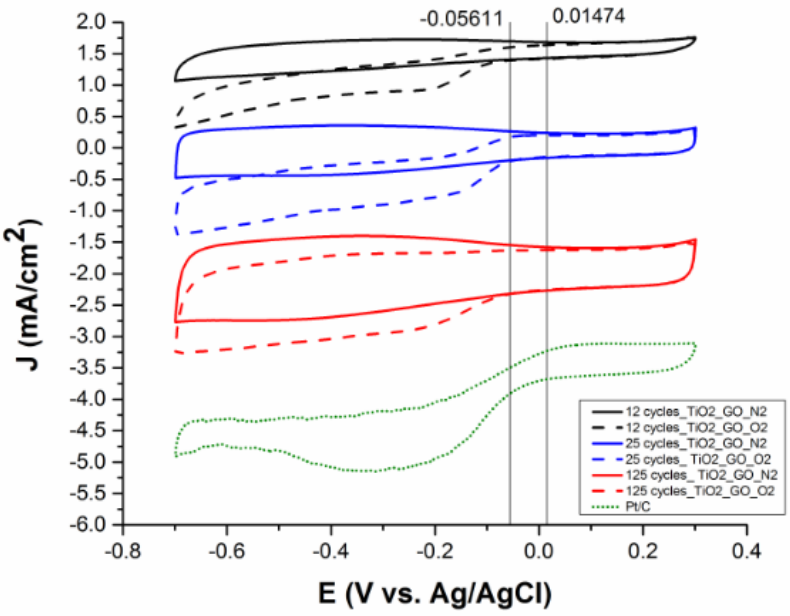

Figure 5-6. CV curves of TiO_2/GO deposited for different number of ALD cycles.

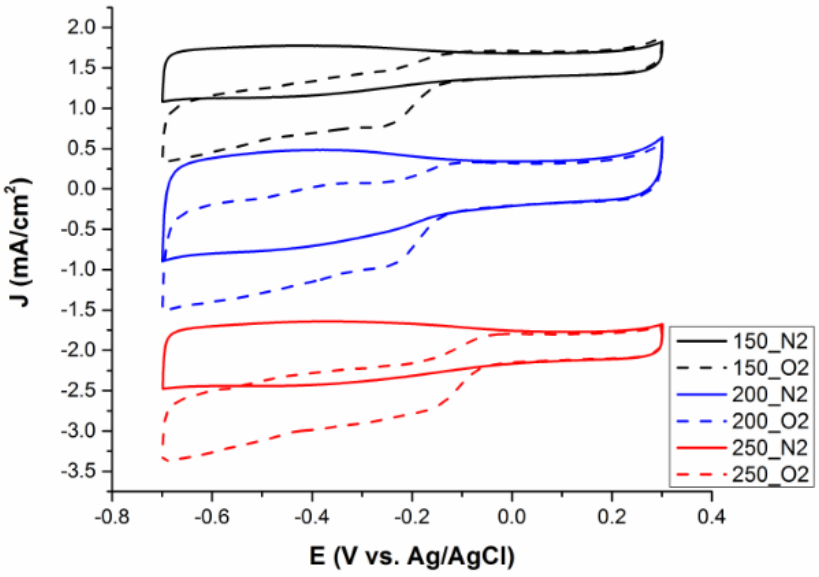

Figure 5-7. CV curves of TiO_2/GO deposited at different chamber temperatures (150, 200 and 250°C) by ALD.

The TiO_2/rGO samples were also deposited at three different chamber temperatures. The set of samples in Figure 5-7 were all deposited with a cycle number of 25. From the CV measurements, it is evident that the overall performance of TiO_2/rGO was improved by increasing the chamber temperature during ALD. Deposition at a higher temperature not only increases the reduction of GO, but it also has an important role in nucleation and crystal structure formation. Recall that catalytic activity of certain nanostructures has depended on the cationic oxidation state, crystal structure and crystal phase. This has especially been true for TiO_2, and the formation of non-stoichiometric form of TiO_2 has been shown to be better for its ORR catalytic activity by facilitating the absorption of O_2.[18]

5.4 Conclusion

This Chapter presents a study using CV for characterizing the catalytic activity of TiO_2/rGO. From TEM images, it was evident that TiO_2 nanoparticles (< 10 nm) were deposited by ALD. The CV results indicated a significant increase in catalytic activity after deposition of TiO_2 by ALD. The optimal ALD condition for ORR catalysis was found to be 25 cycles of deposition at 250 °C. An excessive number of cycles is conjectured to result in a relatively low-surface-area structure while a small cycle number cannot disperse sufficient TiO_2 nanoparticles for an optimum catalysis. Even with the same cycle number, the reaction temperature is also found to have a significant impact on the ORR activity of resulting TiO_2/GO hybrid. A higher temperature is advantageous in further reducing GO (and thus improving electronic conductivity of resulting rGO) and facilitating nucleating and crystalline growth of TiO_2 particles. Any impact on the stoichiometry of TiO_2 particles itself can be a possible factor, which is yet to be revealed.

Limitations: It is challenging to characterize the TiO_2/GO interfaces because of the small quantity of the titania that was deposited by ALD. In addition, the inconsistency in the chemical nature of GO, which as aforementioned is filled with different types of oxygen functional groups, made an explicit revelation of the active sites difficult.

6. ATOMICALLY DISPERSED TRANSITION METAL BY ATOMIC LAYER DEPOSITIN ON CARBONIZED ZIF-8

6.1 Introduction

Atomically dispersed metal sites (ADMS) have an important role in the development of electrocatalytic and photocatalytic devices. ADMS maximize atom-use efficiency and can provide unique coordination that is beneficial for catalyzing oxygen reactions that are crucial for energy conversion and renewable energy device efficiency.[152] In addition, decreasing metal size from bulk to nanoparticles, and then to the monoatomic level, can increase the specific activity per metal atom.[153] There are different synthesis methods for creating ADMS. One that has garnered considerable attention has been ADMS derived from metal-organic frameworks (MOFs).[52,53,154] The benefits of MOFs are that they can form highly ordered structures composed of organic linkers and metal nodes, and the well-defined porous arrangements, making them ideal substrates for supporting atomically dispersed metal sites (ADMS).[155] Usually, ADMS supported on MOFs can be achieved through controlled treatments, such as pyrolysis, nanoparticle transforming method and high-energy ball milling synthesis[97,156,157] These controlled treatments have been recently popular for designing catalytically active materials for electrode use in renewable energy devices.

However, there are some limitations to these methods of synthesizing MOF-derived ADMS including: agglomeration, drastic decrease of metal loading, and lower stability and/or bonding between support and metal complex.[38] Furthermore, the strengthening interfacial chemical bonding and finely dispersed anchor sites, have been the focus of many working on ADMS. [158]

One way of doing this is by introducing more than one metal center. The chemical bonds that are formed between metal atoms and supports can also enhance the stability of single metal atoms and anchoring of metals sites to prevent agglomeration.[52] Moreover, having more than one metal can exhibit binary metal composites and multi-valence species available to catalyze multiple reactions.[57,58] Therefore, creating transition bimetal

sites on carbon structures can increase the utilization and bifunctional catalytic activity of electrode material, overcoming the relatively low activity of single-TM catalysts.[35,63] A multi-metallic species often induces a synergetic effect resulting in a facile charge transfer between dissimilar metals and a decrease in the kinetic energy barrier from modulation of electronic structures.[63] For these reasons, bimetallic transition metals embedded N-doped carbon systems.

Furthermore, using an alternative synthesis method that can provide precise control and stability for ADMS is also highly sought out. Atomic layer deposition (ALD) has garnered a lot of interest recently due to its ability to provide controlled growth at the atomic level.[159–161] Even though ALD is mainly used for film making, controlling ALD parameters, such as temperature and cycle number, can allow the formation metal nanostructures. In addition, ALD is also useful in the exploration of structure-performance relationships in ADMS. For example, Sun et al. anchored isolated Pt atoms onto graphene nanosheets using an ALD technique with oxygen and (methylcyclo-pentadineyl)-trimethyl platinum as precursors. The researchers reported that through the use of ALD the Pt content of the catalyst can be varied from isolated single atoms to sub-nanometer sized.[162]

Still, the type of substrate used for ALD has a large influence on the formation kinetics of TM sites, their dispersion, and stabilization. Supports based on doped carbon can provide versatile binding sites to anchor potential catalytically active transition metal species. One of the most used functional groups in ALD is oxygen functional groups for attaching transition metals. These oxygen functional groups facilitate the removal of ligands for the deposition of metal.[163] Similarly, N-doped carbon materials have a variety of N functional groups, such as pyridinic N, pyrrolic N, graphitic N and quaternary N, which provide rich coordination sites for binding metal atoms.[158]

For this study, a zinc-based zeolitic imidazole framework (ZIF-8) is carbonized to form organized N-doped carbon nanostructures. The carbonized ZIF-8 (C-ZIF-8) was then used as a substrate (support) for ALD. Titanium (Ti) and cerium (Ce) precursors were deposited on C-ZIF-8 to create bimetal (Ti and Ce) and monometal (Ti or Ce)

electrocatalyst. We investigated the effects of bimetal incorporation to enhance the electrocatalytic properties of titanium and cerium supported on ZIF-8 derived carbon nanostructures. Preliminary data shows promising preliminary results towards oxygen evolution reaction (OER) and hydrogen evolution reaction (HER) after ALD.

6.2 Experimental

6.2.1 Synthesis of transition metal embedded C-Zif-8

The synthesis of Zif-8 was done using 0.05 mmol of zinc nitrate ($Zn(NO_3)_2$, 98%, Alfa Aesar) and 0.40 mmol 2-methylimidazole (99+% ACS grade, Alfa Aesar) were separately dissolved in 50 ml of methanol (99.8+% ACS grade, Alfa Aesar) and sonicated for 20 min. Then both solutions were transferred to a clean beaker and the final mixture was brought to 300 ml of methanol. The reaction took place at ambient temperature pressure for 1hr. The white solid was collected and rinsed several times via centrifugation using methanol and ethanol. After being air-dried, the sample was dried further at 150 ºC under N_2 conditions for 30 mins and prepped for a subsequent heat treatment. By heat-treating the resulting solid at 700 ºC for 2 h in N_2, a carbonized polyhedron Zif-8 structure denoted as C-Zif-8 was formed. Subsequently, atomic layer deposition (ALD) was then used to deposit titanium (Ti) and cerium (Ce) on the surface C-Zif-8. Titanium deposition was done under 250°C for 10 cycles with a deposition of 0.4 Å/ cycle using Tetrakis (dimethylamido) titanium (99.99%-Ti Puratrem, STREM). Cerium deposition was done under 250°C for 14 cycles with a deposition of 0.3 Å/ cycle using Tris(isopropylcyclopentadienyl)cerium(III) (99.9%-Ce, REO, STREM). For the bimetallic sample with both Ce and Ti, C- Zif-8 was first deposited with Ti and then with Ce using the conditions stated above. The samples deposited with Ti are denoted C-Zif-8-Ti, with Ce are denoted C-Zif-8-Ce and the bimetallic samples are denoted C-Zif-8-CeTi.

6.2.2 Material Characterization

Scanning electron microscopy (SEM) was used to get the overall morphology of the sample using a Zeiss Gemini SEM 500 using a working current of 0.4 kV . The energy dispersive x-ray spectra (EDS) was captured using a FEI Qunata 200 ESEM equipped with EDAX Gensiss software. Transmission electron microscopy (TEM) and scanning transmission electron microscopy (STEM) images were recorded on a 200 kV FEI monochromated F20 UT Tecnai system. The STEM image was acquired with a convergence angle of 10 mrad and a detection angle of 30 mrad. Energy filtered transmission electron microscopy (EFTEM) was used to visualize elemental distribution. Sample preparation for TEM samples included drop-casting ethanol-suspended catalyst upon a 3 mm Lacey B Carbon 400 mesh grid from Ted Pella, followed by ambient drying. X-ray photoelectron spectroscopy (XPS) was performed on a PHI Quantum 2000 system using a focused, monochromatic Al Kα X-ray (1486.6 eV) source for excitation and a spherical section analyzer (200 μm diameter X-ray beam incident to the surface normal; detector set at 45°). The collected data were referenced to an energy scale with binding energies for Cu $2p_{3/2}$ at 932.7 ± 0.1 eV and Au $4f_{7/2}$ at 84.0 ± 0.1 eV. For XPS, catalysts were dispersed in ethanol and drop-cast onto a cleaned Si wafer.

6.2.3 Electrochemical Characterization

The catalytic activity was evaluated with linear sweep voltammetry (LSV) using a potentiostat (SP-200, Bio-Logic Science Instruments) in either ring-disk electrode (RDE) or rotating ring-disk electrode (RRDE) setup (RRDE-3A, ALS Co. Ltd). Measurements were performed in a three-electrode setup with a graphite rod as the counter and Ag/AgCl (3.5 M KCl) or Hg/HgO (1 M NaOH) electrode as the reference electrodes. The working electrode was prepared by drop-casting each electrode ink onto a glassy carbon (GC) disk electrode or nickel (Ni) foam. The ink was prepared by immersing 5 mg of hybrid catalyst materials into 1 ml of 2:1 volume of ethanol to MiliQ water along with 10.75 μl of 5 wt% Nafion (Nafion D-521, Alfa Aesar). For Pt/C electrode, a 5 mg ml^{-1} Pt/C suspension was prepared by using a commercial 20 wt% Pt supported on carbon black

(Vulcan XC72). These samples were dried under N_2 at 2 standard cubic feet per hour (scfh). The loading mass for all samples measured on glassy carbon was 0.4 mg/cm^2. Then, O_2 and N_2 saturated environments were implemented by flowing high-purity O_2 and N_2 gas at 2 scfh into 80 ml of electrolyte for 30 min. All electrochemical data were expressed with respect to the reversible hydrogen electrode (RHE).

6.3 Results and Discussion

The SEM images in Figure 6-1. SEM micrographs of carbonized Zif-8 (C-Zif-8) (a) before ALD deposition, (b) after Ce ALD (C-Zif-8-Ce), (c) after Ti ALD (C-Zif-8-Ti) and then after bimetallic ALD of Ce and Ti (C-Zif-8-CeTi) confirm the overall polyhedron morphology of the carbonized Zif-8 (C-Zif-8). The polyhedron structures are range from 100 – 200 nm in size.[52] Post ALD, there is still remnants of the C-Zif-8 morphology, which will still have the high surface area and promote high surface area, which can potentially promote the exposure of catalytic active sites.[115,164] However, there is agglomeration presented in the post-ALD samples (C-Zif-8-Ce, C-Zif-8-Ti and C-Zif-8-CeTi). In some of the images, especially for C-Zif-8-CeTi, there is high contrast of white, which could be from the formation of films due to ALD of Ti and Ce. Usually, higher atomic dense materials scatter electrons more giving more signal, and thus looking brighter. Certainly, higher magnification images might show some particles that could be a result of ALD of the metallic samples.

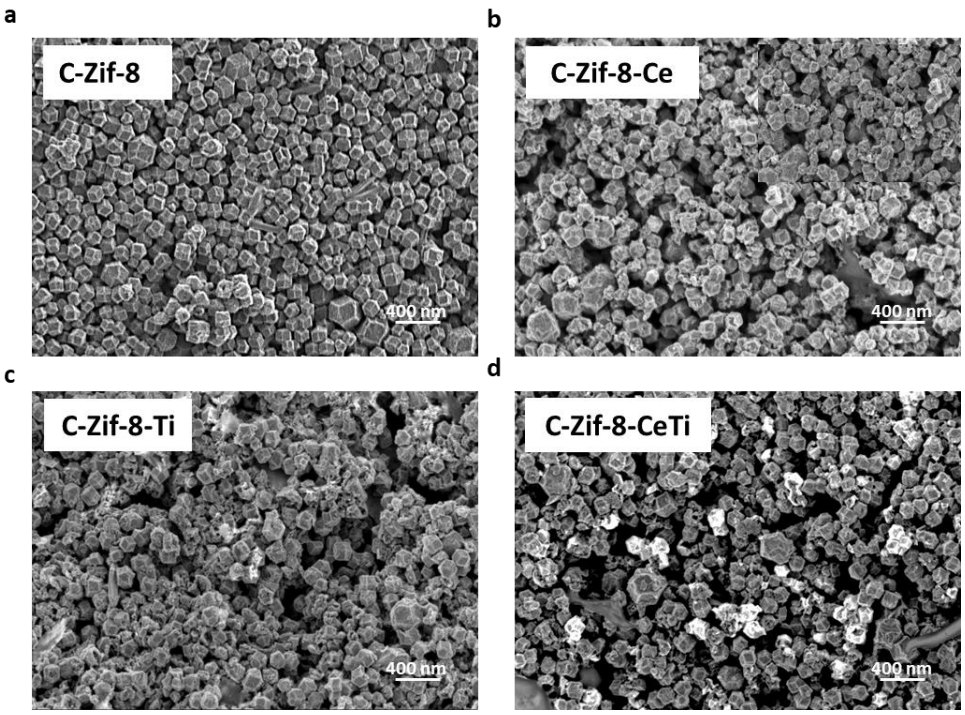

Figure 6-1. SEM micrographs of carbonized Zif-8 (C-Zif-8) (a) before ALD deposition, (b) after Ce ALD (C-Zif-8-Ce), (c) after Ti ALD (C-Zif-8-Ti) and then after bimetallic ALD of Ce and Ti (C-Zif-8-CeTi)

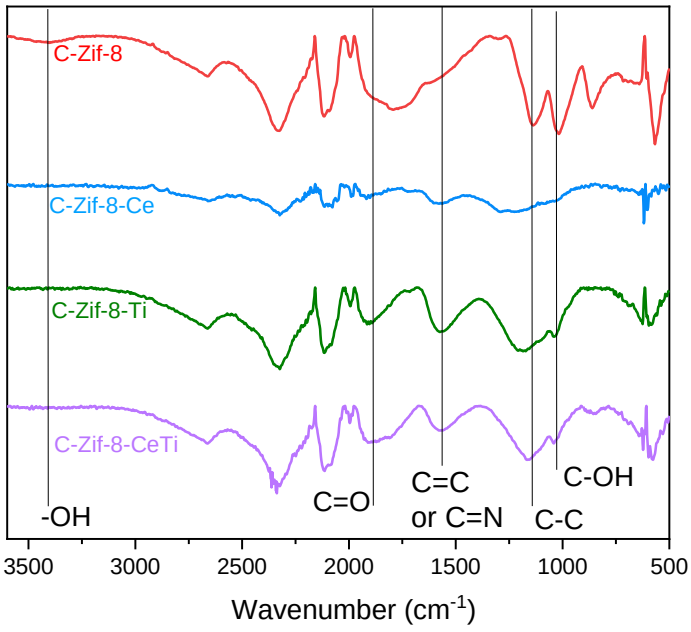

Figure 6-2 FTIR spectra of C-Zif-8, C-Zif-8-Ce, C-Zif-8-Ti and C-Zif-CeTi

The FTIR spectra in Figure 6.2 shows the presence of the following functional groups which include: OH (3550 cm^{-1}), C=O (1875 cm^{-1}), C=C or C=N (1563 cm^{-1}), C-C (1143 cm^{-1}) and C-OH (1015 cm^{-1}), and give an insight on what functional might have attached the metals that were deposited by ALD. The peak corresponding for OH is no longer present after ALD of Ce and Ti, this could signify that the metals have attached to these groups.[165,166] In addition, for C-Zif-8-Ce sample shows a decrease in the C=O after ALD, which can also show that Ce has attached to the carbonyl groups present in C-Zif-8. Both C-Zif-8-Ti and C-Zif-8-CeTi have similar spectra, with the absence of the hydroxyl group, but the peak corresponding to carbonyl is still present. However, there is a change before and after ALD for C-Zif-8-Ti, C-Zif-8-Ce, and C-Zif-8-TiCe. For the C-Zif-8 sample, the C-C and C-OH peak are quite distinguishable, but it seems those peaks are less defined in the samples post-ALD.

Table 6.1:	Relative atomic percentages (%)			
Specimen	C-Zif-8	C-Zif-8-Ce	C-Zif-8-Ti	C-Zif-8-CeTi
C	52.44	59.4	59.61	58.4
N	17.22	21.25	17.27	18.39
O	24.21	16.51	20.31	19.68
Ce	-	1.76	-	0.54
Ti	-	-	1.34	2.17

Table 6.1 The table is shows the relative atomic percentages of all samples, and it was derived from a full-range XPS spectra

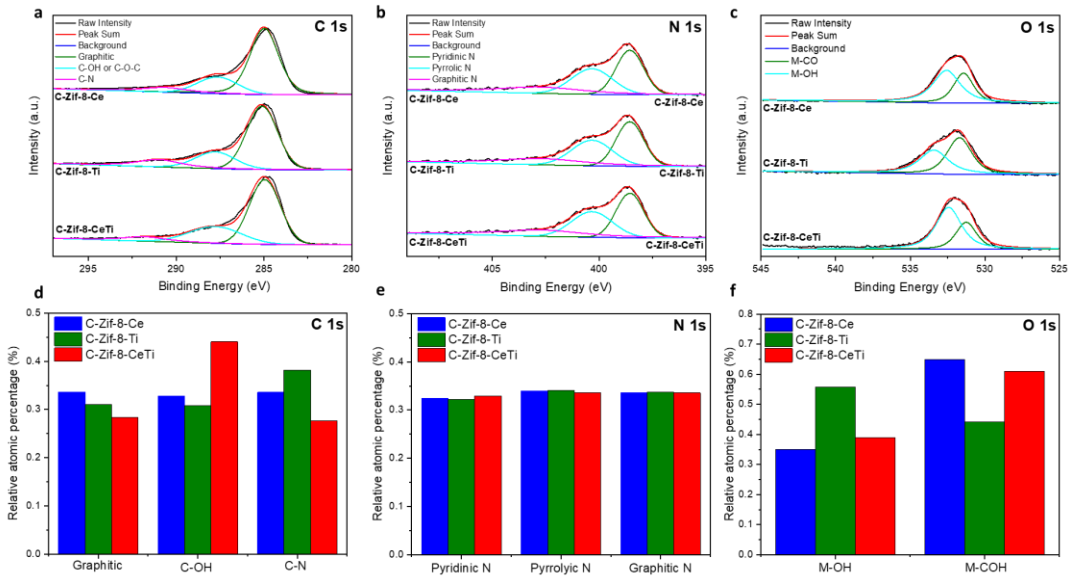

Figure 6-3 (a-c) XPS spectra of samples (a) C 1s, (b) N1s, and (c) O 1s. (d-f) Relative atomic percentage (%) of species deduced from the XPS spectra shown in (a-c).

X-ray photoelectron spectroscopy (XPS) was done to identify the chemical composition and valence states of the samples. The spectra shown in Figure 6.3 and

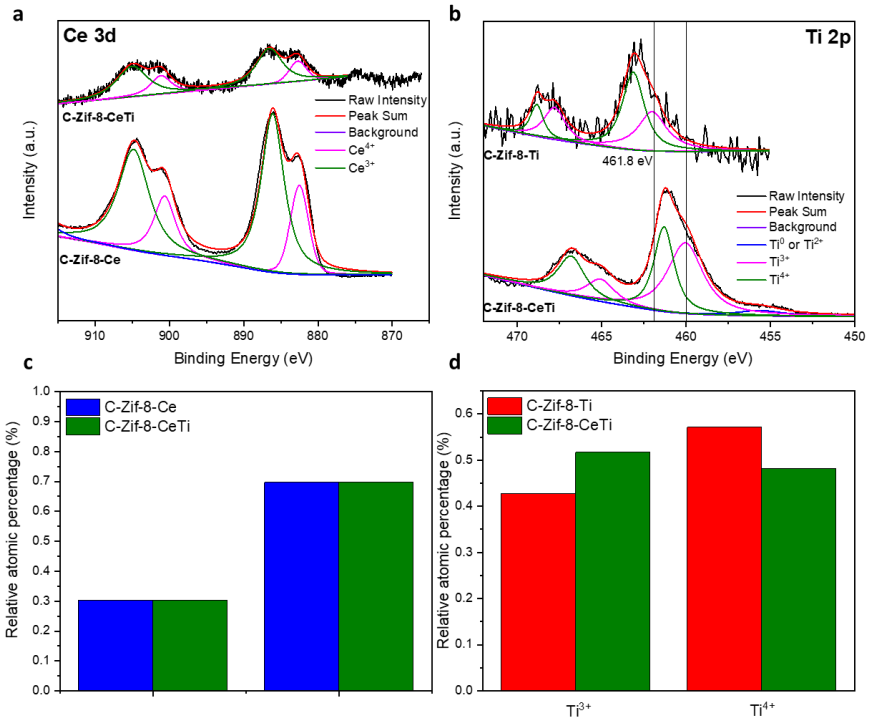

Figure 6-4 shows the presence of C, N, O, Ce and Ti. For all samples the majority of the composition, as seen in Table 6.1, is carbon with atomic percent, over 50% for all samples. Nitrogen and oxygen are the second highest with their relative atomic percentage ranging from about 16 to 24%. While both metals are close to 1-2 atomic percent. It seems the Ti percentage is in both monometallic and bimetallic samples are comparable, with the bimetallic sample having a slightly higher amount of Ti atomic percentage. On the other hand, the Ce content is higher for C-Zif-8-Ce than in the bimetallic sample, C-Zif-8-CeTi. This could be because of the method that was used to introduce the Ce, which was done after the Ti deposition instead of the common alternating cycles of each precursor. It could be that the Ti deposition had taken over the functional groups where Ce could have bonded and therefore the incorporation of Ce by ALD was limited.

As for the oxidation states and composition based on peak location the following was determined. For the C 1s spectra (

Figure 6-3.a) all samples exhibited peaks around 284.6 eV, 287.3 and 292.4 eV, which correspond to graphitic carbon/C-N, C-OH/C-O-C, and C-N/C=O, respectively. When comparing the relative atomic percentage of each of the peaks it seems that the bimetallic sample C-Zif-8-CeTi has relatively higher carboxyl and carboxide groups. Whereas C-Zif-8-Ce has slightly higher graphitic C and C-Zif-8-Ti has higher C-N and carbonyl groups C=O (

Figure 6-3.d). For N 1s (

Figure 6-3.b) spectra of all the samples, there are peaks located at around 398.7, 400.7 and 402.2 eV, which correspond to pyridinic N, pyrrolic N, and graphitic N, respectively. This not only confirms the incorporation and presence of nitrogen, but also the N-doping of the carbonized support structure. The relative atomic percentage for all the corresponding peaks of N 1s are relatively the same for all the specimens around 33 relative atomic%. The O 1s spectra (

Figure 6-3.c) shows peaks at around 531.5 eV is usually associated with metal carbonates and carboxylic bonding, which not only confirms the incorporation of Ti and Ce metal in the C-Zif-8, but it also confirms the C-O present in the sample that are supplemented by the C 1s.

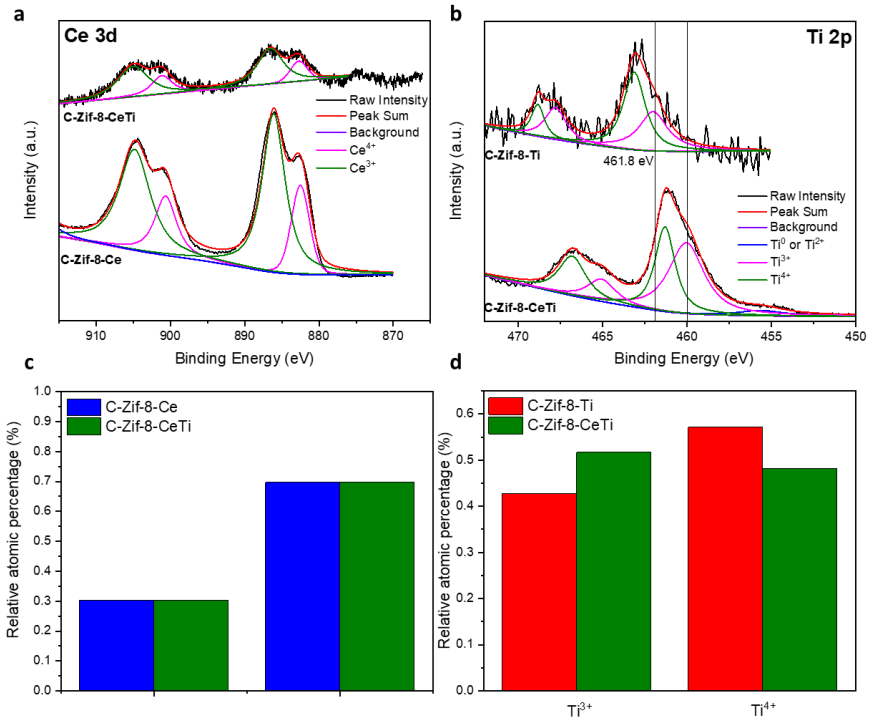

Figure 6-4 XPS spectra of samples (a) Ce 3d and (b) Ti 2p. (c) and (d) Relative atomic percentage (%) of species deduced from the respective XPS spectra shown in (a) and (b).

The metal incorporation characterized by XPS, shows some interesting oxidation states for the bimetallic sample, C-Zif-8-CeTi that could have led to its improved performance for both OER and HER. As seen in Figure 6-4.a for Ce 3d spectra the peaks present show both 3d $^{5}/_{2}$ and 3d $^{3}/_{2}$ that correspond to Ce $^{4+}$ at around 881.7 eV and Ce^{3+} at around 886 eV. The bimetal sample, C-Zif-8-CeTi, and C-Zif-8-Ce have very similar atomic of Ce^{3+} and Ce^{4+} (Figure 6-4.c), which could have some correlation as to why it had an overall better performance than the rest of the samples. In contrast, for the Ti 2p spectra it showed differences in different oxidation states between the bimetallic and monometallic sample. Even though both samples have relatively similar atomic percentages of Ti, Figure 6-4.d shows that there are higher amounts of Ti^{3+} in C-Zif-8-CeTi than in comparison to Ti^{4+}. In contrast, C-Zif-8-Ti had higher Ti^{3+} content. However, it seems for

both metals, C-Zif-8-CeTi has a higher atomic percentage of lower oxidation states of both metals.

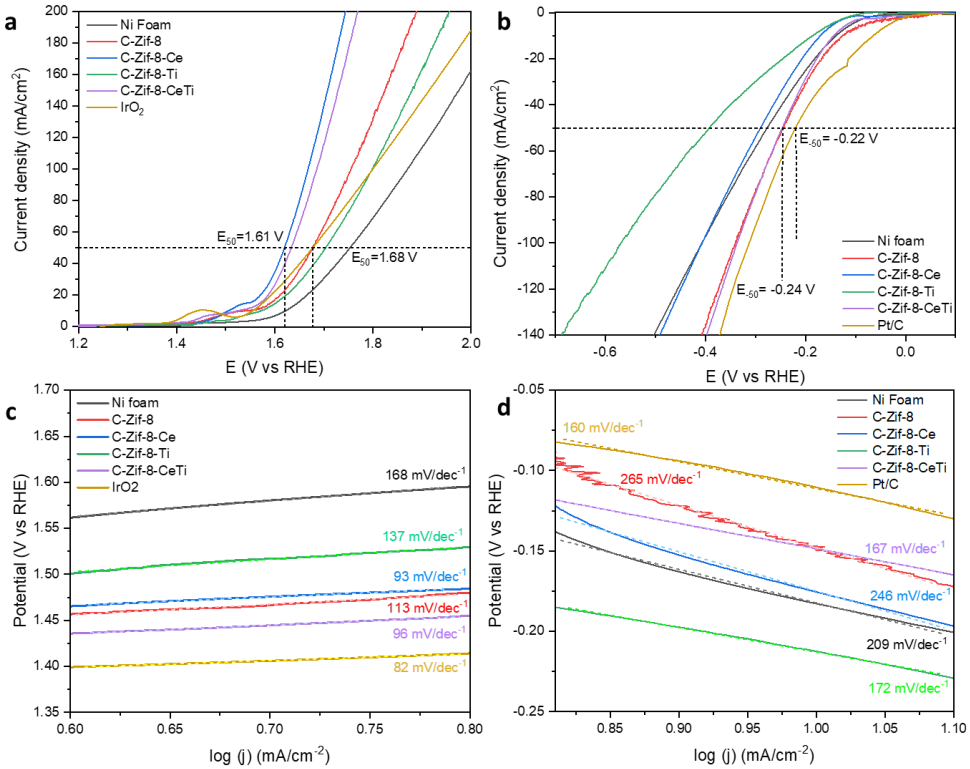

Figure 6-5 are LSV voltammogram for (a) OER and (b) HER. (d and c) Tafel plotes with Tafel slope values for OER and HER. All obtained in 1 M KOH under N_2 environment.

The electrocatalytic performance of the three samples were obtained under alkaline environment using 1 M KOH. Since the samples were deposited onto a Ni foam. In Figure 6-5.a the OER LSV voltammograms show that the best performing sample C-Zif-8-Ce reaching 50 mA/cm^2 at around 1.61 V vs RHE. The second-best sample was the bimetallic sample, C-Zif-8-CeTi, 50 mA/cm^2 at around 1.62 V vs RHE. Both samples outperform the benchmark IrO_2, which reaches 50 mA/cm^2 at around 1.68 V vs RHE. Since it has a higher potential. For HER, (Figure 6-5.b) the best performing is the noble meal benchmark Pt/C with an overpotential of 0.22 V at 50 mA/cm^2. However, C-Zif-8-CeTi and C-Zif-8, which doesn't contain any metal, had comparable HER electrocatalytic

performance to Pt/C reaching -50 mA/cm^2 at around 0.24 V. When comparing Tafel slopes (Figure 6-5.c and d) we see that both benchmarks have the lowest slope followed by the bimetallic samples.

Correlating the material characteristics and their performance we see a few things. For one, the bimetallic sample was the only sample that had good performance in both OER and HER. As seen in Figure 6.6, C-Zif-8-Ce and C-Zif-CeTi only differed by 10 mV of over potential. Overall, both samples had similar compositions based on what was quantified using XPS, especially having similar atomic percentages of oxidation states. Still, C-Zif-8-Ce had a higher relative atomic percentage of Ce could have led to more active sites for OER electrocatalysis formed by Ce. One difference that was evident between C-Zif-8-Ce and C-Zif-8-CeTi, is that the bimetallic sample has higher C-OH relative atomic percentage than C-Zif-8-Ce. This could signify why there was less Ce for the bimetallic sample, and as discussed previously this might be due to the synthesis method of depositing Ti first and the Ce during ALD. Overall, the presence of some sort of CeO_x formed by ALD can aid in the process of OER electrocatalyst. What is known about Ce-O_x catalytic active sites is that the intermediates of OER in an alkaline environment have weaker intermediate binding energies that favor the process.[167]

On the other hand, for HER the best performing sample was C-Zif-8 without any metal and C-Zif-8-CeTi. Both monometallic samples did not have good performance towards HER, with C-Zif-8-Ti have the worst performance for all the samples. This does show the possibility that most of the catalytic sites are either coming from the N-doped carbon or some bimetallic interaction between Ce and Ti. What is known about N-doped carbon electrocatalyst for HER especially both graphitic N and pyridinic N.[42,168] Even though, we didn't confirm Ti-O_x[169] is also a known electrocatalyst site for HER.

6.4 Conclusion

For this study, we synthesized a bifunctional electrocatalyst by carbonizing ZIF-8 (C-ZIF-8) that was then used as a substrate for ALD. Titanium (Ti) and cerium (Ce) precursors were deposited on C-ZIF-8 to create bimetal (C-Zif-8-CeTi) and monometal

(C-Zif-8-Ce or C-Zif-8-Ti) electrocatalyst. The bimetal-based electrocatalytic material, C-Zif-CeTi, showed promising performance for OER and HER reaching 50 mA/cm^2 at around 1.62 V vs RHE for OER and reaching -50 mA/cm^2 at around 0.24 V for HER. Some of the electrocatalytic sites that are suspected to be responsible for this bifunctional performance include the presence of CeO_x, TiO_x, and N-doped carbon complexes that are both stand-alone and synergistic catalytic active sites that promote the adsorption of reactants, desorption of products, and electron conductivity.

Limitations: In this study, we didn't explicitly show how the metals are atomically dispersed, so we would have to show higher magnification images, which includes TEM. In addition, use EDS to characterize the elemental composition of the structures we image to verify the distribution and Ti and Ce. Also, we did not discuss anything regarding the structure or phases present in this material, so we would have to include XRD analysis and potential diffraction analysis using TEM. Overall, we still need to verify and identify if there is a synergistic effect between both metals and how it is correlated to their electrocatalytic performance.

7. CONCLUSION

In this thesis, two different methods were applied to synthesize inorganic/organic hybrid electrocatalysts for ORR, OER, and HER: an ALD-based metal oxide anchoring and a solvothermal approach. The electrocatalytic performance of the resulting hybrid catalysts was characterized, and relevant discussions were provided.

1) We were successful in synthesizing electrocatalysts that have comparable or even exceeding electrocatalytic activity to that of noble metal-based benchmark.

2) The electrocatalytic performance for each electrocatalyst was then correlated to specific characteristic attributes of the materials in terms of structure, composition, and chemical states.

In the first study, a hybrid catalyst synthesized through a metal-organic framework-based process (M-NC-CoCu) enables active trifunctional catalysis due to its multi-faceted favorable characteristics. The presence of both Cu and Co species is conjectured to have deterred the agglomeration of each other and form well-dispersed active sites such as Cu-N_x, Cu-O_x, and $CuCo_2O_4$. The excellent electrocatalytic performance of M-NC-CoCu can be ascribed to multiple factors: (1) the high-surface-area structure of carbon matrix, (2) uniformly distributed tiny-sized catalytically active sites such as $CuCo_2O_4$ phases as well as Cu-O_x, Cu-N_x, and Co-N_x moieties, (3) high concentration of graphitic and pyridinic nitrogen, and (4) high concentration of sp^2 bonding beneficial for electronic conduction. The multitude of active sites derived from bimetallic Cu and Co species and N-doped carbon support of M-NC-CoCu prove to be effective in catalyzing ORR, OER, and HER. This study suggests that a bimetallic mixture and doping can result in multiple favorable effects that can be highly leveraged for efficient trifunctional electrocatalyst

The second study investigated the catalytic activities of TiO_2 incorporated GO where TiO_2 incorporation was achieved by ALD. The catalytic activity was systematically measured by CV. TiO_2 nanoparticles sized < 10 nm were successfully deposited evenly

on GO surface by ALD. A higher number of ALD cycles resulted in an overall better ORR performance in terms of on-set potential and active surface area. At 25 ALD cycles, the performance, especially in terms of on-set potential, reaches an optimum. It was also found that the chamber temperature for ALD process renders a positive impact on the catalytic performance when the same ALD cycle number of 25 was used. It is conjectured that a higher temperature resulted in a further reduction of GO (and thus an improved electronic conductivity of graphene scaffold) and facilitated nucleation and crystallization of TiO_2 nanoparticles.

For this study, we synthesized a bifunctional electrocatalyst by carbonizing ZIF-8 (C-ZIF-8) that was then used as a substrate for ALD. Titanium (Ti) and cerium (Ce) precursors were deposited on C-ZIF-8 to create bimetal (C-Zif-8-CeTi) and monometal (C-Zif-8-Ce or C-Zif-8-Ti) electrocatalyst. The bimetal-based electrocatalytic material, C-Zif-CeTi, showed promising performance for OER and HER reaching 50 mA/cm^2 at around 1.62 V vs RHE for OER and reaching -50 mA/cm^2 at around 0.24 V for HER. Some of the electrocatalytic sites that are suspected to be responsible for this bifunctional performance include the presence of CeO_x, TiO_x, and N-doped carbon complexes that are both stand-alone and synergistic catalytic active sites that promote the adsorption of reactants, desorption of products, and electron conductivity.

While the aforementioned studies show promises of each organic/inorganic hybrid material as multifunctional electrocatalyst, an in-depth mechanism study to reveal the process-property-performance correlation is expected to provide a useful insight in designing high-performance catalysts from these approaches.

8. REFERENCES

1. Winter, M. & Brodd, R. J. What are batteries, fuel cells, and supercapacitors? *Chem. Rev.* **104**, 4245–4269 (2004).

2. Han, L., Dong, S. & Wang, E. Transition-Metal (Co, Ni, and Fe)-Based Electrocatalysts for the Water Oxidation Reaction. *Adv. Mater.* **28**, 9266–9291 (2016).

3. Serov, A., Artyushkova, K. & Atanassov, P. Fe-N-C oxygen reduction fuel cell catalyst derived from carbendazim: Synthesis, structure, and reactivity. *Adv. Energy Mater.* **4**, 1–7 (2014).

4. Dai, L., Xue, Y., Qu, L., Choi, H.-J. & Baek, J.-B. Metal-Free Catalysts for Oxygen Reduction Reaction. *Chem. Rev.* **115**, 4823–4892 (2015).

5. Masa, J., Xia, W., Muhler, M. & Schuhmann, W. On the Role of Metals in Nitrogen-Doped Carbon Electrocatalysts for Oxygen Reduction Angewandte. *Angew. Chemie Int. Ed.* **54**, 10102–10120 (2015).

6. Shui, J., Wang, M., Du, F. & Dai, L. N-doped carbon nanomaterials are durable catalysts for oxygen reduction reaction in acidic fuel cells. *Sci. Adv.* 1–7 (2015).

7. Chen, G., Bare, S. R. & Mallouk, T. E. Development of Supported Bifunctional Electrocatalysts for Unitized Regenerative Fuel Cells. *J. Electrochem. Soc.* **149**, A1092 (2002).

8. Alayoglu, S., Nilekar, A. U., Mavrikakis, M. & Eichhorn, B. Ru–Pt core–shell nanoparticles for preferential oxidation of carbon monoxide in hydrogen. (2008). doi:10.1038/nmat2156

9. Gorlin, Y. & Jaramillo, T. F. A Bifunctional Nonprecious Metal Catalyst for Oxygen Reduction and Water Oxidation. doi:10.1021/ja104587v

10. Liang, Y. *et al.* Co3O4 nanocrystals on graphene as a synergistic catalyst for

oxygen reduction reaction. *Nat. Mater.* **10**, 780–786 (2011).

11. Ding, J., Zhou, Y., Li, Y., Guo, S. & Huang, X. MoS 2 Nanosheet Assembling Superstructure with a Three- Dimensional Ion Accessible Site: A New Class of Bifunctional Materials for Batteries and Electrocatalysis. doi:10.1021/acs.chemmater.5b04815

12. Qu, L., Liu, Y., Baek, J.-B. B. & Dai, L. Nitrogen-doped graphene as efficient metal-free electrocatalyst for oxygen reduction in fuel cells. *ACS Nano* **4**, 1321–1326 (2010).

13. Grigoriev, S. A. *et al.* Design and characterization of bi-functional electrocatalytic layers for application in PEM unitized regenerative fuel cells. *Int. J. Hydrogen Energy* **35**, 5070–5076 (2009).

14. Yang, H., Zhang, Y., Hu, F. & Wang, Q. Urchin-like CoP Nanocrystals as Hydrogen Evolution Reaction and Oxygen Reduction Reaction Dual-Electrocatalyst with Superior Stability. *Nano Lett.* **15**, 7616–7620 (2015).

15. Duan, J., Chen, S. & Zhao, C. Ultrathin metal-organic framework array for efficient electrocatalytic water splitting. *Nat. Commun.* **8**, 1–7 (2017).

16. Cao, X. *et al.* Metal oxide-coated three-dimensional graphene prepared by the use of metal-organic frameworks as precursors. *Angew. Chemie - Int. Ed.* **53**, 1404–1409 (2014).

17. Aijaz, A. *et al.* Co@Co 3 O 4 Encapsulated in Carbon Nanotube-Grafted Nitrogen-Doped Carbon Polyhedra as an Advanced Bifunctional Oxygen Electrode. *Angew. Chemie Int. Ed.* **55**, 4087–4091 (2016).

18. Pei, D.-N. *et al.* ARTICLE Defective titanium dioxide single crystals exposed by high-energy {001} facets for efficient oxygen reduction. (2015). doi:10.1038/ncomms9696

19. Zhang, Y., Gao, L., Hensen, E. J. M. & Hofmann, J. P. Evaluating the Stability of Co2P Electrocatalysts in the Hydrogen Evolution Reaction for Both Acidic and

Alkaline Electrolytes. *ACS Energy Lett.* **3**, 1360–1365 (2018).

20. Ioroi, T., Siroma, Z., Fujiwara, N., Yamazaki, S. & Yasuda, K. Sub-stoichiometric titanium oxide-supported platinum electrocatalyst for polymer electrolyte fuel cells. **7**, 183–188 (2005).

21. Close, T., Tulsyan, G., Diaz, C. a, Weinstein, S. J. & Richter, C. Reversible oxygen scavenging at room temperature using electrochemically reduced titanium oxide nanotubes. *Nat. Nanotechnol.* **10**, 418–22 (2015).

22. Jahan, M., Liu, Z. & Loh, K. P. A graphene oxide and copper-centered metal organic framework composite as a tri-functional catalyst for HER, OER, and ORR. *Adv. Funct. Mater.* **23**, 5363–5372 (2013).

23. Hod, I. *et al.* A porous proton-relaying metal-organic framework material that accelerates electrochemical hydrogen evolution. *Nat. Commun.* **6**, 1–9 (2015).

24. Wu, H.-W. A review of recent development: Transport and performance modeling of PEM fuel cells. (2016). doi:10.1016/j.apenergy.2015.12.075

25. Zhao, S., Yan, L., Luo, H., Mustain, W. & Xu, H. Recent progress and perspectives of bifunctional oxygen reduction/evolution catalyst development for regenerative anion exchange membrane fuel cells. *Nano Energy* **47**, 172–198 (2018).

26. Yan, D. *et al.* Defect Chemistry of Nonprecious-Metal Electrocatalysts for Oxygen Reactions. *Adv. Mater.* **29**, 1–20 (2017).

27. Barbir, F., Molter, T. & Dalton, L. Efficiency and weight trade-off analysis of regenerative fuel cells as energy storage for aerospace applications. *Int. J. Hydrogen Energy* **30**, 351–357 (2005).

28. Morozan, A., Jousselme, B. & Palacin, S. Low-platinum and platinum-free catalysts for the oxygen reduction reaction at fuel cell cathodes. *Energy Environ. Sci.* **4**, 1238 (2011).

29. Doyle, R. L. & Lyons, M. E. G. *The Oxygen Evolution Reaction : Mechanistic Concepts and Catalyst Design*. (2010). doi:10.1007/978-3-319-29641-8

30. Toda, T., Igarashi, H., Uchida, H. & Watanabe, M. Enhancement of the Electroreduction of Oxygen on Pt Alloys with Fe , Ni , and Co. **146**, 3750–3756 (1999).

31. Li, M. *et al.* Ultrafine jagged platinum nanowires enable ultrahigh mass activity for the oxygen reduction reaction. *Science* **354**, 1414–1419 (2016).

32. Greeley, J. *et al.* Alloys of platinum and early transition metals as oxygen reduction electrocatalysts. *Nat. Chem.* **1**, 552–556 (2009).

33. Johansson, M. B. NiFeO X as a Bifunctional Electrocatalyst for Oxygen Reduction (OR) and Evolution (OE) Reaction in Alkaline Media. **3**, 1–26 (2018).

34. Jin, H. *et al.* In situ cobalt-cobalt oxide/N-doped carbon hybrids as superior bifunctional electrocatalysts for hydrogen and oxygen evolution. *J. Am. Chem. Soc.* **137**, 2688–2694 (2015).

35. Osgood, H., Devaguptapu, S. V., Xu, H., Cho, J. & Wu, G. Transition metal (Fe, Co, Ni, and Mn) oxides for oxygen reduction and evolution bifunctional catalysts in alkaline media. *Nano Today* **11**, 601–625 (2016).

36. Zhang, C., Zhang, W. & Zheng, W. Transition Metal-Nitrogen-Carbon Active Site for Oxygen Reduction Electrocatalysis: Beyond the Fascinations of TM-N 4. *ChemCatChem* **11**, 655–668 (2019).

37. Wang, A., Li, J. & Zhang, T. Heterogeneous single-atom catalysis. *Nat. Rev. Chem.* **2**, 65–81 (2018).

38. Liu, M. *et al.* Atomically dispersed metal catalysts for the oxygen reduction reaction: Synthesis, characterization, reaction mechanisms and electrochemical energy applications. *Energy Environ. Sci.* **12**, 2890–2923 (2019).

39. Liang, Y., Wang, H., Casalongue, H. S., Chen, Z. & Dai, H. TiO 2 Nanocrystals

Grown on Graphene as Advanced Photocatalytic Hybrid Materials. **3**, 701–705 (2010).

40. Wang, L. *et al.* Dendritic copper-cobalt nanostructures/reduced graphene oxide-chitosan modified glassy carbon electrode for glucose sensing. *Sensors Actuators, B Chem.* **195**, 1–7 (2014).

41. Xia, B. Y. *et al.* A metal–organic framework-derived bifunctional oxygen electrocatalyst. *Nat. Energy* **1**, 15006 (2016).

42. Zhang, E. *et al.* Multifunctional high-activity and robust electrocatalyst derived from metal-organic frameworks. *J. Mater. Chem. A* **4**, 17288–17298 (2016).

43. Zhang, J., Zhao, Z., Xia, Z. & Dai, L. A metal-free bifunctional electrocatalyst for oxygen reduction and oxygen evolution reactions. *Nat. Nanotechnol.* **10**, 444–452 (2015).

44. Fu, Y., Huang, Y., Xiang, Z., Liu, G. & Cao, D. Phosphorous-Nitrogen-Codoped Carbon Materials Derived from Metal-Organic Frameworks as Efficient Electrocatalysts for Oxygen Reduction Reactions. *Eur. J. Inorg. Chem.* **2016**, 2100–2105 (2016).

45. Gong, K., Du, F., Xia, Z., Durstock, M. & Dai, L. Nitrogen-doped carbon nanotube arrays with high electrocatalytic activity for oxygen reduction. *Science* **323**, 760–764 (2009).

46. Yang, Z. *et al.* Sulfur-Doped Graphene as an Efficient Metal-free Cathode Catalyst for Oxygen Reduction. (2011). doi:10.1021/nn203393d

47. Yang, D.-S., Bhattacharjya, D., Song, M. Y. & Yu, J.-S. Highly efficient metal-free phosphorus-doped platelet ordered mesoporous carbon for electrocatalytic oxygen reduction. (2014). doi:10.1016/j.carbon.2013.10.065

48. Jia, Y. *et al.* Defect Graphene as a Trifunctional Catalyst for Electrochemical Reactions. *Adv. Mater.* **28**, 9532–9538 (2016).

49. Li, X. *et al.* ZIF-67-derived Co-NC@CoP-NC nanopolyhedra as an efficient bifunctional oxygen electrocatalyst. 15836–15840 (2016). doi:10.1039/c6ta06434e

50. Liang, Y. *et al.* Covalent hybrid of spinel manganese-cobalt oxide and graphene as advanced oxygen reduction electrocatalysts. *J. Am. Chem. Soc.* **134**, 3517–3523 (2012).

51. Kibsgaard, J. & Jaramillo, T. F. Molybdenum phosphosulfide: An active, acid-stable, earth- Abundant catalyst for the hydrogen evolution reaction. *Angew. Chemie - Int. Ed.* **53**, 14433–14437 (2014).

52. Wang, G. *et al.* Highly active atomically dispersed CoN 4 fuel cell cathode catalysts derived from surfactant-assisted MOFs: Carbon-shell confinement strategy. *Energy Environ. Sci.* **12**, 250–260 (2019).

53. Tao, L. *et al.* Creating coordinatively unsaturated metal sites in metal-organic-frameworks as efficient electrocatalysts for the oxygen evolution reaction: Insights into the active centers. *Nano Energy* **41**, 417–425 (2017).

54. Xu, L. *et al.* Plasma-Engraved Co 3 O 4 Nanosheets with Oxygen Vacancies and High Surface Area for the Oxygen Evolution Reaction. *Angew. Chemie* **128**, 5363–5367 (2016).

55. Wang, Y. *et al.* Reduced mesoporous Co3O4nanowires as efficient water oxidation electrocatalysts and supercapacitor electrodes. *Adv. Energy Mater.* **4**, 1–7 (2014).

56. Cheng, F. *et al.* Rapid room-temperature synthesis of nanocrystalline spinels as oxygen reduction and evolution electrocatalysts. (2011). doi:10.1038/NCHEM.931

57. Adamson, W. *et al.* Co-Fe binary metal oxide electrocatalyst with synergistic interface structures for efficient overall water splitting. *Catal. Today* 0–1 (2019). doi:10.1016/j.cattod.2019.01.060

58. Wang, D. *et al.* Coordination-Engineered Cu-Nx Single-Site Catalyst for Enhancing Oxygen Reduction Reaction. *ACS Appl. Energy Mater.* **2**, 6497–6504

(2019).

59. Zhao, S. *et al.* Ultrathin metal-organic framework nanosheets for electrocatalytic oxygen evolution. *Nat. Energy* **1**, 1–10 (2016).

60. Dai, X. *et al.* Molybdenum Polysulfide Anchored on Porous Zr-Metal Organic Framework to Enhance the Performance of Hydrogen Evolution Reaction. *J. Phys. Chem. C* **120**, 12539–12548 (2016).

61. Furukawa, H., Cordova, K. E., O'Keeffe, M. & Yaghi, O. M. The chemistry and applications of metal-organic frameworks. *Science (80-.).* **341**, (2013).

62. Kim, J. H. *et al.* High-performance fuel cell cathodes exclusively containing atomically dispersed iron active sites. *Energy Environ. Sci.* **12**, 2548–2558 (2019).

63. Yan, L. *et al.* Metal-Organic Frameworks Derived Nanotube of Nickel-Cobalt Bimetal Phosphides as Highly Efficient Electrocatalysts for Overall Water Splitting. *Adv. Funct. Mater.* **27**, 1703455 (2017).

64. Liu, P. *et al.* Cu and Co nanoparticle-Co-decorated N-doped graphene nanosheets: a high efficiency bifunctional electrocatalyst for rechargeable Zn–air batteries. *J. Mater. Chem. A* **7**, 12851–12858 (2019).

65. Cheng, H., Li, M.-L., Su, C.-Y., Li, N. & Liu, Z.-Q. Cu-Co Bimetallic Oxide Quantum Dot Decorated Nitrogen-Doped Carbon Nanotubes: A High-Efficiency Bifunctional Oxygen Electrode for Zn-Air Batteries. *Adv. Funct. Mater.* **27**, 1701833 (2017).

66. Li, Z. *et al.* Structural Modulation of Co Catalyzed Carbon Nanotubes with Cu–Co Bimetal Active Center to Inspire Oxygen Reduction Reaction. *ACS Appl. Mater. Interfaces* **11**, 3937–3945 (2019).

67. Kuang, M., Wang, Q., Han, P. & Zheng, G. Cu, Co-Embedded N-Enriched Mesoporous Carbon for Efficient Oxygen Reduction and Hydrogen Evolution Reactions. *Adv. Energy Mater.* **7**, 1–8 (2017).

68. Wang, Y., Tran, H. D., Liao, L., Duan, X. & Kaner, R. B. Nanoscale Morphology, Dimensional Control, and Electrical Properties of Oligoanilines. doi:10.1021/ja1014184

69. Peters, A. W., Li, Z., Farha, O. K. & Hupp, J. T. Atomically Precise Growth of Catalytically Active Cobalt Sulfide on Flat Surfaces and within a Metal–Organic Framework via Atomic Layer Deposition. *ACS Nano* **9**, 8484–8490 (2015).

70. O'Keeffe, M. & Yaghi, O. M. Deconstructing the crystal structures of metal-organic frameworks and related materials into their underlying nets. *Chem. Rev.* **112**, 675–702 (2012).

71. Chen, J., Lim, B., Lee, E. P. & Xia, Y. Shape-controlled synthesis of platinum nanocrystals for catalytic and electrocatalytic applications. *Nano Today* **4**, 81–95 (2009).

72. Nanostructures, Z. Zero-Dimensional Nanostructures: Nanoparticles 3.1. **c**, 51–81

73. Karthik, P., Pandikumar, A., Preeyanghaa, M., Kowsalya, M. & Neppolian, B. Amino-functionalized MIL-101(Fe) metal-organic framework as a viable fluorescent probe for nitroaromatic compounds. doi:10.1007/s00604-017-2215-2

74. Qu, Q. *et al.* Chemically Binding Carboxylic Acids onto TiO 2 Nanoparticles with Adjustable Coverage by Solvothermal Strategy. *Langmuir* **26**, 9539–9546 (2010).

75. Cundy, C. S. & Cox, P. A. The hydrothermal synthesis of zeolites: Precursors, intermediates and reaction mechanism. *Microporous Mesoporous Mater.* **82**, 1–78 (2005).

76. Pinna, N. & Knez, M. *Edited by Atomic Layer Deposition of Nanostructured Materials Related Titles Nanocomposites Bulk Nanostructured Materials Semiconductor Nanomaterials Handbook of Nitride Semiconductors and Devices Nanostructured Thin Films and Surfaces Electronic Material*. doi:10.1002/9783527639915

77. Neill, B. J. O. *et al.* Catalyst Design with Atomic Layer Deposition. *ACS Catal.* **5**,

1804–1825 (2015).

78. Lemaire, P. C., King, M. & Parsons, G. N. Understanding inherent substrate selectivity during atomic layer deposition: Effect of surface preparation, hydroxyl density, and metal oxide composition on nucleation mechanisms during tungsten ALD. *J. Chem. Phys.* **146**, (2017).

79. Stock, N. & Biswas, S. Synthesis of metal-organic frameworks (MOFs): Routes to various MOF topologies, morphologies, and composites. *Chem. Rev.* **112**, 933–969 (2012).

80. Ghanbari, T., Abnisa, F. & Wan Daud, W. M. A. A review on production of metal organic frameworks (MOF) for CO2 adsorption. *Sci. Total Environ.* **707**, 135090 (2020).

81. Zhang, H. *et al.* High-performance fuel cell cathodes exclusively containing atomically dispersed iron active sites. *Energy Environ. Sci.* **12**, 2548–2558 (2019).

82. Yang, J. *et al.* Porous Molybdenum Phosphide Nano-Octahedrons Derived from Confined Phosphorization in UIO-66 for Efficient Hydrogen Evolution. *Angew. Chemie - Int. Ed.* **55**, 12854–12858 (2016).

83. Liu, Y., Deng, R., Wang, Z. & Liu, H. Carboxyl-functionalized graphene oxide–polyaniline composite as a promising supercapacitor material. *J. Mater. Chem.* **22**, 13619 (2012).

84. Lee, K. J., Elgrishi, N., Kandemir, B. & Dempsey, J. L. Electrochemical and spectroscopic methods for evaluating molecular electrocatalysts. *Nat. Rev. Chem.* **1**, (2017).

85. Sui, S. *et al.* A comprehensive review of Pt electrocatalysts for the oxygen reduction reaction: Nanostructure, activity, mechanism and carbon support in PEM fuel cells. *J. Mater. Chem. A* **5**, 1808–1825 (2017).

86. Chen, Z., Higgins, D., Yu, A., Zhang, L. & Zhang, J. A review on non-precious metal electrocatalysts for PEM fuel cells. *Energy Environ. Sci.* **4**, 3167 (2011).

87. Wang, Z. L., Xu, D., Xu, J. J. & Zhang, X. B. Oxygen electrocatalysts in metal-air batteries: From aqueous to nonaqueous electrolytes. *Chemical Society Reviews* **43**, 7746–7786 (2014).

88. Hong, W. T. *et al.* Toward the rational design of non-precious transition metal oxides for oxygen electrocatalysis. *Energy Environ. Sci.* **8**, 1404–1427 (2015).

89. Liang, Y. *et al.* Co3O4 nanocrystals on graphene as a synergistic catalyst for oxygen reduction reaction. *Nat. Mater.* **10**, 780–786 (2011).

90. Su, Y. *et al.* Cobalt nanoparticles embedded in N-doped carbon as an efficient bifunctional electrocatalyst for oxygen reduction and evolution reactions. *Nanoscale* **6**, 15080–15089 (2014).

91. Ma, T. Y., Dai, S., Jaroniec, M. & Qiao, S. Z. Metal-organic framework derived hybrid Co3O4-carbon porous nanowire arrays as reversible oxygen evolution electrodes. *J. Am. Chem. Soc.* **136**, 13925–13931 (2014).

92. Nørskov, J. K. *et al.* Origin of the Overpotential for Oxygen Reduction at a Fuel-Cell Cathode. *J. Phys. Chem. B* **108**, 17886–17892 (2004).

93. Kuang, M., Han, P., Wang, Q., Li, J. & Zheng, G. CuCo Hybrid Oxides as Bifunctional Electrocatalyst for Efficient Water Splitting. *Adv. Funct. Mater.* **26**, 8555–8561 (2016).

94. Jung, M., Scott, J., Ng, Y. H., Jiang, Y. & Amal, R. CuO x dispersion and reducibility on TiO 2 and its impact on photocatalytic hydrogen evolution. *Int. J. Hydrogen Energy* **39**, 12499–12506 (2014).

95. Rasul, S. *et al.* A Highly Selective Copper-Indium Bimetallic Electrocatalyst for the Electrochemical Reduction of Aqueous CO 2 to CO . *Angew. Chemie* **127**, 2174–2178 (2015).

96. Tabassum, H. *et al.* Metal–Organic Frameworks Derived Cobalt Phosphide Architecture Encapsulated into B/N Co-Doped Graphene Nanotubes for All pH Value Electrochemical Hydrogen Evolution. *Adv. Energy Mater.* **7**, 1–7 (2017).

97. Shah, S. S. A. *et al.* Monodispersed Co in Mesoporous Polyhedrons: Fine-tuning of ZIF-8 Structure with Enhanced Oxygen Reduction Activity. *Electrochim. Acta* **251**, 498–504 (2017).

98. Li, F. *et al.* Boosting oxygen reduction catalysis with abundant copper single atom active sites. *Energy Environ. Sci.* **11**, 2263–2269 (2018).

99. Lai, Q. *et al.* Directly Anchoring Highly Dispersed Copper Sites on Nitrogen-Doped Carbon for Enhanced Oxygen Reduction Electrocatalysis. *ChemElectroChem* **5**, 1822–1826 (2018).

100. Han, X. *et al.* Generation of Nanoparticle, Atomic-Cluster, and Single-Atom Cobalt Catalysts from Zeolitic Imidazole Frameworks by Spatial Isolation and Their Use in Zinc-Air Batteries. *Angew. Chemie Int. Ed.* **58**, 5359–5364 (2019).

101. Zhang, H. *et al.* Uniform copper–cobalt phosphides embedded in N-doped carbon frameworks as efficient bifunctional oxygen electrocatalysts for rechargeable Zn–air batteries. *Nanoscale* **11**, 17384–17395 (2019).

102. Niu, W. *et al.* Understanding Synergism of Cobalt Metal and Copper Oxide toward Highly Efficient Electrocatalytic Oxygen Evolution. *ACS Catal.* **8**, 12030–12040 (2018).

103. Wang, X. *et al.* Electrospun Thin-Walled CuCo 2 O 4 @C Nanotubes as Bifunctional Oxygen Electrocatalysts for Rechargeable Zn–Air Batteries. *Nano Lett.* **17**, 7989–7994 (2017).

104. Rotondo, A., Bruno, G., Brancatelli, G., Nicolò, F. & Armentano, D. A phenyl-salicyliden-imine as a suitable ligand to build functional materials. *Inorganica Chim. Acta* **362**, 247–252 (2009).

105. Li, W. Z. *et al.* Fabrication of monodisperse flower-like coordination polymers (CP) microparticles by spray technique. *Nanomaterials* **7**, (2017).

106. Yang, Y. *et al.* Synthesis and characterization of three amino-functionalized metal-organic frameworks based on the 2-aminoterephthalic ligand. *Dalt. Trans.* **44**,

8190–8197 (2015).

107. Yin, P. *et al.* Single Cobalt Atoms with Precise N-Coordination as Superior Oxygen Reduction Reaction Catalysts. *Angew. Chemie* **128**, 10958–10963 (2016).

108. Xia, B. Y. *et al.* A metal–organic framework-derived bifunctional oxygen electrocatalyst. *Nat. Energy* **1**, 15006 (2016).

109. Van Khai, T. *et al.* Significant enhancement of blue emission and electrical conductivity of N-doped graphene. *J. Mater. Chem.* **22**, 17992–18003 (2012).

110. Shen, K., Chen, X., Chen, J. & Li, Y. Development of MOF-Derived Carbon-Based Nanomaterials for Efficient Catalysis. *ACS Catal.* **6**, 5887–5903 (2016).

111. Shen, M. *et al.* Covalent Entrapment of Cobalt–Iron Sulfides in N-Doped Mesoporous Carbon: Extraordinary Bifunctional Electrocatalysts for Oxygen Reduction and Evolution Reactions. *ACS Appl. Mater. Interfaces* **7**, 1207–1218 (2015).

112. Patterson, A. L. The Scherrer Formula for X-Ray Particle Size Determination. *Phys. Rev.* **56**, 978–982 (1939).

113. Fierro, G., Lo Jacono, M., Inversi, M., Dragone, R. & Porta, P. TPR and XPS study of cobalt-copper mixed oxide catalysts: Evidence of a strong Co-Cu interaction. *Top. Catal.* **10**, 39–48 (2000).

114. Yang, Y. *et al.* Incorporation of Cu–N_x cofactors into graphene encapsulated Co as biomimetic electrocatalysts for efficient oxygen reduction. *Nanoscale* **10**, 21076–21086 (2018).

115. Zhang, L. *et al.* Highly graphitized nitrogen-doped porous carbon nanopolyhedra derived from ZIF-8 nanocrystals as efficient electrocatalysts for oxygen reduction reactions. *Nanoscale* **6**, 6590–6602 (2014).

116. Jiang, Y. *et al.* A cobalt–nitrogen complex on N-doped three-dimensional graphene framework as a highly efficient electrocatalyst for oxygen reduction

reaction. *Nanoscale* **6**, 15066–15072 (2014).

117. Yang, Y. *et al.* Incorporation of Cu – N x cofactors into graphene encapsulated Co as biomimetic electrocatalysts for e ffi cient oxygen reduction †. 21076–21086 (2018). doi:10.1039/c8nr06538a

118. Yu, H., Fisher, A., Cheng, D. & Cao, D. Cu,N-codoped Hierarchical Porous Carbons as Electrocatalysts for Oxygen Reduction Reaction. *ACS Appl. Mater. Interfaces* **8**, 21431–21439 (2016).

119. Yang, H. Bin *et al.* Identification of catalytic sites for oxygen reduction and oxygen evolution in N-doped graphene materials: Development of highly efficient metal-free bifunctional electrocatalyst. *Sci. Adv.* **2**, e1501122 (2016).

120. Wang, Z. *et al.* Fe, Cu-Coordinated ZIF-Derived Carbon Framework for Efficient Oxygen Reduction Reaction and Zinc-Air Batteries. *Adv. Funct. Mater.* **28**, 1802596 (2018).

121. Wei, J. *et al.* Nitrogen-Doped Nanoporous Carbon/Graphene Nano-Sandwiches: Synthesis and Application for Efficient Oxygen Reduction. *Adv. Funct. Mater.* **25**, 5768–5777 (2015).

122. Jiang, H. *et al.* Defect-rich and ultrathin N doped carbon nanosheets as advanced trifunctional metal-free electrocatalysts for the ORR, OER and HER. *Energy Environ. Sci.* **12**, 322–333 (2019).

123. Zhu, Z., Yang, Y., Guan, Y., Xue, J. & Cui, L. Construction of a cobalt-embedded nitrogen-doped carbon material with the desired porosity derived from the confined growth of MOFs within graphene aerogels as a superior catalyst towards HER and ORR. *J. Mater. Chem. A* **4**, 15536–15545 (2016).

124. De Koninck, M., Poirier, S. & Marsan, B. Cu[sub x]Co[sub 3−x]O[sub 4] Used as Bifunctional Electrocatalyst. *J. Electrochem. Soc.* **153**, A2103 (2006).

125. Serov, A. *et al.* CuCo 2 O 4 ORR/OER Bi-Functional Catalyst: Influence of Synthetic Approach on Performance. *J. Electrochem. Soc.* **162**, F449–F454 (2015).

126. Wang, D. *et al.* Coordination-Engineered Cu–N x Single-Site Catalyst for Enhancing Oxygen Reduction Reaction. *ACS Appl. Energy Mater.* **2**, 6497–6504 (2019).

127. Biesinger, M. C. Advanced analysis of copper X-ray photoelectron spectra. *Surf. Interface Anal.* **49**, 1325–1334 (2017).

128. Xiang, X. *et al.* Sphere-and-Flake-Structured Cu, N Co-Doped Carbon Catalyst Designed by a Template-Free Method for Robust Oxygen Reduction Reaction. *ChemElectroChem* **6**, 1078–1087 (2019).

129. Zhu, Y. *et al.* Operando unraveling of the structural and chemical stability of P-substituted CoSe 2 electrocatalysts toward hydrogen and oxygen evolution reactions in alkaline electrolyte. *ACS Energy Lett.* **4**, 987–994 (2019).

130. Dhawale, D. S. *et al.* Hierarchically Ordered Porous CoOOH Thin-Film Electrodes for High-Performance Supercapacitors. *ChemElectroChem* **2**, 497–502 (2015).

131. Huerta, F., Cazorla-amor, D. & Morall, E. Copper-Doped Cobalt Spinel Electrocatalysts Evolution Reaction. *Materials (Basel).* (2019).

132. Xiao, Z. *et al.* Operando Identification of the Dynamic Behavior of Oxygen Vacancy-Rich Co3O4for Oxygen Evolution Reaction. *J. Am. Chem. Soc.* **142**, 12087–12095 (2020).

133. Seo, B. *et al.* Size-Dependent Activity Trends Combined with in Situ X-ray Absorption Spectroscopy Reveal Insights into Cobalt Oxide/Carbon Nanotube-Catalyzed Bifunctional Oxygen Electrocatalysis. *ACS Catal.* **6**, 4347–4355 (2016).

134. Wang, J. *et al.* Stabilizing the oxygen vacancies and promoting water-oxidation kinetics in cobalt oxides by lower valence-state doping. *Nano Energy* **53**, 144–151 (2018).

135. Mo, Q., Chen, N., Deng, M., Yang, L. & Gao, Q. Metallic Cobalt @ Nitrogen-Doped Carbon Nanocomposites : Carbon-Shell Regulation toward Efficient Bi-Functional Electrocatalysis. 1–9

136. Panda, C., Menezes, P. W., Zheng, M., Orthmann, S. & Driess, M. In Situ Formation of Nanostructured Core-Shell Cu 3 N-CuO to Promote Alkaline Water Electrolysis. *ACS Energy Lett.* **4**, 747–754 (2019).

137. Cao, L. *et al.* Identification of single-atom active sites in carbon-based cobalt catalysts during electrocatalytic hydrogen evolution. *Nat. Catal.* **2**, 134–141 (2019).

138. Flores-Lasluisa, J. X. *et al.* Copper-Doped Cobalt Spinel Electrocatalysts Supported on Activated Carbon for Hydrogen Evolution Reaction. *Materials (Basel).* **12**, 1302 (2019).

139. Jain, D. *et al.* Changes in Active Sites on Nitrogen-Doped Carbon Catalysts Under Oxygen Reduction Reaction: A Combined Post-Reaction Characterization and DFT Study. *ChemCatChem* **11**, 5945–5950 (2019).

140. Asahi, R., Morikawa, T., Ohwaki, T., Aoki, K. & Taga, Y. Visible-Light Photocatalysis in Nitrogen-Doped Titanium Oxides. **293**, 269–272 (2001).

141. Wang, L. & Sasaki, T. Titanium oxide nanosheets: Graphene analogues with versatile functionalities. *Chem. Rev.* **114**, 9455–9486 (2014).

142. Dreyer, D. R., Park, S., Bielawski, C. W. & Ruoff, R. S. The chemistry of graphene oxide. (2009). doi:10.1039/b917103g

143. Williams, G., Seger, B. & Kamat, P. V. TiO 2 -Graphene Nanocomposites. UV-Assisted Photocatalytic Reduction of Graphene Oxide. doi:10.1021/nn800251f

144. Pore, B. V. *et al.* Atomic Layer Deposition of Photocatalytic TiO 2 Thin Films From Titanium Tetramethoxide and Water **. 143–148 (2004). doi:10.1002/cvde.200306289

145. How, G. T. S., Pandikumar, A., Ming, H. N. & Ngee, L. H. Highly exposed {001} facets of titanium dioxide modified with reduced graphene oxide for dopamine sensing. *Sci. Rep.* **4**, 2–9 (2014).

146. Wang, X., Tabakman, S. M. & Dai, H. Atomic Layer Deposition of Metal Oxides on Pristine and Functionalized Graphene. *J. AM. CHEM. SOC* **130**, 8152–8153 (2008).

147. Williams, G., Seger, B. & Kamat, P. V. UV-Assisted Photocatalytic Reduction of Graphene Oxide. **2**, 1487–1491 (2008).

148. Reinke, M., Kuzminykh, Y. & Hoffmann, P. Surface Reaction Kinetics of Titanium Isopropoxide and Water in Atomic Layer Deposition. doi:10.1021/acs.jpcc.5b10529

149. Marcano, D. C. *et al.* Improved Synthesis of Graphene Oxide. **4**, (2010).

150. Hayashi, T. *et al.* Temperature dependence of oxygen reduction mechanism on a titanium oxide-based catalyst made from oxy-titanium tetra-pyrazino-porphyrazine using carbon nano-tubes as support in acidic solution. *Electrochim. Acta* (2016). doi:10.1016/j.electacta.2016.05.068

151. Ayissi, S. *et al.* Interaction of Titanium Oxide Nanostructures with Graphene and Functionalized Graphene Nanoribbons: A DFT Study. *J. Phys. Chem. C* **117**, 25424–25432 (2013).

152. Yao, Y. *et al.* High temperature shockwave stabilized single atoms. *Nat. Nanotechnol.* **14**, 851–857 (2019).

153. Chen, Y. *et al.* Single-Atom Catalysts: Synthetic Strategies and Electrochemical Applications. *Joule* **2**, 1242–1264 (2018).

154. Qiao, M. *et al.* Hierarchically Ordered Porous Carbon with Atomically Dispersed FeN4 for Ultraefficient Oxygen Reduction Reaction in Proton-Exchange Membrane Fuel Cells. *Angew. Chemie - Int. Ed.* **59**, 2688–2694 (2020).

155. Liang, Z., Qu, C., Xia, D., Zou, R. & Xu, Q. Atomically Dispersed Metal Sites in MOF-Based Materials for Electrocatalytic and Photocatalytic Energy Conversion. *Angew. Chemie - Int. Ed.* **57**, 9604–9633 (2018).

156. Chen, Y. *et al.* Isolated Single Iron Atoms Anchored on N-Doped Porous Carbon as an Efficient Electrocatalyst for the Oxygen Reduction Reaction. *Angew. Chemie - Int. Ed.* **56**, 6937–6941 (2017).

157. Ren, G. *et al.* A bio-inspired Co3O4-polypyrrole-graphene complex as an efficient oxygen reduction catalyst in one-step ball milling. *Nano Res.* **8**, 3461–3471 (2015).

158. Qin, R., Liu, P., Fu, G. & Zheng, N. Strategies for Stabilizing Atomically Dispersed Metal Catalysts. *Small Methods* **2**, 1–21 (2018).

159. Guo, H. C., Ye, E., Li, Z., Han, M.-Y. & Loh, X. J. Recent progress of atomic layer deposition on polymeric materials. *Mater. Sci. Eng. C* **70**, 1182–1191 (2017).

160. Finke, C. E. *et al.* Enhancing the activity of oxygen-evolution and chlorine-evolution electrocatalysts by atomic layer deposition of TiO 2. *Energy Environ. Sci.* **12**, 358–365 (2019).

161. Kung, C. *et al.* Metal − Organic Framework Thin Films as Platforms for Atomic Layer Deposition of Cobalt Ions To Enable Electrocatalytic Water Oxidation. (2015). doi:10.1021/acsami.5b06901

162. Sun, S. *et al.* Single-atom catalysis using Pt/graphene achieved through atomic layer deposition. *Sci. Rep.* **3**, 97–99 (2013).

163. Yao, Y., Coyle, J. P., Barry, S. T. & Zaera, F. Effect of the nature of the substrate on the surface chemistry of atomic layer deposition precursors. *J. Chem. Phys.* **146**, 052806 (2017).

164. Tanaka, S., Kida, K., Okita, M., Ito, Y. & Miyake, Y. Size-Controlled synthesis of zeolitic imidazolate framework-8 (ZIF-8) crystals in an aqueous system at room temperature. *Chem. Lett.* **41**, 1337–1339 (2012).

165. Reiners, M. *et al.* Growth and Crystallization of TiO 2 Thin Films by Atomic Layer Deposition Using a Novel Amido Guanidinate Titanium Source and Tetrakis-dimethylamido-titanium. *Chem. Mater.* **25**, 2934–2943 (2013).

166. Wan, G. *et al.* Ti2Nb10O29 microspheres coated with ultrathin N-doped carbon layers by atomic layer deposition for enhanced lithium storage. *Chem. Commun.* **55**, 517–520 (2019).

167. Kim, J. H. *et al.* Enhanced Activity Promoted by CeOx on a CoOx Electrocatalyst for the Oxygen Evolution Reaction. *ACS Catal.* **8**, 4257–4265 (2018).

168. Liu, X. *et al.* Metal (Ni, Co)-Metal Oxides/Graphene Nanocomposites as Multifunctional Electrocatalysts. *Adv. Funct. Mater.* **25**, 5799–5808 (2015).

169. Chen, D., Zou, L., Li, S. & Zheng, F. Nanospherical like reduced graphene oxide decorated TiO 2 nanoparticles: An advanced catalyst for the hydrogen evolution reaction. *Sci. Rep.* **6**, 1–8 (2016).